A Generalized Nambu–Jona-Lasinio Model

by

HU LI

A dissertation submitted to the Graduate Faculty in Physics in partial fulfillment of the requirements for the degree of Doctor of Philosophy, The City University of New York

2005

ProQuest Information and Learning Company
300 North Zeeb Road
P.O. Box 1346
Ann Arbor, MI 48106-1346

This manuscript has been read and accepted for the Graduate Faculty in Physics in satisfaction of the dissertation requirement for the degree of Doctor of Philosophy.

04/26/05	Professor Carl M. Shakin
Date	Chair of Examining Committee
04/26/05	Professor Sultan Catto
Date	Executive Officer

Professor Carl M. Shakin

Professor Louis S. Celenza

Professor Peter Lesser

Professor Ming-Kung Liou

Professor Sultan Catto

Supervisory Committee

THE CITY UNIVERSITY OF NEW YORK

Abstract

A Generalized Nambu–Jona-Lasinio Model

by

Hu Li

Adviser: Professor Carl M. Shakin

We make use of the Nambu–Jona-Lasinio (NJL) formalism and real-time finite-temperature field theory to calculate spectral functions, as well as Euclidean-time hadronic current correlation functions in the deconfined phase of quantum chromodynamics (QCD), and have made a comparison to the lattice results for the correlators. Some resonant features are seen in our calculations. The spectral functions obtained when using the maximum-entropy-method (MEM) and the lattice data differ from the spectral functions that we calculate in our chiral model. However, our results for the Euclidean-time correlators are in general agreement with the lattice results, with better agreement when our temperature-dependent coupling parameters are used than when temperature-independent parameters are used for the NJL model.

We extend our calculations to study the excitations of dense quark matter at zero temperature and explore some consequences of the use of density-dependent coupling parameters for the Nambu–Jona-Lasinio model.

We also use our model to study the optical potential of a quark in the quark-gluon plasma and calculate the quark mean-free-path. Our results represent a specific example of the dynamics of the plasma as described by the Stony Brook group.

Acknowledgements

To Professor Carl M. Shakin, my thesis advisor, I wish to express my deepest gratitude for his valuable guidance and constant encouragement throughout this thesis work. I would also like to express my sincere gratitude to Professor Louis S. Celenza for the help given to me during the course of this work. My thanks also go to Mr. Qing Sun, Mr. Bing He, Dr. Xiangdong Li and Dr. Huangsheng Wang for many useful discussions. Finally, I would like to thank the Department of Physics of Brooklyn College and the Research Foundation of CUNY for financial support. And invaluable assistance by Professor Ming-Kung Liou, Ms. Laura Incampo, and Ms. Suzanne Whiter is also much appreciated.

Contents

List of Tables

List of Figures

Chapter 1

Introduction

Recent years have seen a great deal of interest in the properties of matter at high temperature and density. One hopes to be able to understand aspects of the dynamics of the early universe. One goal has been to study the creation of a plasma of quarks and gluons by scattering heavy nuclei at very high energies. A good deal of that work is being done at the relativistic heavy-ion collider (RHIC) at the Brookhaven Laboratory.

In this thesis we have studied the properties of matter at high temperature and density using a version of the Nambu–Jona-Lasinio model. This model has been used to study matter at very high density, however, relatively few studies have been made of this model at high temperatures.

Our work has been stimulated, in part, by various lattice studies of QCD at finite temperature. For many years it was thought that one could consider the quark-gluon plasma as a gas of quarks and gluons. These ideas have been changed recently with the success of a hydrodynamic description of the quark-gluon plasma in the early stages of the heavy-ion collision process. One reason that the hydrodynamic description is appropriate is that there are many resonances formed in the quark-gluon system that lead to quite small quark mean-free paths.

In our work we have studied various aspects of the quark-gluon plasma. We have made several calculations of hadronic current correlation functions. The results of these calculations could be compared to some results obtained in lattice simulations of QCD. Results of our studies and comparison to lattice data are presented in Chapter II of this thesis. In Chapter III we go on to study correlation functions of various hadronic currents at finite matter density. Finally, in Chapter IV we discuss quark propagation in dense matter and include a calculation of the quark optical potential and the quark mean-free path. In our early work we did not take into account resonances found in the quark-gluon plasma and obtained long mean-free paths. The inclusion of the effects of resonance formation led to results more in keeping with the present successful hydrodynamic description of the quark-gluon plasma.

Chapter 2

Temperature-Dependent Hadronic Correlation Function

2.1 Introduction

Euclidean-time hadronic current correlation functions contain information about the hadronic spectrum, including information about the temperature dependence of hadronic resonances, the widths of these states and the eventual disappearance of such states from the spectrum at sufficiently high temperature. In this work we calculate various hadronic correlation functions and compare our results to results obtained in lattice simulations of QCD (1; 2; 3). The lattice results for the correlators, $G(\tau, T)$, may be used to obtain the corresponding spectral functions, $\sigma(\omega, T)$, by making use of the relation

$$G(\tau, T) = \int_0^\infty d\omega\sigma(\omega, T)K(\tau, \omega, T)\,, \tag{2.1}$$

where

$$K(\tau, \omega, T) = \frac{\cosh[\omega(\tau - 1/2T)]}{\sinh(\omega/2T)}\,. \tag{2.2}$$

The procedure to obtain $\sigma(\omega, T)$ from the knowledge of $G(\tau, T)$ makes use of the maximum entropy method (MEM) (4; 5; 6), since $G(\tau, T)$ is only known at a limited number of points.

In our studies we make use of the Nambu–Jona-Lasinio (NJL) model. The Lagrangian of the generalized NJL model we have used in our studies is

$$\begin{aligned}\mathcal{L} &= \bar{q}(i\partial\!\!\!/ - m^0)q + \frac{G_S}{2}\sum_{i=0}^{8}[(\bar{q}\lambda^i q)^2 + (\bar{q}i\gamma_5\lambda^i q)^2] \\ &- \frac{G_V}{2}\sum_{i=0}^{8}[(\bar{q}\lambda^i\gamma_\mu q)^2 + (\bar{q}\lambda^i\gamma_5\gamma_\mu q)^2] \\ &+ \frac{G_D}{2}\{\det[\bar{q}(1+\lambda_5)q] + \det[\bar{q}(1-\lambda_5)q]\} + \mathcal{L}_{conf}\,.\end{aligned} \tag{2.3}$$

Here, m^0 is a current quark mass matrix, m^0=diag(m_u^0, m_d^0, m_s^0). The λ_i are the Gell-Mann (flavor) matrices and $\lambda^0 = \sqrt{2/3}\mathbf{1}$, with $\mathbf{1}$ being the unit matrix. The fourth term is the 't Hooft interaction and $\mathcal{L}_{conf}$ represents the model of confinement used in our studies of meson properties.

In order to specify the parameters in Eq. (2.3) we may refer to Ref. (7). There, a quite detailed fit was made to the properties of the η mesons. The analysis yields fits to the first four experimentally known levels and provides excellent fits to the mixing angles and decay constants of the $\eta(547)$ and $\eta\prime(958)$. That work led to the specification of $G_S = 11.84$ GeV^{-2}. The 't Hooft interaction strength, G_D, was taken to be in the range -220 GeV$^{-5} \leq G_D \leq -180$ GeV^{-5} when calculating the properties of the η mesons. The value $G_V = 13.0$ GeV^{-2} was used in Ref. (7).

In terms of these parameters we can introduce effective coupling constants for states with particular quantum numbers. The effective coupling parameter involves the vacuum condensates $\alpha =<0|\bar{u}u|0>$, $\beta =<0|\bar{d}d|0>$ and $\gamma =<0|\bar{s}s|0>$. For the pseudoscalar-isovector states, we have (8)

$$G_P^{eff} = G_S + \gamma\frac{G_D}{2}\,. \tag{2.4}$$

We take $\alpha = \beta = -(0.241\text{GeV})^3$ and $\gamma = -(0.258\text{GeV})^3$ (9). If we put $G_D = -190\ \text{GeV}^{-5}$, we find $G_P^{eff} = 13.47\ \ \text{GeV}^{-2}$.

In Ref. (10) we presented relativistic random phase approximation (RPA) calculations for the pion, kaon and several other mesons. It was found that in the case of pion, that the use of $G_P^{eff} = 13.49\ \text{GeV}^{-2}$ gave a pion energy of 140 MeV at $T = 0$. It is gratifying to see that an independent calculation gives rise to essentially the same effective coupling constant as that obtained from the parameters determined in Ref. (7).

If we consider the scalar-isovector states, the effective coupling constant is

$$G_S^{eff} = G_S - \gamma\frac{G_D}{2}\,, \tag{2.5}$$

which, for $G_S = -11.84\ \text{GeV}^{-2}$, $G_D = 190.0\ \text{GeV}^{-5}$ and $\gamma = -(0.258\text{GeV})^3$, yields $G_S^{eff} = 10.21\ \text{GeV}^{-2}$. When we compare G_P^{eff} with G_S^{eff}, we see that we can expect the resonant enhancement of the spectral functions for the pseudoscalar-isovector channel will be larger in magnitude than that of the spectral function of the scalar-isovector channel. On the other hand, since the 't Hooft interaction does not affect the vector or axial-vector coupling constants, these coupling constants would be equal in our model, leading us to expect quite similar spectral functions for these two channels.

In the study of the η mesons $G_V = 13.00\ \ \mathrm{GeV}^{-2}$ was used. However,the results for the η mesons are not particularly sensitive to that parameter. In this work we present the results for $G_V = 11.46\ \ \mathrm{GeV}^{-2}$.

It was found that the use of a sharp cutoff did not allow us to study radial excitations with a large number of nodes. However, a Gaussian regulator, $\exp[-\vec{k}^{\,2}/\alpha^2]$, with $\alpha = 0.605$ GeV, gave similar results as that of the sharp cutoff $\Lambda_3 = 0.622$ GeV for the low-lying states and also allowed us to describe radial excitations with many nodes. Therefore, we use the Gaussian regulator with $\alpha = 0.605$ GeV in almost all of our calculations.

We calculated the temperature dependence of the spectra of various meons using our generalized NJL model, which includes a covariant model of confinement and presented results for the π, K, a_0, f_0 and K_0^* mesons in Ref. (10). In that work, temperature-dependent constituent quark masses were calculated using the equation (11)

$$m(T) = m^0 + 2G_S(T)N_c\frac{m(T)}{\pi^2}\int_0^\Lambda dp\frac{p^2}{E_p}\tanh(\frac{1}{2}\beta E_p)\,. \tag{2.6}$$

Here, m^0 is the current quark mass, $G_S(T)$ is a temperature-dependent coupling constant introduced in our model. (In Ref. (10) we used what was termed model 1 for $G_S(T)$.) Here, $N_c = 3$ is the number of colors, $\beta = 1/T$ and $E_p = [\vec{p}^{\,2} + m^2(T)]^{1/2}$. Further, $\Lambda = 0.631$ GeV is a cutoff such that $|\vec{p}| \leq \Lambda$. We have put $\Lambda = 0.631$ GeV, since that is the cutoff that is often used when solving Eq. (2.6) (8). We have also used $m_u^0 = 5.5$ MeV and $m_s^0 = 120$ MeV. Since in our work dealing with meson spectra, we have used $m_u = 0.364$ GeV and $m_s = 0.565$ GeV as phenomenological parameters, we have put $G_S(0) = 2G$, with $G = 5.691$ GeV^{-2}, in the notation of Ref. (11), to reproduce those values. In Ref. (11) G is one-half of the G_S defined in Eq. (2.3)

Since the use of temperature-dependent coupling constants is an unusual feature of our work, we now describe some advantages that follow from that choice. Our original introduction of temperature dependence, $G(T) = G[1 - 0.17(T/T_c)]$, with $T_c = 170$ MeV, had the purpose of simulating the dynamical interactions which eliminate pion or kaon condensation at relatively low temperatures. However, we found when solving Eq. (2.6) for the temperature-dependent constituent mass of the up quark, chiral symmetry was (partially) restored at lower temperatures than when constant coupling parameters were used. This may be seen in Fig. 2.1, where we show the results that follow from the use of a constant value of $G(T) = 5.691$ GeV^{-2}(in the notation of Ref. (11)) as a dotted line. Here we have used $m^0 = 5.5$ MeV as the current quark mass. For the solid and dashed curves in Fig. 2.1 we have used $G(T) = G[1 - 0.17(T/T_c)]$. For the sake of this discussion, let us consider the reduction of the constituent mass to 50 MeV from 364 MeV as signal of the (partial) restoration of chiral symmetry. For the dashed and solid curves, that restoration take place at about $T_c = 170$ MeV, while for the dotted curve the (partial) restoration of chiral symmetry takes place at about 250 MeV. For QCD, the transition temperature is about 150-170 MeV. Since we

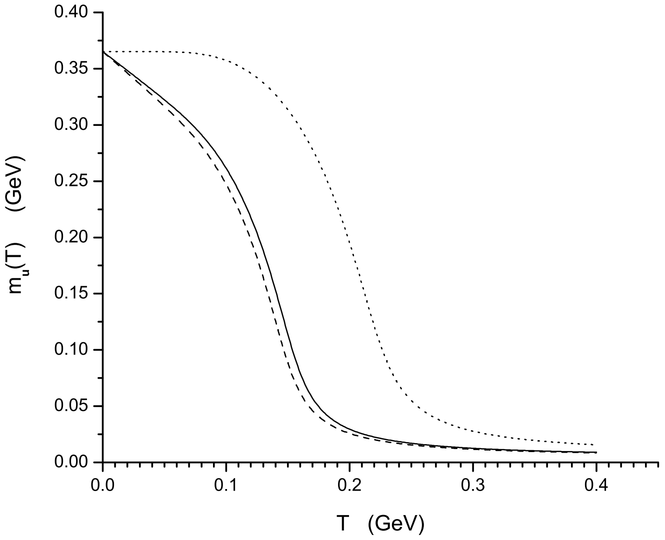

Figure 2.1: We exhibit the solution for $m_u(T)$ obtained using Eq. (5.38) of Ref. (11), where $m^0 = 5.50$ MeV and $\Lambda = 0.631$ GeV. The dotted curve corresponds to the use of a constant value $G = 5.691$ GeV^{-2}, in the notation of Ref. (11). For the solid and dashed curves we have used $G(T) = G[1 - 0.17(T/T_c)]$. For the solid curve $T_c = 0.170$ GeV and for the dashed curve we have used $T_c = 0.150$ GeV.

are attempting to create a model that has some correspondence to QCD, with dynamical quarks, we see that the temperature-dependent coupling constants lead to the desired behavior.

The temperature dependence of the constituent mass in the case of temperature-dependent coupling constants is such that we described the mesonic confinement-deconfinement transition as taking place at $T \approx T_c$ with $T_c = 170$ MeV in Ref. (10). In that work we have studied the confinement-deconfinement transition for

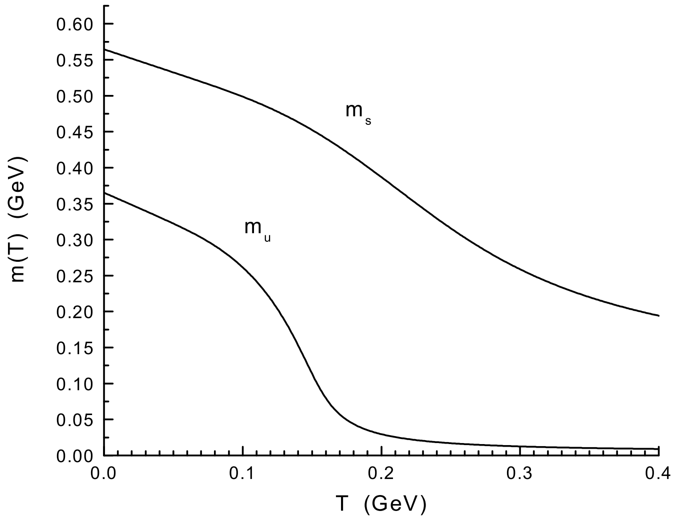

Figure 2.2: Temperature dependent constituent mass values, $m_u(T)$ and $m_s(T)$, calculated in a mean-field approximation (11), are shown. [See Eq. (2.6)]. Here $m_u^0 = 0.0055$ GeV, $m_s^0 = 0.120$ GeV, and $G(T) = 5.691[1 - 0.17(T/T_c)]$, if we use Klevansky's notation (11). (The value of G_S of Eq. (2.3) is twice the value of G used in (11).)

the π, K, a_0, f_0 and K_0^* mesons. We have checked that, without the introduction of the temperature-dependent coupling constants, the confinement-deconfinement transition would take place at a significantly higher temperature.

A further advantage of the use of our temperature-dependent coupling parameter is that the NJL interaction goes to zero for $T = 5.88T_c$.(It is put equal to zero for $T > 5.88T_c$.) We suggest that that is consistent with QCD thermodynamics, since it appears that the system is weakly coupled for $T \geq 6T_c$ (12).

In Fig. 2.2 we show the behavior of both the up and strange quark constituent masses calculated with Eq. (2.6) using current masses $m_u^0 = 5.50$ MeV and $m_s^0 = 120$ MeV. For the calculations made in this work, we have used the temperature-dependent up (or down) quark masses shown in Fig. 2.2 for temperatures for which the quark masses are quite small. Therefore, our results are insensitive to variations of the mass values shown in Fig. 2.2.

In calculating the constituent mass values we have neglected the confining interaction. That interaction was taken into account in our earlier Euclidean-space calculation of the quark self-energy (13), which also included the effects related to the 't Hooft interaction. We found that, to a good approximation, we could neglect the confining and 't Hooft interactions, if we modified the value of the NJL coupling constant, G_S, and we adopt that approach when using Eq. (2.6).

2.2 Polarization Functions at Finite Temperature

The basic polarization function that is calculated in the NJL model is shown in Fig. 2.3. We will consider calculations of such functions in the frame where $\vec{P} = 0$. In our earlier work, calculations were made after a confinement vertex was included. That vertex is represented by the filled triangular region in Fig. 2.3. However, we here consider calculations for $T \geq 1.2\,T_c$ where confinement may be neglected. We will, however, use the temperature-dependent mass values

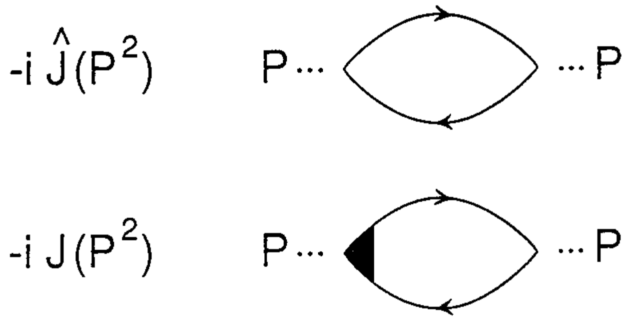

Figure 2.3: The upper figure represents the basic polarization diagram of the NJL model in which the lines represent a constituent quark and a constituent antiquark. The lower figure shows a confinement vertex [filled triangular region] used in our earlier work. For the present work we neglect confinement for $T \geq 1.2\,T_c$, with $T_c = 150$ MeV.

shown in Fig. 2.2.

The procedure we adopt is based upon the real-time finite-temperature formalism, in which the imaginary part of the polarization function may be calculated. Then, the real part of the function is obtained using a dispersion relation. The result we need for this work has been already given in the work of Kobes and Semenoff (14). (In Ref. (14) the quark momentum in Fig. 2.3 is k and the antiquark momentum is $k - P$. We will adopt that notation in this section for ease of reference to the results presented in Ref. (14).) With reference to Eq. (5.4) of

Ref. (14), we write the imaginary part of the scalar polarization function as

$$\begin{aligned}\mathrm{Im}\, J_S(P^2,T) = \frac{1}{2}(2N_c)\beta_S\,\epsilon(P^0)\int\frac{d^3k}{(2\pi)^3}\,e^{-\vec{k}^{\,2}/\alpha^2}\left(\frac{2\pi}{2E_1(k)2E_2(k)}\right) \qquad (2.7)\\ \{(1-n_1(k)-n_2(k))\delta(P^0-E_1(k)-E_2(k))\\ -(n_1(k)-n_2(k))\delta(P^0+E_1(k)-E_2(k))\\ -(n_2(k)-n_1(k))\delta(P^0-E_1(k)+E_2(k))\\ -(1-n_1(k)-n_2(k))\delta(P^0+E_1(k)+E_2(k))\}\,.\end{aligned}$$

Here, $E_1(k) = [\vec{k}^{\,2} + m_1^2(T)]^{1/2}$. Relative to Eq. (5.4) of Ref. (14), we have changed the sign, removed a factor of g^2 and have included a statistical factor of $2N_c$, where the factor of 2 arises from the flavor trace. In addition, we have included a Gaussian regulator, $\exp[-\vec{k}^{\,2}/\alpha^2]$, with $\alpha = 0.605$ GeV, which is the same as that used in most of our applications of the NJL model in the calculation of meson properties. We also note that

$$n_1(k) = \frac{1}{e^{\beta E_1(k)}+1}\,, \qquad (2.8)$$

and

$$n_2(k) = \frac{1}{e^{\beta E_2(k)}+1}\,. \qquad (2.9)$$

For the calculation of the imaginary part of the polarization function, we may put $k^2 = m_1^2(T)$ and $(k-P)^2 = m_2^2(T)$, since in that calculation the quark and antiquark are on-mass-shell. In Eq. (2.7) the factor β_S arises from a trace involving Dirac matrices, such that

$$\begin{aligned}\beta_S &= -\mathrm{Tr}[(\not{k}+m_1)(\not{k}-\not{P}+m_2)] &(2.10)\\ &= 2P^2-2(m_1+m_2)^2\,, &(2.11)\end{aligned}$$

where m_1 and m_2 depend upon temperature. In the frame where $\vec{P}=0$, and in the case $m_1=m_2=m$, we have $\beta_S=2P_0^2(1-4m^2/P_0^2)$. For the scalar case, with $m_1=m_2=m$, we find

$$\mathrm{Im}\,J_S(P^2,T)=\frac{N_cP_0^2}{4\pi}\left(1-\frac{4m^2}{P_0^2}\right)^{3/2}e^{-\vec{k}^{\,2}/\alpha^2}[1-2n_1(k)]\,, \tag{2.12}$$

where

$$\vec{k}^{\,2}=\frac{P_0^2}{4}-m^2(T)\,. \tag{2.13}$$

For pseudoscalar mesons, we replace β_S by

$$\begin{aligned}\beta_P &= -\mathrm{Tr}[i\gamma_5(\not{k}+m_1)i\gamma_5(\not{k}-\not{P}+m_2)] &(2.14)\\ &= 2P^2-2(m_1-m_2)^2\,, &(2.15)\end{aligned}$$

which for $m_1=m_2$ is $\beta_P=2P_0^2$ in the frame where $\vec{P}=0$. We find, for the π mesons,

$$\mathrm{Im}\,J_P(P^2,T)=\frac{N_cP_0^2}{4\pi}\left(1-\frac{4m_u^2(T)}{P_0^2}\right)^{1/2}e^{-\vec{k}^{\,2}/\alpha^2}[1-2n_1(k)]\,, \tag{2.16}$$

where $\vec{k}^{\,2}=P_0^2/4-m_u^2(T)$, as above. Thus, we see that, relative to the scalar case, the phase space factor has an exponent of 1/2 corresponding to a s-wave amplitude. For the scalars, the exponent of the phase-space factor is 3/2, as seen in Eq. (2.12).

For a study of the vector-isovector correlators, we introduce conserved vector currents $j_{\mu,i}(x) = \bar{q}(x)\gamma_\mu\lambda_i q(x)$ with i=1, 2 and 3. In this case we define

$$J_V^{\mu\nu}(P^2,T) = \left(g^{\,\mu\nu} - \frac{P^{\,\mu}P^{\,\nu}}{P^2}\right) J_V(P^2,T) \tag{2.17}$$

and

$$C_V^{\mu\nu}(P^2,T) = \left(g^{\,\mu\nu} - \frac{P^{\,\mu}P^{\,\nu}}{P^2}\right) C_V(P^2,T)\,, \tag{2.18}$$

taking into account the fact that the current $j_{\mu,\,i}(x)$ is conserved. We may then use the fact that

$$J_V(P^2,T) = \frac{1}{3} g_{\mu\nu} J_V^{\mu\nu}(P^2,T) \tag{2.19}$$

and

$$\begin{aligned} \mathrm{Im}\, J_V(P^2,T) &= \frac{2N_c}{3}\left[\frac{P_0^2+2m_u^2(T)}{4\pi}\right]\left(1-\frac{4m_u^2(T)}{P_0^2}\right)^{1/2} && (2.20)\\ &\times\; e^{-\vec{k}^{\,2}/\alpha^2}[1-2n_1(k)] \\ &\simeq\; \frac{2}{3}\mathrm{Im} J_P(P^2,T)\,. && (2.21)\end{aligned}$$

We now consider

$$\beta_{\mu\nu}^V = \mathrm{Tr}[\gamma_\mu(\not{k}+m_1)\gamma_\nu(\not{k}-\not{P}+m_2)]\,, \tag{2.22}$$

and calculate

$$g^{\mu\nu}\beta_{\mu\nu}^V = 4[P^2-m_1^2-m_2^2+4m_1m_2]\,, \tag{2.23}$$

which, in the equal-mass case, is equal to $4P_0^2+8m^2(T)$, when $m_1=m_2$ and $\vec{P}=0$. This result will be needed when we calculate the correlator of vector currents in the next section. Note that for the elevated temperatures considered in this work $m_u(T)=m_d(T)$ is quite small, so that $4P_0^2+8m_u^2(T)$ can be approximated by $4P_0^2$ when we consider the vector current correlation functions. In that case, we have

$$\mathrm{Im}\, J_V(P^2,T) \simeq \frac{2}{3}\mathrm{Im}\, J_P(P^2,T)\,, \tag{2.24}$$

At this point it is useful to define functions that do not contain the Gaussian regulator:

$$\mathrm{Im}\, \tilde{J}_P(P^2,T) = \frac{N_c P_0^2}{4\pi}\left(1-\frac{4m(T)^2}{P_0^2}\right)^{1/2}[1-2n_1(k)]\,, \tag{2.25}$$

and

$$\mathrm{Im}\, \tilde{J}_V(P^2,T) = \frac{2}{3}\frac{N_c P_0^2}{4\pi}\left(1-\frac{4m(T)^2}{P_0^2}\right)^{1/2}[1-2n_1(k)]\,. \tag{2.26}$$

For the functions defined in Eq. (2.25) and (2.26) we need to use a twice-subtracted dispersion relation to obtain $\mathrm{Re}\, \tilde{J}_P(P^2,T)$, or $\mathrm{Re}\, \tilde{J}_V(P^2,T)$. For example,

$$\begin{aligned}\mathrm{Re}\, \tilde{J}_P(P^2,T) &= \mathrm{Re}\, \tilde{J}_P(0,T) + \frac{P^2}{P_0^2}[\mathrm{Re}\, \tilde{J}_P(P_0^2,T) - \mathrm{Re}\, \tilde{J}_P(0,T)] \qquad (2.27)\\ &+ \frac{P^2(P^2-P_0^2)}{\pi}\int_{m^2(T)}^{\tilde{\Lambda}^2} ds \frac{\mathrm{Im}\, \tilde{J}_P(s,T)}{s(P^2-s)(P_0^2-s)}\,,\end{aligned}$$

where $\tilde{\Lambda}^2$ can be quite large since the integral over the imaginary part of the polarization function is now convergent. We may introduce $\tilde{J}_P(P^2,T)$ and $\tilde{J}_V(P^2,T)$ as complex functions, since we now have both the real and imaginary parts of these functions. We note that the construction of either $\mathrm{Re}\, J_P(P^2, T)$ or $\mathrm{Re}\, J_V(P^2, T)$ by means of a dispersion relation does not require a subtraction. We use these functions to define the complex functions $J_P(P^2, T)$ and $J_V(P^2, T)$.

In order to make use of Eq. (2.27) we need to specify $\tilde{J}_P(0)$ and $\tilde{J}_P(P_0^2)$. We found it useful to take $P_0^2 = -1.0$ GeV^2 and to put $\tilde{J}_P(0) = J_P(0)$ and $\tilde{J}_P(P_0^2) = J_P(P_0^2)$. The quantities $\tilde{J}_V(0)$ and $\tilde{J}_V(P_0^2)$ are determined in an analogous fashion. This procedure in which we fix the behavior of a function such as $\tilde{J}_P(P^2)$ or $\tilde{J}_V(P^2)$, which may be used when making calculations for large P^2, is quite analogous to the procedure used in Ref. (15). In that work we made use of dispersion relations to construct a continuous vector-isovector current correlation function that had the correct perturbative behavior for $P^2 \to -\infty$ and also described the low-energy resonance present in the correlator due to the excitation of the ρ meson. In Ref. (15) the NJL model was shown to provide a quite satisfactory description of the low-energy resonant behavior of the vector-isovector correlation function.

We may compare our expressions for $(1/\pi)\mathrm{Im}J(P^2)$ with those given in Eq. (2.13) of Ref. (16). We find that the scalar and pseudoscalar polarization functions are defined there with a sign opposite to ours. However, since we have defined the pseudoscalar current using the matrix $i\gamma_5$ rather than γ_5, which was used in Ref. (16), our expression for the spectral function agrees with that of

Ref. (16) with respect to the sign in the pseudoscalar case. In the case of the vector and axial-vector spectral functions, we have the same sign convention as that of Ref. (16).

In Ref. (16) use is made of the hard-thermal-loop (HTL) approximation. It was found that the scalar channels are only moderately influenced by the HTL medium effects, while the HTL vertex corrections lead to divergent vector correlators.

2.3 Calculation of Hadronic Current Correlation Functions

In this section we consider the calculation of temperature-dependent hadronic current correlation functions. The general form of the correlator is a transform of a time-ordered product of currents,

$$iC(P^2,T) = \int d^4x e^{iP\cdot x} \ll T(j(x)j(0)) \gg , \tag{2.28}$$

where the double bracket is a reminder that we are considering the finite-temperature case.

For the study of pseudoscalar states, we may consider currents of the form $j_{P,i}(x) = \bar{q}(x)i\gamma_5\lambda^i q(x)$, where, in the case of the π mesons, $i = 1, 2$ and 3. For the study of pseudoscalar-isoscalar mesons, we again introduce $j_{P,i}(x) = \bar{q}(x)i\gamma_5\lambda^i q(x)$, but here $i = 0$ for the flavor-singlet current and $i = 8$ for the flavor-octet current. For the study of scalar-isoscalar mesons, we introduce $j_{S,i}(x) = \bar{q}(x)\lambda^i q(x)$, with $i = 0$ for the flavor-singlet current and $i = 8$ for the flavor-octet current (17).

In the case of the pseudoscalar-isovector mesons, the correlator may be expressed in terms of the basic vacuum polarization function of the NJL model, $J_P(P^2, T)$ (8; 9; 11). Thus,

$$C_P(P^2, T) = \tilde{J}_P(P^2, T)\frac{1}{1 - G_P(T)J_P(P^2, T)}\,, \tag{2.29}$$

where $G_P(T)$ is the coupling constant appropriate for our study of π mesons. We have found $G_P(T) = 13.49$ GeV^{-2} by fitting the pion mass in a calculation made at $T = 0$, with $m_u = m_d = 0.364$ GeV. The result given in Eq. (2.29) is only expected to be useful for small P^2, since the Gaussian regulator strongly modifies the large P^2 behavior. Therefore, we suggest that the following form is useful, if we are to consider the larger values of P^2

$$\frac{C_P(P^2, T)}{P^2} = \left[\frac{\tilde{J}_P(P^2, T)}{P^2}\right]\frac{1}{1 - G_P(T)J_P(P^2, T)}\,. \tag{2.30}$$

(As usual, we put $\vec{P} = 0$.) This form has two important features. At large P_0^2, $\mathrm{Im}\, C_P(P_0, T)/P_0^2$ is a constant, since $\mathrm{Im}\, \tilde{J}_P(P_0^2, T)$ is proportional to P_0^2. Further, the denominator of the second term on the right-hand side of Eq. (2.30) goes to 1 for large P_0^2. On the other hand, at small P_0^2, that denominator is capable of describing resonant enhancement of the correlation function. (We may again refer to Ref. (15), in which a similar approximation is described.)

The calculation of the correlator for pseudoscalar-isoscalar states is more complex, since there are both flavor-singlet and flavor-octet states to consider. We may define polarization functions for u, d and s quarks: $J_u(P^2,T)$, $J_d(P^2,T)$ and $J_s(P^2,T)$. (We recall that the factor of 2 arising from the flavor trace is not included when these functions are calculated.) In terms of these polarization functions we may then define

$$J_{00}(P^2,T)=\frac{2}{3}[J_u(P^2,T)+J_d(P^2,T)+J_s(P^2,T)]\,, \tag{2.31}$$

$$J_{08}(P^2,T)=\frac{\sqrt{2}}{3}[J_u(P^2,T)+J_d(P^2,T)-2J_s(P^2,T)]\,, \tag{2.32}$$

and

$$J_{88}(P^2,T)=\frac{1}{3}[J_u(P^2,T)+J_d(P^2,T)+4J_s(P^2,T)]\,. \tag{2.33}$$

We also introduce the matrices

$$J(P^2,T)=\begin{bmatrix} J_{00}(P^2,T) & J_{08}(P^2,T) \\ J_{80}(P^2,T) & J_{88}(P^2,T) \end{bmatrix}, \tag{2.34}$$

$$G(T)=\begin{bmatrix} G_{00}(T) & G_{08}(T) \\ G_{80}(T) & G_{88}(T) \end{bmatrix}, \tag{2.35}$$

and

$$C(P^2,T)=\begin{bmatrix} C_{00}(P^2,T) & C_{08}(P^2,T) \\ C_{80}(P^2,T) & C_{88}(P^2,T) \end{bmatrix}. \tag{2.36}$$

We then write the matrix relation

$$C(P^2,T)=J(P^2,T)[1-G(T)J(P^2,T)]^{-1}\,. \tag{2.37}$$

For some purposes it may be useful to also define a t matrix

$$t(P^2,T)=[1-G(T)J(P^2,T)]^{-1}G(T)\,, \tag{2.38}$$

where $t(P^2,T)$ has the structure shown in Eqs. (2.34)-(2.36). The same resonant structures are seen in both $C(P^2,T)$ and $t(P^2,T)$.

For the vector-isovector case, we then have

$$C_V(P^2,T)=\tilde{J}_V(P^2,T)\frac{1}{1-G_V(T)J_V(P^2,T)}\,, \tag{2.39}$$

where we have introduced

$$\begin{aligned}
\mathrm{Im}\tilde{J}_V(P^2,T) &= \frac{2}{3}\left[\frac{P_0^2+2m_u^2(T)}{4\pi}\right]\left(1-\frac{4m_u^2(T)}{P_0^2}\right)^{1/2}[1-2n_1(k)] \qquad (2.40)\\
&\simeq \frac{2}{3}\mathrm{Im}\tilde{J}_P(P^2,T)\,. \qquad (2.41)
\end{aligned}$$

(See Eq. (2.13) for the specification of $k=|\vec{k}|$.) In the literature, ω is used instead of P_0 (1; 2; 3). We may define the spectral functions

$$\sigma_V(\omega,T)=\frac{1}{\pi}\,\mathrm{Im}\,C_V(\omega,T)\,, \tag{2.42}$$

and

$$\sigma_P(\omega,T)=\frac{1}{\pi}\,\mathrm{Im}\,C_P(\omega,T)\,. \tag{2.43}$$

We may use the notation $\bar{\sigma}_P(\omega,T)$ and $\bar{\sigma}_V(\omega,T)$ for the spectral functions given in the literature (1; 2; 3). We have the following relations:

$$\bar{\sigma}_P(\omega,T)=\sigma_P(\omega,T) \tag{2.44}$$

and

$$\frac{\bar{\sigma}_V(\omega,T)}{2}=\frac{3}{4}\sigma_V(\omega,T)\,, \tag{2.45}$$

where the factor of 3/4 arises because, in Refs. (1; 2; 3), there is a division by 4, while we have divided by 3 as in Eq. (2.19).

2.4 Numerical Results

2.4.1 Correlation Functions of Pseudoscalar-Isovector Currents: Numerical Results

We perform calculations of hadronic current correlation functions for pseudoscalar and vector currents in the range $1.2 \leqslant T/T_c \leqslant 5.88$. We make use of two models for the temperature dependence of the NJL coupling parameters. For model 1, we use $G(T)=G[1-0.17(T/T_c)]$, which was the form used in our previous studies of meson properties (10) and hadronic current correlation functions (17) at finite temperature. In this work we also introduce a model 2, for which $G(T)=G[1-0.0289(T/T_c)^2]$. In both cases, $G(T)=0$ for $T/T_c=5.88$. For values of $T/T_c>5.88$ we put $G(T)=0$ for both models.

In Fig. 2.4 we show $\mathrm{Im}\,C_P(P_0,T)/P_0^2$ for $T/T_c=1.5$, and for model 1, as a solid line. The dashed line represents the result at $T/T_c=1.5$, if we put $G_P(T)=0$. The results for a broader range of temperatures are shown in Fig. 2.5. In Fig. 2.6 we show the ratios $R_P(P_0,T)=\mathrm{Im}C_P(P_0,T)/\mathrm{Im}C_P^{(0)}(P_0,T)$ calculated for various temperatures. Here, $\mathrm{Im}C_P^{(0)}(P_0,T)/P_0^2$ is calculated with

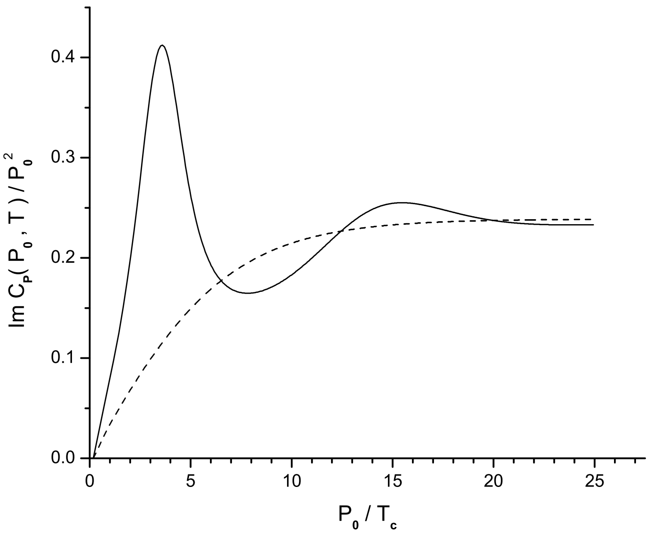

Figure 2.4: Values of $\mathrm{Im}\, C_P(P_0,T)/P_0^2$ are shown at $T/T_c = 1.5$ for model 1, where $G_P(T) = G_P[1 - 0.17\,(T/T_c)]$ (solid line). The dashed line represents the result obtained when $T/T_c = 1.5$ and $G_P(T) = 0$. (Here, the dashed line represents the values of $\mathrm{Im}\,\tilde{J}_P(P_0,T)/P_0^2$ for $T/T_c = 1.5$.)

$G_P(T) = 0$. In Fig. 2.7 we show the ratio $R_G^{(P)}(\tau,T) = G_P(\tau,T)/G_P^{(0)}(\tau,T)$ for various temperatures. Here, $G_P^{(0)}(\tau,T)$ represents $G_P(\tau,T)$ evaluated for $G_P(T) = 0$. In Fig. 2.8 we exhibit $\mathrm{Im}\, C_P(P_0,T)/P_0^2$ for various temperature for model 2.

In Fig. 2.9 we show, as a dashed line, values of $\mathrm{Im}\, C_P(P_0,T)/P_0^2$ at $T/T_c = 5.88$ obtained using a constant value of $G_P(T) = 13.49\ \ \mathrm{GeV}^{-2}$. The solid line is the result for model 1 (or model 2) at $T/T_c = 5.88$, in which case $G_P(T) = 0$ for both models. Since we have argued that for $T/T_c \sim 6$ the quark-gluon plasma may be a weakly interacting system, the use of a constant value for $G_P(T)$ appears to be unacceptable. We present this result to support our argument that the

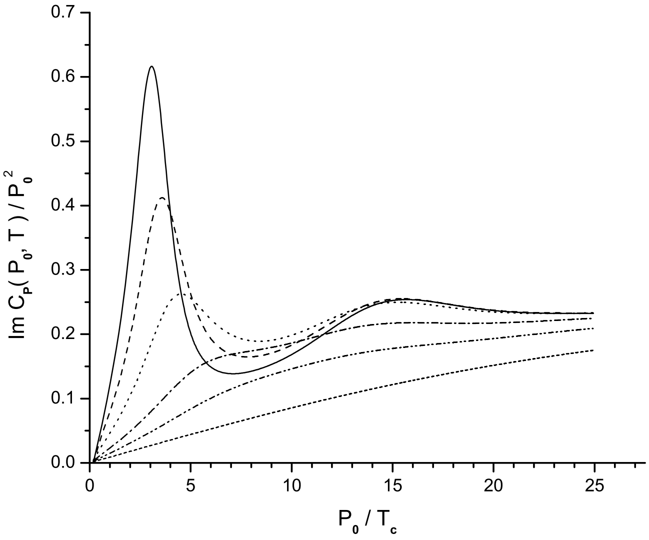

Figure 2.5: Values of $\mathrm{Im}\, C_P(P_0, T)/P_0^2$ are shown for model 1 and for various temperatures: $T/T_c = 1.2$ [sold line], $T/T_c = 1.5$ [dashed line], $T/T_c = 2.0$ [dotted line], $T/T_c = 3.0$ [dashed-dotted line], $T/T_c = 4.0$ [dashed-double dotted line], and $T/T_c = 5.88$ [short-dashed line].

coupling parameters of the chiral Lagrangian model should be made temperature dependent to be consistent with QCD thermodynamics.

In Fig. 2.10 we show values of $G_P(\tau, T)/T^3$ for $T/T_c = 1.5$ [dashed line], $T/T_c = 3.0$ [dash-dotted line] and $T/T_c = 5.88$ [solid line]. In Fig. 1 of Ref. (18) we see a marked difference in the behavior of $G_P(\tau, T)/T^3$ and $G_V(\tau, T)/T^3$.

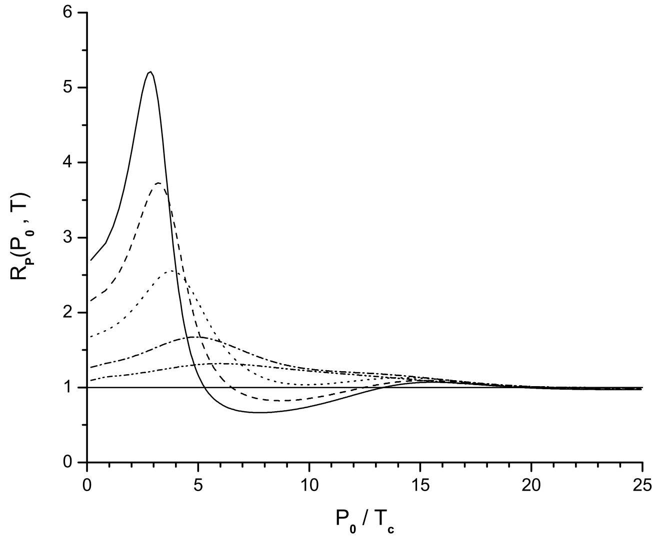

Figure 2.6: The ratio $R_P(P_0,T) = \mathrm{Im}C_P(P_0,T)/\mathrm{Im}C_P^{(0)}(P_0,T)$ is shown for various values of $T/T_c = 1.2$ [solid line], $T/T_c = 1.5$ [dashed line], $T/T_c = 2.9$ [dotted line], $T/T_c = 3.0$ [dot-dashed line] and $T/T_c = 4.0$ [double dot-dashed line]. Here, $\mathrm{Im}C_P^{(0)}(P_0,T)$ is calculated at temperature T with $G_P(T) = 0$.

2.4.2 Correlation Functions of Vector-Isovector Currents: Numerical Results

In Fig. 2.11 we show the values of $\mathrm{Im}\, C_V(P_0,T)/P_0^2$ for model 1 and for $T/T_c = 1.5$, as a solid line. The result for $T/T_c = 1.5$ and $G_V(T) = 0$ is represented by the dashed line. (See Fig. 2.4.) In Fig. 2.12 we show values of $\mathrm{Im}\, C_V(P_0,T)/P_0^2$ for various values of T/T_c and for model 1. Corresponding results for model 2 are given in Fig. 2.13.

In Fig. 2.14 we show the ratio $R_V(P_0,T) = \mathrm{Im}C_V(P_0,T)/\mathrm{Im}C_V^{(0)}(P_0,T)$,

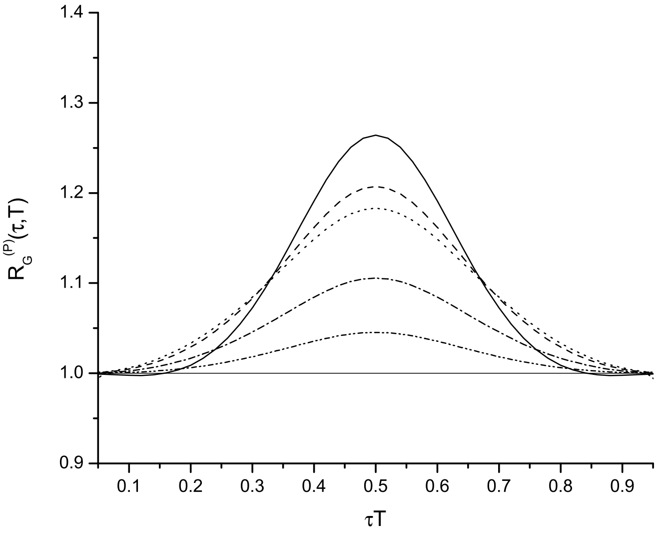

Figure 2.7: Values of $R_G^{(P)}(\tau, T)$ are shown for values of $T/T_c = 1.2$ [solid line], $T/T_c = 1.5$ [dashed line], $T/T_c = 2.0$ [dotted line], $T/T_c = 3.0$ [dashed-dotted line], and $T/T_c = 4.0$ [dashed-double dotted line]. For $T/T_c = 5.88$, $R_G^{(P)}(\tau, T) = 1$.

where $\text{Im}C_V^{(0)}(P_0, T)$ is calculated with $G_V(T) = 0$. (See Fig. 2.6). In Fig. 2.15 we show the ratio $R_G^{(V)}(\tau, T) = G_V(\tau, T)/G_V^{(0)}(\tau, T)$, where $G_V^{(0)}(\tau, T)$ represents $G_V(\tau, T)$ calculated with $G_V(T) = 0$. In Fig. 2.16 we show, as a dashed line, values for $T/T_c = 5.88$ of $\text{Im}\, C_V(P_0, T)/P_0^2$, which were calculated with a constant value of $G_V(T) = 11.46\ \text{GeV}^{-2}$. The solid line represents the results for $G_V(T) = 0$, which is characteristic of models 1 and 2 when $T/T_c = 5.88$. The comments made with respect to Fig. 2.9 are also applicable here.

In Fig. 2.17 we show values of $G_V(\tau, T)/T^3$ for $T/T_c = 1.5$ [dashed line], $T/T_c = 3.0$ [dash-dotted line] and $T/T_c = 5.88$ [solid line]. These results were

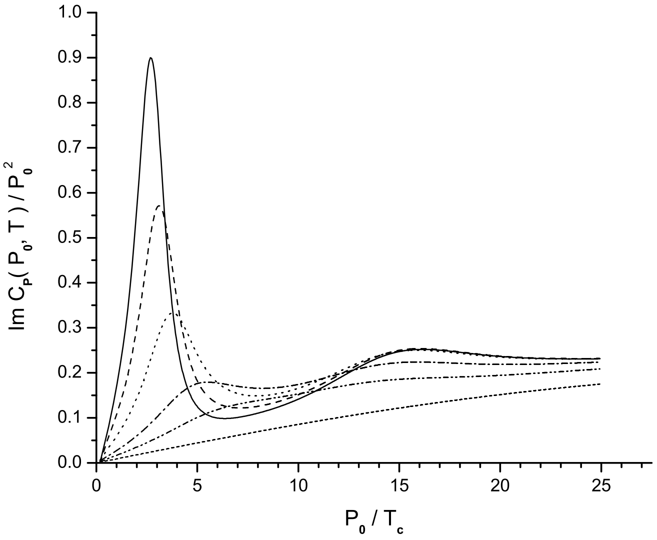

Figure 2.8: Values of $\mathrm{Im}\, C_P(P_0, T)/P_0^2$ are shown at for various temperatures for model 2, with $G_P(T) = G_P[1 - 0.0289\,(T/T_c)^2]$. (See the caption to Fig. 2.5.)

obtained with model 1, and may be compared to those shown in Fig. 2.10, where we see generally similar behavior. That is in strong contrast to the results shown in Ref. (2), where $G_V(\tau, T)/T^3$ and $G_P(\tau, T)/T^3$ show quite different behavior, with the result for the vector correlator close to the values for $G(T) = 0$ at $T/T_c = 1.5$ and $T/T_c = 3.0$. This suggests that the value of $G_V = 11.46$ GeV^{-2} that we have used in this work may be too large, or that the temperature dependence of $G_V(T)$ is such as to yield smaller values than those obtained in this work for model 1 or model 2. (In general, we prefer the the second of these possibilities, since our value of G_V at $T = 0$ is set by fitting meson spectra.) In Fig. 2.18 we show $\mathrm{Im}\, C_V(P_0, T)/P_0^2$ for $T = 1.5\, T_c$, for model 1, with $G_V = 11.46$ GeV^{-2} [solid line], $G_V = 8.00$ GeV^{-2} [dashed line], $G_V = 4.0$ GeV^{-2} [dotted line]

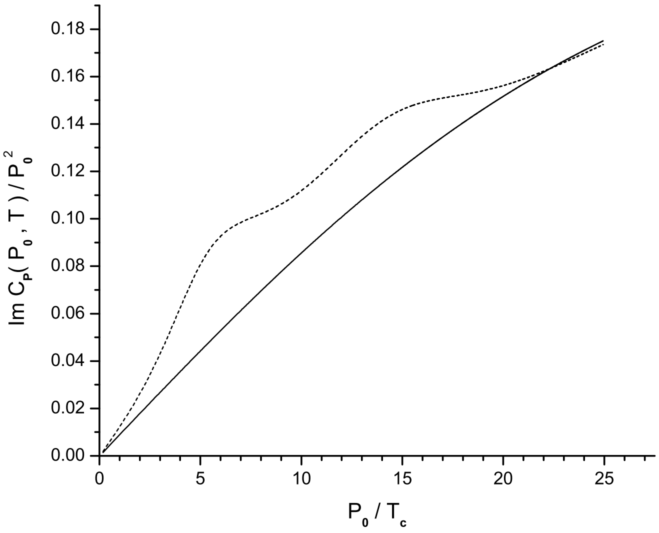

Figure 2.9: Values of $\mathrm{Im}\, C_P(P_0, T)/P_0^2$ are shown for $T/T_c = 5.88$. The dashed line represents the result when $G_P(T) = G_P = 13.49$ GeV^{-2}. The solid line is the result for $G_P(T) = 0$, which is characteristic of models 1 and 2, when $T/T_c = 5.88$. (The solid line, therefore, represents the values of $\mathrm{Im}\, \tilde{J}_P(P_0, T)/P_0^2$ for $T/T_c = 5.88$.)

and $G_V = 0.0$ GeV^{-2} [dot-dashed line].

2.4.3 Correlation Functions of Pseudoscalar-Isoscalar Currents: Numerical Results

Some of our results for the imaginary parts of the pseudoscalar-isoscalar correlators $C_{00}(P^2)$, $C_{88}(P^2)$ and $C_{08}(P^2)$ are shown in Figs. 2.19, 2.20 and 2.21, respectively. In these figures the values are $T/T_c = 1.2$ [solid line], $T/T_c = 1.6$ [dashed line], $T/T_c = 2.0$ [dotted line], $T/T_c = 4.0$ [dashed-dotted line] and

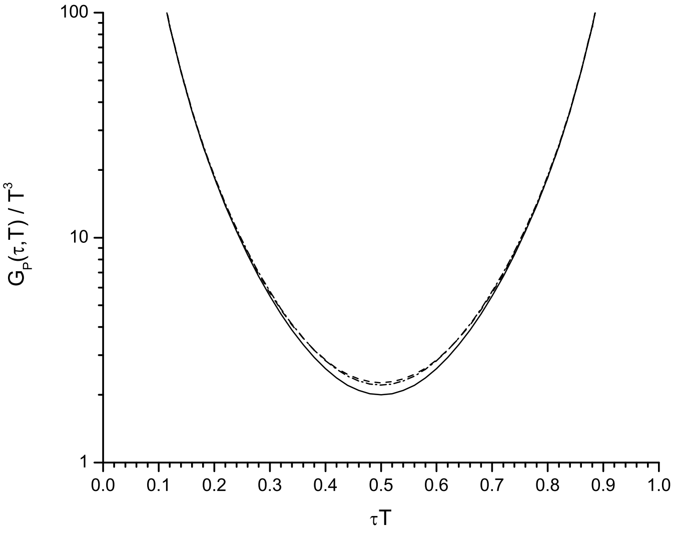

Figure 2.10: Values of $G_P(\tau, T)/T^3$ are shown for $T/T_c = 1.5$ [dashed line], $T/T_c = 3.0$ [dashed-dotted line], and $T/T_c = 5.88$ [solid line]. These results were calculated with model 1.

$T/T_c = 6.0$ [dashed-(double)dotted line]. There is a large peak seen in Figs. 2.19-2.21 at about 775 MeV. It is worth noting that the state that evolves from the $\eta'(958)$ with increasing temperature has a mass of about 750 MeV for $T \simeq T_c$. However, an analysis of the mixing angle for the state at 775 MeV shows that it is mainly an $s\bar{s}$ state. Further work is needed to understand the relation between the bound-state spectrum for $T < T_c$ and the resonant structures seen for $T > T_c$.

Since the introduction of temperature-dependent coupling constants for the NJL model is a novel feature of our work, we provide arguments in this section to justify their introduction. We make reference to Fig. 1.3 of Ref. (12). That figure shows the behavior of the ratio ϵ/T^4 and $3P/T^4$ for the pure gauge sector

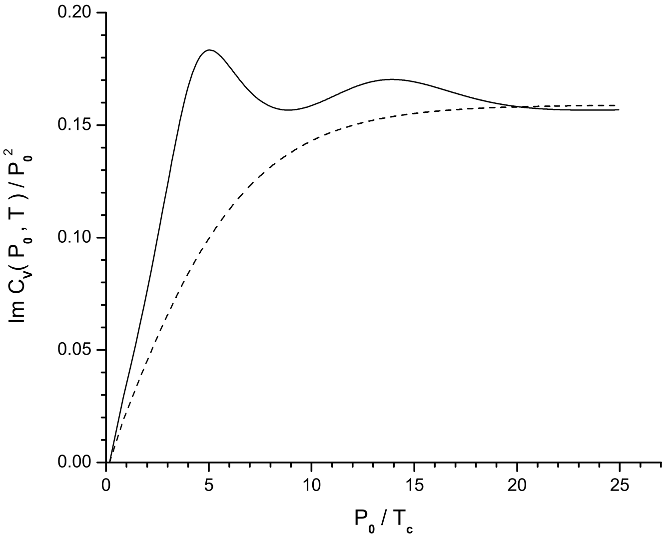

Figure 2.11: Values of $\mathrm{Im}\, C_V(P_0, T)/P_0^2$ are shown for $T/T_c = 1.5$. (See the caption of Fig. 2.4.)

of QCD. Here ϵ is the energy density and P is the pressure. Ideal gas behavior implies $\epsilon = 3P$. The values of ϵ/T^4 and $3P/T^4$ are compared to the value $\epsilon_{SB}/T^4 = 8\pi^2/15$ for an ideal gluon gas. It may be seen from the figure that at $T = 3T_c$ there are still significant differences from the ideal gluon gas result. Deviations from ideal gas behavior become progressively smaller with increasing T/T_c and could be considered to be relatively unimportant for $T/T_c > 5$.

The use of our energy-dependent coupling constants is meant to be consistent with the approach to asymptotic freedom at high temperature. In order to understand this feature in our model, we can calculate the correlator with *constant* values of G_{00}, G_{88} and G_{08} and with $G_{00}(T) = G_{00}[1 - 0.17\,T/T_c]$, etc. (In this work we use $G_{00} = 8.09$ GeV^{-2}, $G_{88} = 13.02$ GeV^{-2} and $G_{08} = -0.4953$ GeV^{-2}.)

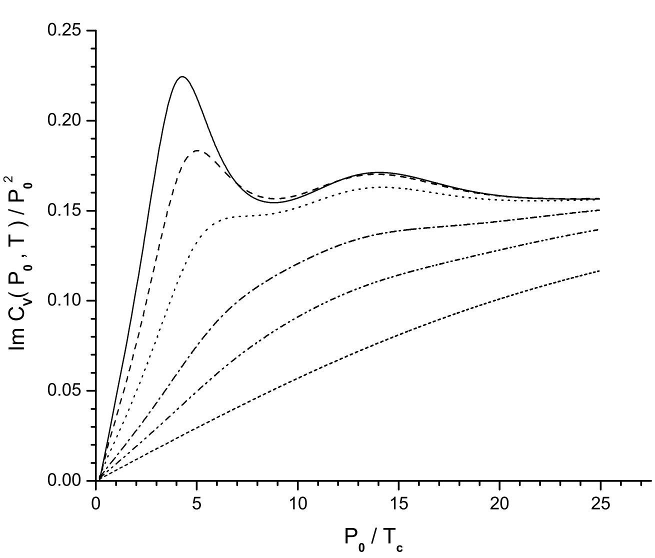

Figure 2.12: Values of $\operatorname{Im} C_V(P_0, T)/P_0^2$ are shown for model 1 and for various temperatures. (See the caption of Fig. 2.5.)

We now consider the values of $\operatorname{Im} C_{88}(P^2)$ for $T/T_c = 4.0$. In Fig. 2.22 we show the values of $\operatorname{Im} C_{88}(P^2)$ calculated in our model with temperature-dependent coupling constants as a dashed line. The dotted line shows the values of the correlator for $G_{00} = G_{88} = G_{08} = 0$, while the solid line shows the values when the coupling constants are kept at their values at $T = 0$. We see that we have some resonant behavior in the case the constants are temperature independent.

In Fig. 2.23 we show similar results for $T/T_c = 5.88$. Here the temperature-dependent coupling constants are equal to zero, so that the lines corresponding to the dashed and dotted lines of Fig. 2.22 coincide. The solid line again shows some resonant behavior at a value of T/T_c, where we expect only very weak interactions associated with asymptotic freedom. We conclude that the model

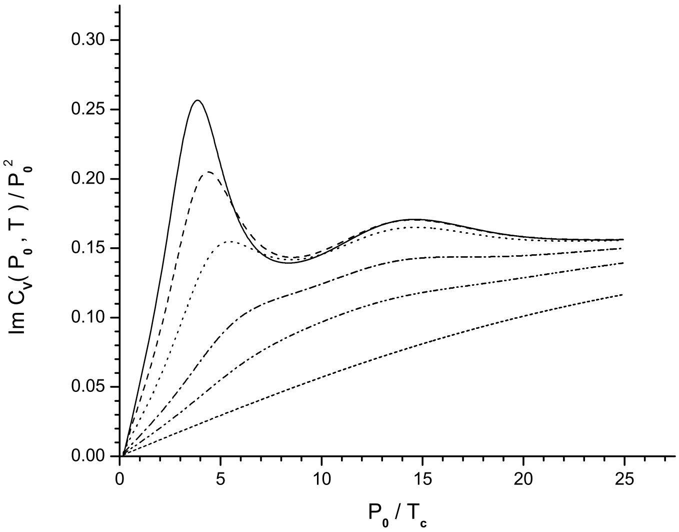

Figure 2.13: Values of $\mathrm{Im}\, C_V(P_0, T)/P_0^2$ are shown for model 2 and for various temperatures. (See the caption of Fig. 2.5.)

with constant values of the coupling constants yields unacceptable results, while our model, which has temperature-dependent coupling constants, behaves as one may expect, when the results of lattice simulations of QCD thermodynamics are taken into account.

2.5 Comparison of Our Results with the Results Obtained in Lattice Simulation of QCD

We believe is of interest to supplement lattice studies of hadronic current correlation functions with calculations made using chiral Lagrangian models of the type considered in this work. We have made some progress in exhibiting results for such correlators in the present study. However, it is difficult to make

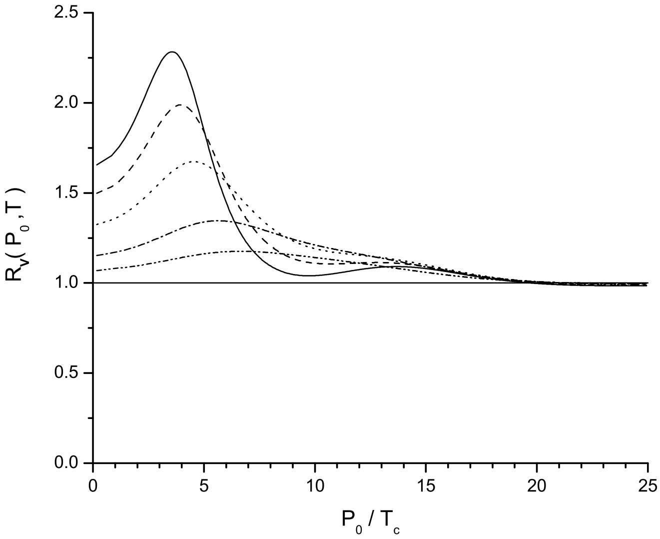

Figure 2.14: Same caption as Fig. 2.6, except that we show $R_V(P_0, T) = \mathrm{Im}C_V(P_0, T)/\mathrm{Im}C_V^{(0)}(P_0, T)$.

a definitive comparison of our results and the results obtained for the spectral functions in the lattice simulations, since those results are accompanied by large errors. Also, it is somewhat difficult to understand why the different behavior seen for $G_V(\tau, T)/T^3$ and $G_P(\tau, T)/T^3$ in Ref. (2), leads to values for $\sigma_P(\omega, T)/\omega^3$ and $\sigma_V(\omega, T)/\omega^3$ that are rather similar (1; 2; 3). On the other hand, the chiral Lagrangian model provides a systematic study, which may yield some guidance for further studies of lattice QCD.

While it may be premature to compare our results for the spectral functions with those given in literature, the errors for the Euclidean-time correlation functions are small. Therefore, in this section we will make an extensive comparison of our results with those presented in Ref. (2).

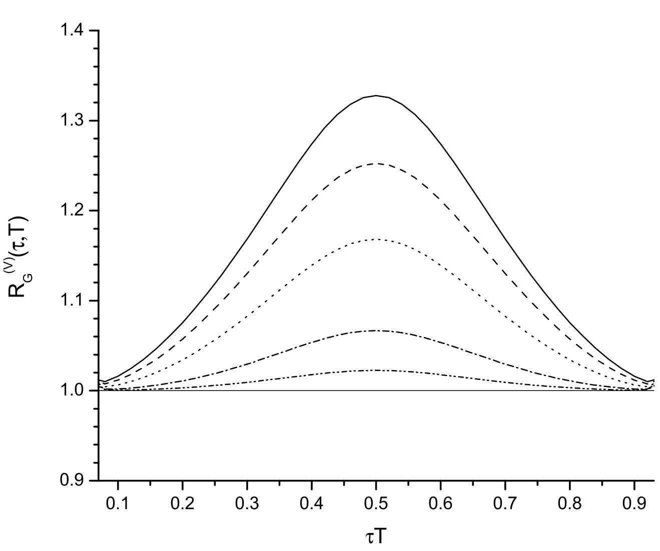

Figure 2.15: Values of $R_G^{(V)}(\tau, T)$ are shown for values of $T/T_c = 1.2$ [solid line], $T/T_c = 1.5$ [dashed line], $T/T_c = 2.0$ [dotted line], $T/T_c = 3.0$ [dashed-dotted line], and $T/T_c = 4.0$ [double dot-dashed line]. For $T/T_c = 5.88$, $R_G^{(V)}(\tau, T) = 1$.

2.5.1 Euclidean-Time Correlators of Pseudoscalar Hadronic Currents

In Fig. 2.5 we show the values of $\mathrm{Im}C_P(P_0, T)/P_0^2$. The large peak at $T/T_c = 1.2$ has its origin in the properties of a pion-like mode that is present after deconfinement has taken place. We note that no resonance is seen for $T/T_c = 3.0$ [dot-dashed line], but resonance behavior is present for $T/T_c = 1.5$ [dashed line] and $T/T_c = 2.0$ [dotted line].

Before we proceed, it is useful to discuss the properties of the integral in Eq. (2.1). We wish to show that the calculation of $G_P(\tau, T)$ is sensitive to the properties of $\sigma_P(\omega, T)$ for relatively small ω, when $\tau T \sim 0.5$. On the other hand,

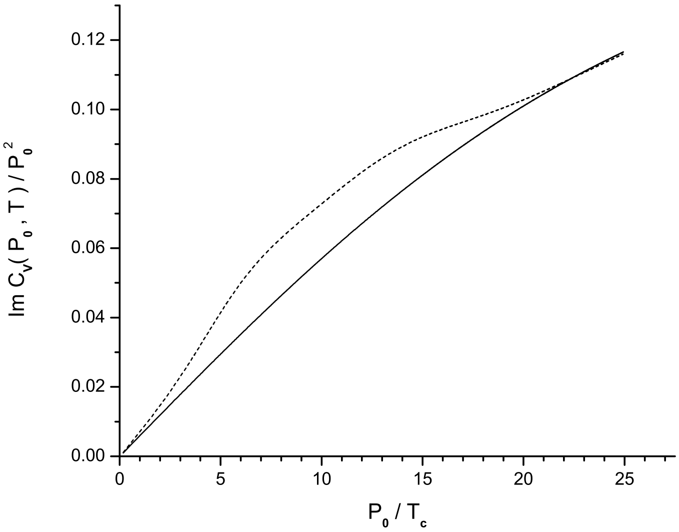

Figure 2.16: Values of $\mathrm{Im}\, C_V(P_0, T)/P_0^2$ are shown for $T/T_c = 5.88$. The dashed line represents the result when $G_V(T) = G_V = 11.46$ GeV^{-2}. The solid line is the result for $G_V(T) = 0$, which is characteristic of models 1 and 2, when $T/T_c = 5.88$. The solid line, therefore, represents the values of Im $\tilde{J}_V(P_0, T)/P_0^2$ for $T/T_c = 5.88$.

when τT is small (or near 1), the integral is sensitive to the values of $\sigma_P(\tau, T)$ for large ω, where $\sigma_P(\tau, T)$ increases as ω^2 and is largely model independent. These features may be seen in Fig. 2.24, where the solid line represents our calculated values of $\sigma_P(\tau, T) = (1/\pi)\mathrm{Im}C_P(\omega, T)$ for $T = 1.5\,T_c$. The dashed line shows $K(\omega, \tau, T)$ for $\tau T = 0.5$, while the dotted and dot-dashed lines show $K(\omega, \tau, T)$ for $\tau T = 0.05$ and $\tau T = 0.10$, respectively. We note that the $1/\omega$ singularity in $K(\omega, \tau, T)$ for small ω is compensated by the behavior of the spectral function at small ω, $\sigma_P(\omega, T) \sim \omega$. These remarks also pertain to the calculation of $G_V(\tau, T)$

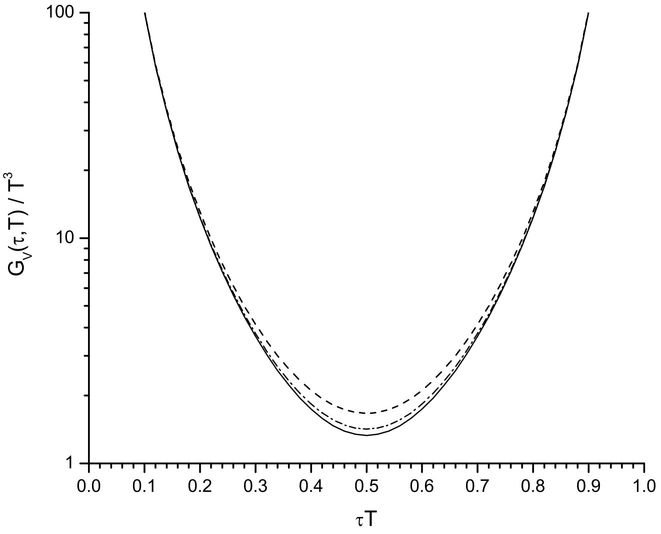

Figure 2.17: Values of $G_V(\tau,T)/T^3$ are shown for $T/T_c = 1.5$ [dashed line], $T/T_c = 3.0$ [dashed-dotted line], and $T/T_c = 5.88$ [solid line]. These results were calculated with model 1.

made using $\sigma_V(\omega,T)$.

In Fig. 2.25 we show the data we have taken from Ref. (2) as squares. The solid line shows the result of our calculation of $G_P(\tau,T)/T^3$, as obtained from our calculated values of $\sigma_P(\omega,T)$ at $T = 1.5\,T_c$. The deviation of our calculation from the data for $\tau T \simeq 0$ or $\tau T \simeq 1$ is inconsequential, given our remarks made in the previous paragraph. We also show the result for the case $G_P(T) = G_P = 13.49\,\mathrm{GeV}^{-2}$ as a dotted curve. When comparing the solid curve and the dotted curve we see evidence for the temperature dependence we have used: $G_P(T) = G_P[1 - 0.17(T/T_c)]$. (We have obtained the value $G_P = 13.49\,\mathrm{GeV}^{-2}$ by calculating the pion mass at $T = 0$ in our model.)

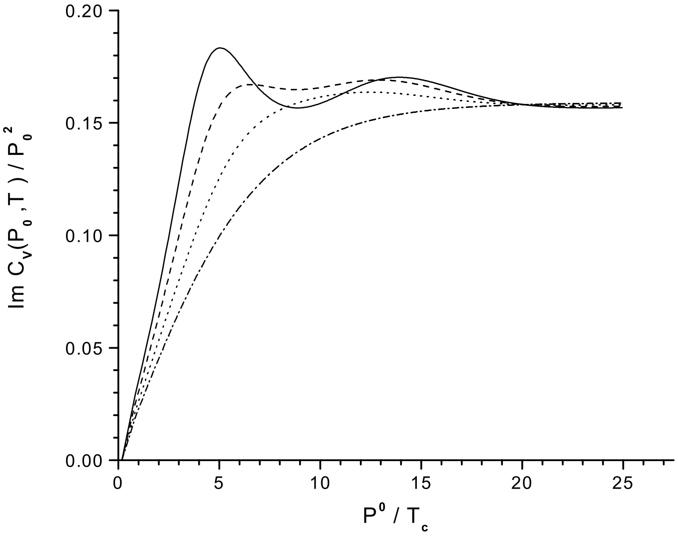

Figure 2.18: Values of $\mathrm{Im}\, C_V(P_0, T)/P_0^2$ are shown for $T/T_c = 1.5$ with $G_V = 11.46$ GeV^{-2} [solid line], $G_V = 8.00$ GeV^{-2} [dashed line], $G_V = 4.00$ GeV^{-2} [dotted line] and $G_V = 0.0$ GeV^{-2} [dot-dashed line]. Here, we have used model 1.

In Fig. 2.26 we show, as a solid line, our result for $G_P(\tau, T)/T^3$ at $T = 3.0\, T_c$. In this case the fit to the data taken from Ref. (2) is poor. Therefore, we have investigated the case in which $G_P(T) = 0$ and show the result as a dashed line in Fig. 2.26. The fit to the data of Ref. (2) is improved somewhat. We may suggest that the suppression of $G_P(T)$ at large temperatures may be greater than that given by the form we have used, $G_P(T) = G_P[1 - 0.17(T/T_c)]$.

In Fig. 2.27 we again consider the value $T = 3.0\, T_c$. In this case, the solid line is the result obtained when $G_P(T) = 0$, while the dotted line results when we use a constant value for $G_P(T) = G_P = 13.49\,\mathrm{GeV}^{-2}$. We may compare our

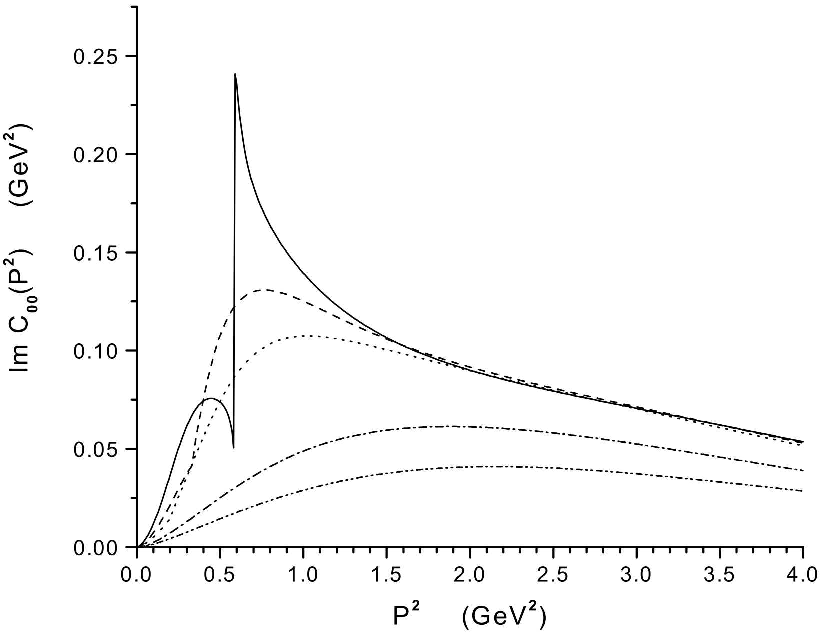

Figure 2.19: The imaginary part of the pseudoscalar-isoscalar correlator $C_{00}(P^2)$ is shown. Here, $T/T_c = 1.2$ [solid line], 1.6 [dashed line], 2.0 [dotted line], 4.0 [dashed-dotted line] and 6.0 [dashed-(double)dotted line]. In this work we use $G_{00} = 8.09$ GeV^{-2}, $G_{88} = 13.02$ GeV^{-2} and $G_{08} = -0.4953$ GeV^{-2}.

results for the spectral functions to those obtained using the MEM procedure and depicted in Ref. (2). One essential difference is that we do not see the resonant behavior reported there for $T = 3.0\,T_c$ at a rather high energy of about 2.4 GeV. The peak in $\bar{\sigma}_P(\omega, T)/\omega^2$ for $T = 1.5\,T_c$ is at about 1 GeV in Ref. (2), while for $T = 1.5\,T_c$ our peak in Fig. 2.5 is at about 0.55 GeV.

In estimating the energies of the peaks we have used $T_c = 150$ MeV. However, if we use $T_c = 270$ MeV, which is more appropriate for a lattice calculation without dynamical quarks, the resonant structures would appear at still higher

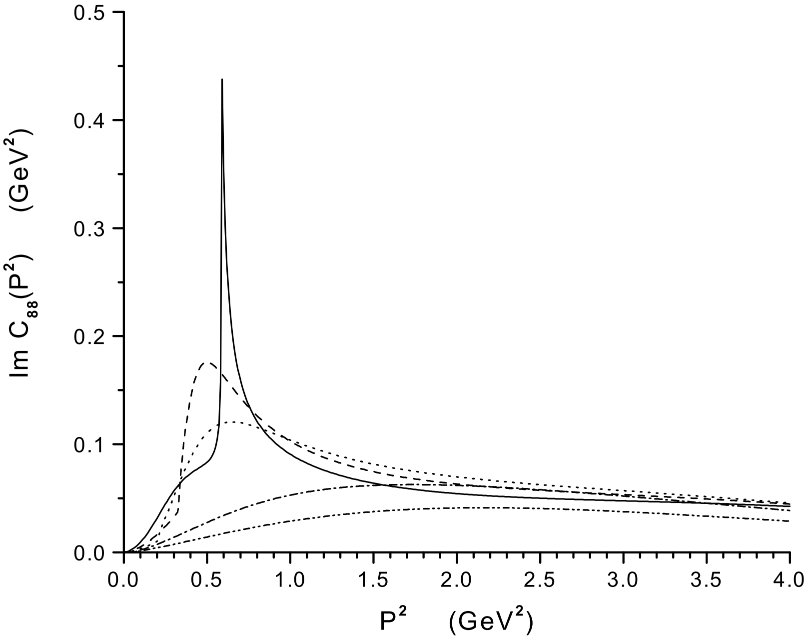

Figure 2.20: The imaginary part of the correlator $C_{88}(P^2)$ is shown. [See caption to Fig. 2.19.]

energy.

2.5.2 Euclidean-Time Correlators of Lorentz-Vector Hadronic Currents

In Fig. 2.12 we present our values of Im$C_V(P_0, T)/P_0^2$, which may be compared to the values of $\bar{\sigma}_V(\omega, T)/\omega^2$ given in Fig. 1 of Ref. (2). In Ref. (2) we find a peak at about 1 GeV for $T = 1.5\,T_c$ and at about 2.5 GeV for $T = 3.0\,T_c$. On the other hand, there is some weak resonant behavior seen for $T = 1.5\,T_c$ [dashed line] in our Fig. 2.12 at about 0.75 GeV which may reflect a residual enhancement due to a ρ-like mode that is present after the confinement-deconfinement transition has

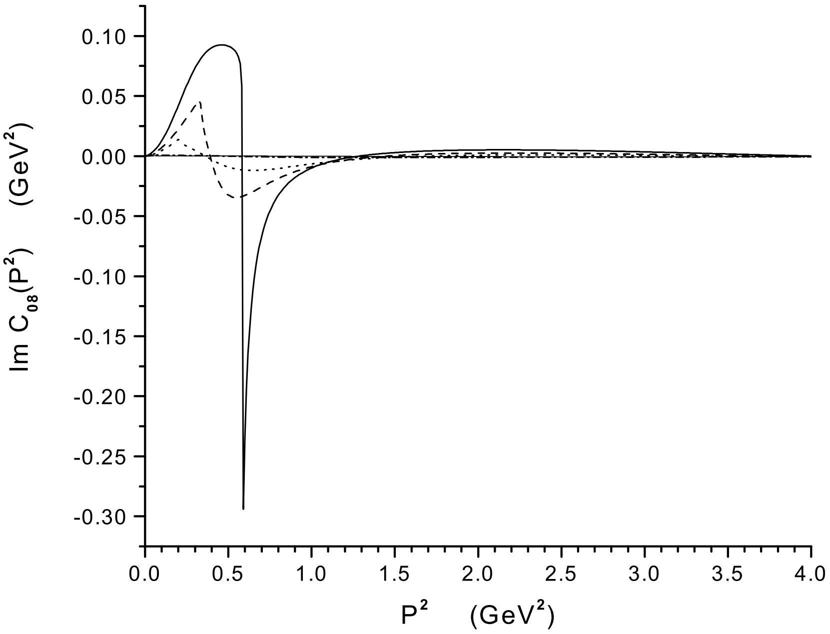

Figure 2.21: The imaginary part of the correlator $C_{08}(P^2)$ is shown. [See caption to Fig. 2.19.]

taken place. At $T = 3.0\,T_c$ [dot-dashed line], we see no resonance enhancement in our work, in contrast to what is obtained by the MEM analysis of Ref. (2).

In Fig. 2.28 we show the data taken from Ref. (2) as squares. Here, there is hardly any difference seen in the data reported for $T = 1.5\,T_c$ and $T = 3.0\,T_c$. In Fig. 2.28, the solid line represents our results for $(3/4)G_V(\tau, T)/T^3$ at $T = 1.5\,T_c$. We only achieve a fair fit to the data, but the fit is decidedly better than that obtained when a constant value of $G_V(T) = G_V = 11.46\,\mathrm{GeV}^{-2}$ is used [dotted line].

In Fig. 2.29 we compare our result for $(3/4)G_V(\tau, T)/T^3$ at $T = 3.0\,T_c$ [solid line] with the data of Ref. (2). Here the fit is better than that of Fig. 2.26.

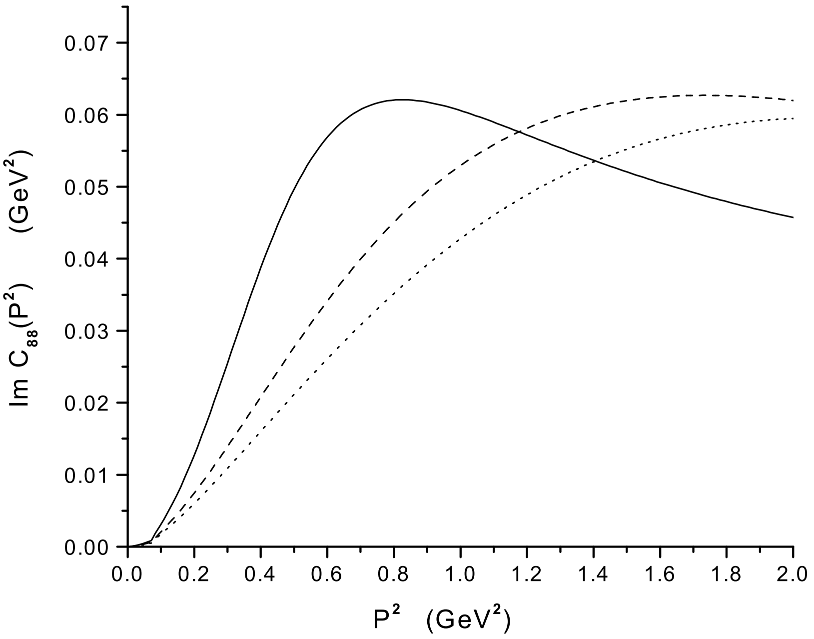

Figure 2.22: The imaginary part of the correlator $C_{88}(P^2)$ is shown for $T/T_c = 4.0$. The dashed line is the result for the temperature-dependent coupling constants of our model, while the solid line represents the results for coupling constants kept at their $T = 0$ values. [See caption to Fig. 2.19.] The dotted line shows the values of the correlator when the coupling constants are set equal to zero.

Again, the use of a constant value of $G_V(T) = G_V = 11.46\,\mathrm{GeV}^{-2}$ yields a poor result. We suggest that our analysis tends to support our choice of temperature-dependent coupling parameters for the NJL model.

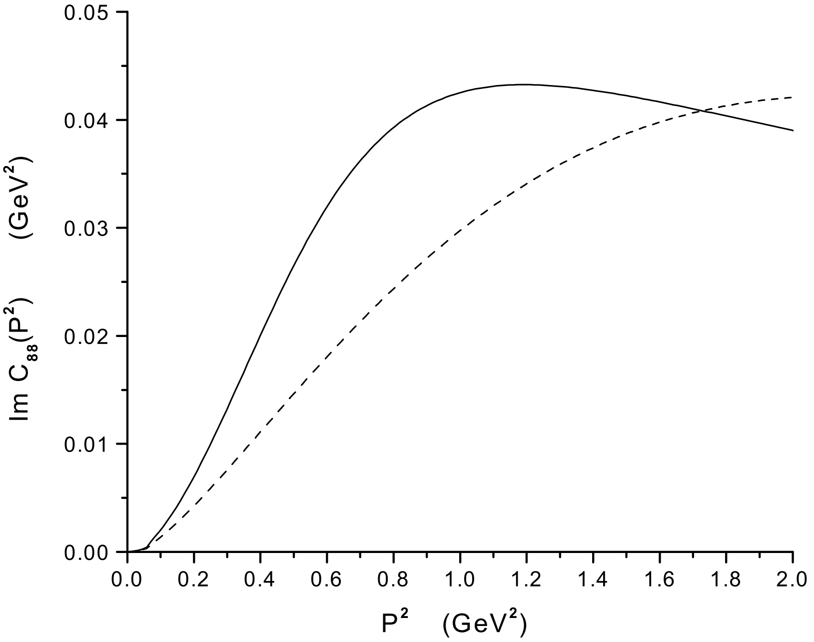

Figure 2.23: The imaginary part of the correlator $C_{88}(P^2)$ is shown for $T/T_c = 5.88$. [See caption to Fig. 2.22.] Here the dashed and dotted lines of Fig. 2.22 coincide.

2.6 Calculation of the Momentum Dependence of Hadronic Current Correlation Functions at Finite Temperature

We have calculated spectral functions associated with hadronic current correlation functions for pseudoscalar and vector currents at finite temperature in previous sections. Good fits were obtained for the spectral functions that were extracted from lattice data by means of the maximum entropy method (MEM). In this section we extend our calculations and provide values for the three-momentum dependence of the vector correlation function at $T = 1.5\,T_c$. We consider the calculation of $\mathrm{Im}J_V(P^0, \vec{P}, T)$. The momenta P^0 and $\vec{P}$ are the val-

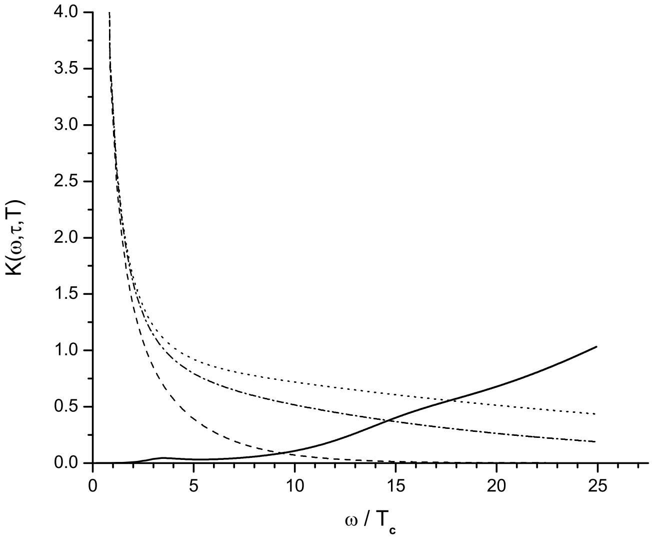

Figure 2.24: Values of $K(\omega,\tau,T)$ are shown for $T=1.5\,T_c$ and $\tau T=0.05$ [dotted line], $\tau T=0.10$ [dot-dashed line], and $\tau T=0.50$ [dashed line]. The solid line represents $(1/\pi)\mathrm{Im}C_P(\omega,T)$. Here, we use the notation $\omega=P_0$ and have put $T_c=0.150\,\mathrm{GeV}$.

ues external to the loop diagram. Internal to the diagram, we have a quark of momentum $k+P/2$ leaving the left-hand vertex and an antiquark of momentum $k-P/2$ entering the left-hand vertex. It is useful to define

$$E_1(k) = \left|\vec{k}+\vec{P}/2\right| \tag{2.46}$$

$$= \left(k^2+\frac{P^2}{4}+kP\cos\theta\right)^{1/2} \tag{2.47}$$

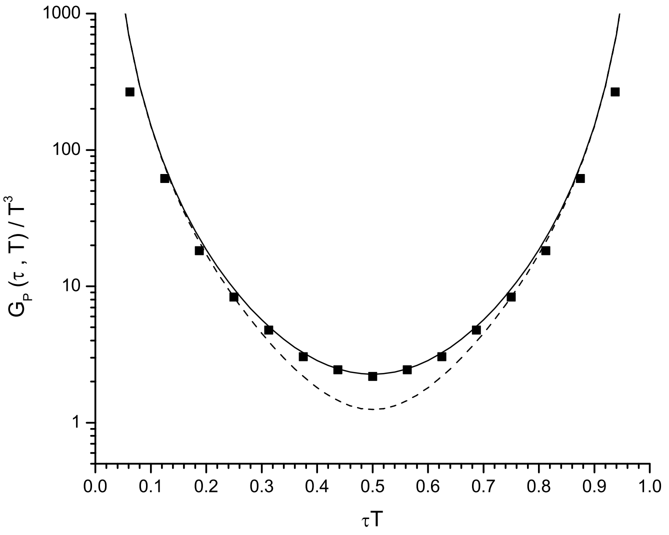

Figure 2.25: Values of $G_P(\tau, T)/T^3$ are shown as a function of τT, with $T = 1.5\,T_c$. The solid line represents the result of our calculation made for $G_P(T) = G_P\,[1 - 0.17\,(T/T_c)]$ with $G_P = 13.49\,\mathrm{GeV}^{-2}$. The dotted line is obtained when we use a constant value $G_P(T) = G_P$. The data (squares) are taken from Ref. (2) for the case $T = 1.5\,T_c$.

and

$$E_2(k) = \left|\vec{k} - \vec{P}/2\right| \tag{2.48}$$

$$= \left(k^2 + \frac{P^2}{4} - kP\cos\theta\right)^{1/2} . \tag{2.49}$$

Here $k = |\vec{k}|$ and $P = |\vec{P}|$.

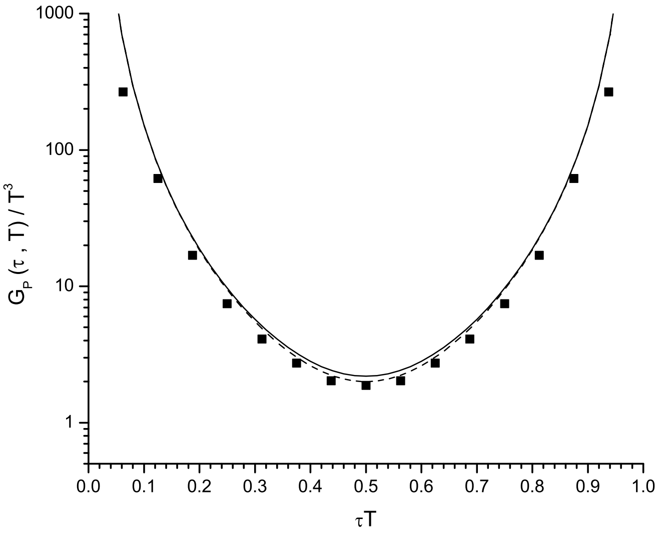

Figure 2.26: Values of $G_P(\tau,T)/T^3$ are shown as a function of τT, for $T = 3.0\,T_c$. The solid line is the result of our calculation made for $G_P(T) = G_P\,[1 - 0.17\,(T/T_c)]$ with $G_P = 13.49\,\mathrm{GeV}^{-2}$, while the dashed line is obtained when we put $G_P(T) = 0$. The data (squares) are taken from Ref. (2) for the case $T = 3.0\,T_c$.

We have

$$\begin{aligned}\mathrm{Im}\,J_V(P^0,\vec{P},T) = \frac{1}{2}N_c\beta_V\,\epsilon(P^0)\int^{k_{max}}\frac{d^3k}{(2\pi)^3}\left(\frac{2\pi}{2E_1(k)2E_2(k)}\right) \\ \times\{[1-n_1(k)-n_2(k)]\delta(P^0-E_1(k)-E_2(k)) \\ -[n_1(k)-n_2(k)]\delta(P^0+E_1(k)-E_2(k)) \\ -[n_2(k)-n_1(k)]\delta(P^0-E_1(k)+E_2(k)) \\ -[1-n_1(k)-n_2(k)]\delta(P^0+E_1(k)+E_2(k))\}\,.\end{aligned} \tag{2.50}$$

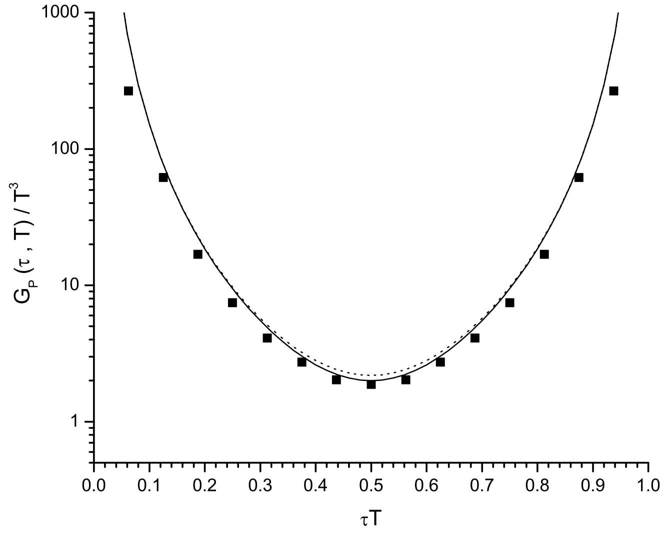

Figure 2.27: Values of $G_P(\tau, T)/T^3$ are shown for $T = 3.0\,T_c$. Here the solid line is the same as the dashed line in Fig. 2.26 and corresponds to $G_P = 0$. The dotted line is obtained when we use the constant value $G_P(T) = G_P = 13.49\,\mathrm{GeV}^{-2}$.

Here,

$$n_1(k) = \frac{1}{e^{\beta E_1(k)} + 1}\,, \tag{2.51}$$

and

$$n_2(k) = \frac{1}{e^{\beta E_2(k)} + 1}\,. \tag{2.52}$$

In Eq. (2.50), the second and third terms cancel and the fourth term does not contribute. It is useful to rewrite $\delta(P^0 - E_1(k) - E_2(k))$ using

$$\delta[f(\cos\theta)] = \frac{2}{\left|\frac{\partial f}{\partial \cos\theta}\right|_x}\delta(\cos\theta - x)\,, \tag{2.53}$$

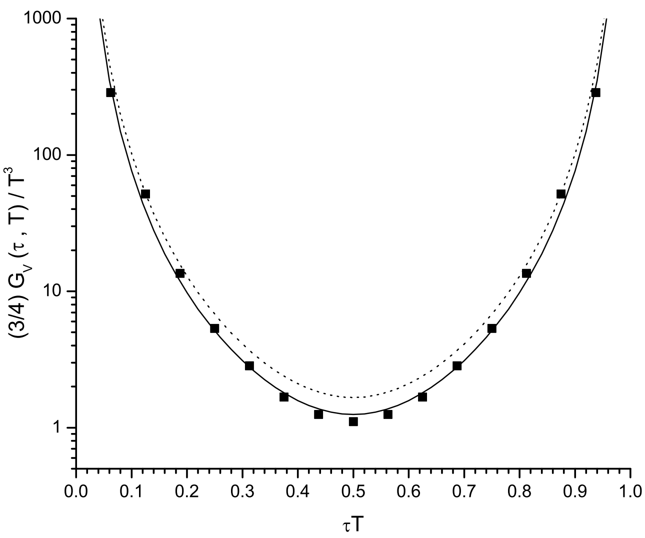

Figure 2.28: Values of $(3/4)G_V(\tau, T)/T^3$ are shown for $T = 1.5\,T_c$. Here, the solid line represents the result when we use $G_V(T) = G_V\,[1 - 0.17\,(T/T_c)]$ with $G_V = 11.46\,\mathrm{GeV}^{-2}$. The dotted line is obtained when we use a constant value of $G_V(T) = G_V = 11.46\,\mathrm{GeV}^{-2}$. The data (squares) are taken from Ref. (2) for the case $T = 1.5\,T_c$.

where

$$\begin{aligned} x^2 &= \cos^2\theta \\ &= \frac{4P_0^2(k^2 + P^2/4) - P_0^4}{4k^2P^2}\,. \end{aligned} \tag{2.54}$$

We find

$$\left|\frac{\partial f}{\partial \cos\theta}\right| = \frac{1}{2}kP\left|\frac{E_1(k) - E_2(k)}{E_1(k)E_2(k)}\right|\,, \tag{2.55}$$

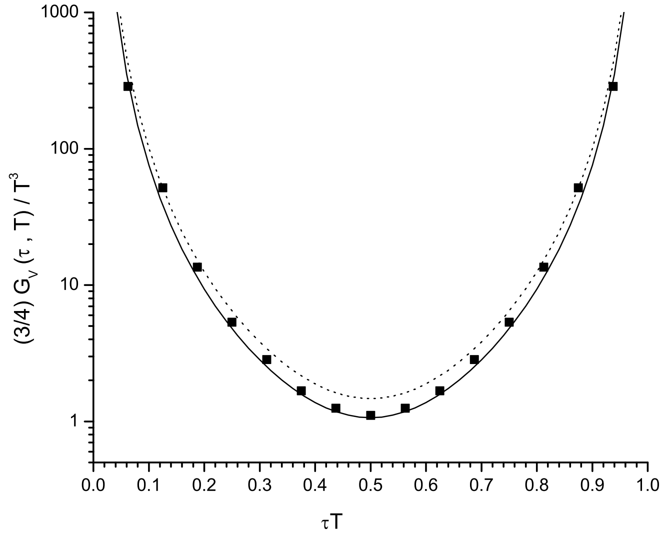

Figure 2.29: Values of $(3/4)G_V(\tau,T)/T^3$ are shown for $T = 3.0\,T_c$. Here, the solid line represents the result when we use $G_V(T) = G_V\,[1 - 0.17\,(T/T_c)]$ with $G_V = 11.46\,\mathrm{GeV}^{-2}$. The dotted line is obtained when we use a constant value of $G_V(T) = G_V = 11.46\,\mathrm{GeV}^{-2}$. The data (squares) are taken from Ref. (2) for the case $T = 3.0\,T_c$.

and obtain

$$\begin{aligned} \mathrm{Im}\, J_V(P^0,\vec{P},T) &= \frac{1}{2} N_c \beta_V\, \epsilon(P^0)(2\pi)^2 \int^{k_{max}} \frac{k^2 dk}{(2\pi)^3} \\ &\int \frac{1}{2E_1(k)E_2(k)} [1 - n_1(k) - n_2(k)] \left| \frac{\partial f(\cos\theta)}{\partial \cos\theta} \right| \\ &\qquad \times \delta(\cos\theta - x) d(\cos\theta)\,. \end{aligned} \tag{2.56}$$

We note there is a singularity when $E_1(k) = E_2(k)$. That occurs when $\cos\theta = 0$ or $\theta = \pi/2$. For our calculations we eliminate the point with $\theta = \pi/2$ when evaluating the angular integral over $d(\cos\theta)\delta(\cos\theta - x)$ in the last expression. We obtain

$$\begin{aligned}\mathrm{Im}\, J_V(P^0,\vec{P},T) = N_c\beta_V\,\epsilon(P^0)\frac{4\pi^2}{(2\pi)^3}\int^{k_{max}} k^2 dk \qquad (2.57)\\ \times\, \frac{1-n_1(k)-n_2(k)}{kP|E_1(k)-E_2(k)|}\bigg|_x\,,\end{aligned}$$

where x is obtained from Eq. (2.54),

$$x = \frac{P^0}{kP}\left[k^2 + \frac{P^2}{4} - \frac{P_0^2}{4}\right]^{1/2} \qquad (2.58)$$

In the calculations we take $T_c = 270$ MeV, since we have usually made comparison to lattice calculations made in the quenched approximation.

In Fig. 2.30 we present $\sigma(\omega)/\omega^2$, for various values of $|\vec{P}|$, as function of ω^2. Comparison may be made to the lattice data shown in Fig. 2.31 (19). (We note that our calculation does not reproduce the second peak in the lattice data which is known to be a lattice artifact.) The curves shown in Fig. 2.30 are given for values of $|\vec{P}|$ ranging from 0.10 GeV to 2.10 GeV in steps of 0.20 GeV. For these calculations we have used $k_{max} = 1.22\,\mathrm{GeV}$. Our results for the various values of $|\vec{P}|$ given in Fig. 2.30 may be compared to Fig. 20 of Ref. (20). We see that the results calculated by completely different methods are similar.

The coordinate-dependent correlator $C(z)$ is defined as

$$C(z) = \frac{1}{2}\int_{-\infty}^{\infty} dP_z e^{iP_z z}\int_0^{\infty} d\omega\frac{\sigma(\omega,0,0,P_z)}{\omega}\,. \qquad (2.59)$$

We may also use the form

$$C(z) = \frac{1}{4}\int_{-\infty}^{\infty} dP_z e^{iP_z z}\int_0^{\infty} dP^2\,\frac{\sigma(P^2,0,0,P_z)}{P^2}\,. \qquad (2.60)$$

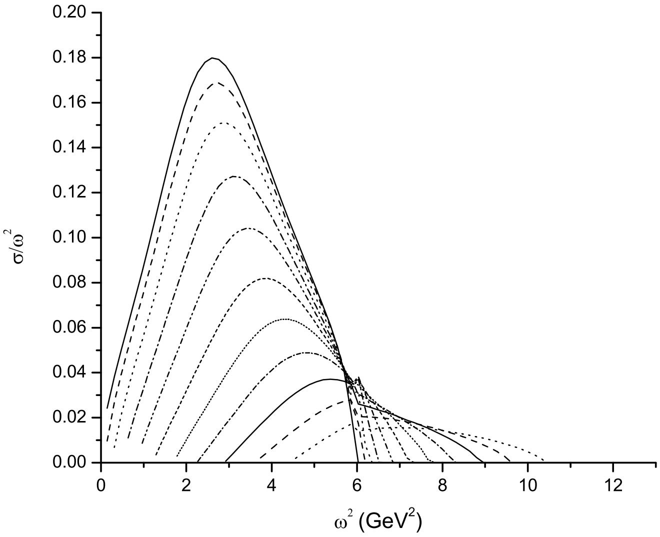

Figure 2.30: The imaginary part of the correlator $\sigma(\omega)/\omega^2$ is shown for various values of $|\vec{P}|$ as a function of ω^2. Starting with the topmost curve the values of $|\vec{P}|$ in GeV units are 0.10, 0.30, 0.50, 0.70, 0.90, 1.10, 1.30, 1.50, 1.70, 1.90 and 2.10. Here we have used $G_S = 1.2$ GeV^{-2} and $k_{max} = 1.22$ GeV.

We have used the results of our calculations which were presented in Fig. 2.30 to calculate $C(z)$ of Eq. (2.60). The result of that calculation is shown in Fig. 2.32. We note that the simple assumption for the behavior of this correlator that is usually made, $C(z) \sim \exp[-m_{sc}z]$, is born out in our calculation for $1\,\mathrm{GeV}^{-1} < z < 3\,\mathrm{GeV}^{-1}$. For the study of charmonium on the lattice, values found for the screening mass are given in Ref. (20).

For the result shown in Fig. 2.32 we obtain a screening mass of 1.02 GeV which may be compared to the value of πT=1.27 GeV. The dotted line represents an

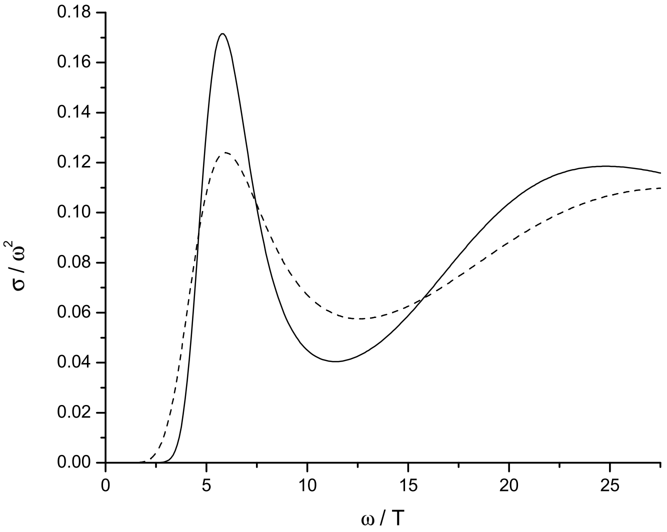

Figure 2.31: The spectral functions σ/ω^2 for vector states obtained by MEM are shown (19). The solid line is for $T/T_c = 1.5$ and the dashed line is for $T/T_c = 3.0$. The second peak is a lattice artifact.

exponential fit to our result. We have shown in an earlier work that exponential behavior with the appropriate screening mass may be obtained for the full range of z values if quite small values of k_{max} (of the order of 0.4 GeV) are used (21). Finally, we note that an extensive discussion of screening masses appears in Ref. (22).

2.7 Discussion and Conclusions

It is of interest to obtain further insight into the results shown in Figs. 2.26 and 2.27. To that end, we show various calculations made for $\mathrm{Im}C_P(P_0,T)/P_0^2$

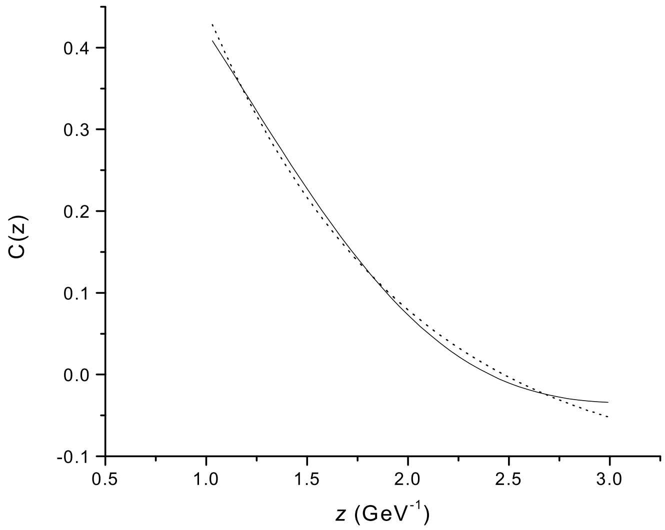

Figure 2.32: The correlation function $C(z)$ defined in Eq. (2.60) is shown. The dotted line represents a fit using an exponential function.

in Fig. 2.33. There, for $T = 3.0\,T_c$, the solid line is the result of our model, the dotted curve corresponds to the use of a constant value of the coupling parameter $G_P(T) = G_P = 13.49\,\mathrm{GeV}^{-2}$, while the dashed line is the result for $G_P(T) = 0$. A comparison of the solid curve and the dashed curve leads to some understanding of the results shown in Fig. 2.26, while a comparison of the dotted curve and the dashed curve leads to further understanding of the results shown in Fig. 2.27. Similar results are given for $\mathrm{Im}C_V(P_0,T)/P_0^2$ in Fig. 2.34. For that figure, a comparison of the solid curve and the dashed curve gives some insight into the results shown in Fig. 2.29, where the dotted line corresponds to $G_V(T) = G_V = 11.46\,\mathrm{GeV}^{-2}$ and the solid curve represents the results of our model.

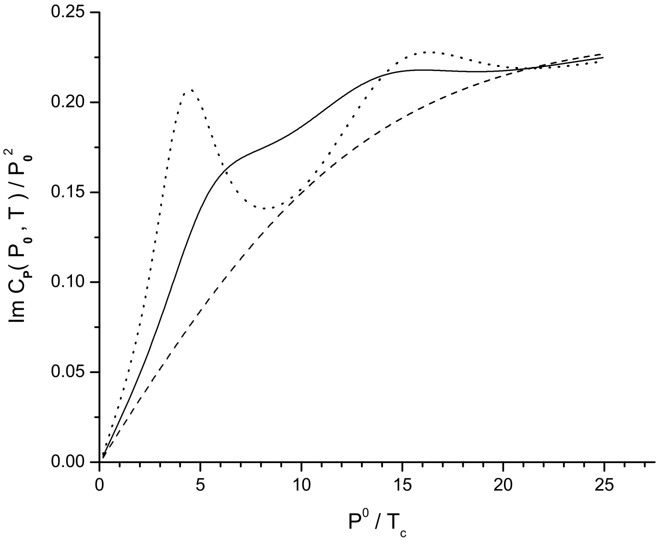

Figure 2.33: Values of $\mathrm{Im}\, C_P(P_0, T)/P_0^2$ are shown for $T = 3.0\, T_c$. The solid line is the result of our model with temperature-dependent coupling parameters, the dotted line is obtained in the absence of the temperature dependence ($G_P(T) = G_P = 13.49\,\mathrm{GeV}^{-2}$), and the dashed line represents the result for $G_P(T) = 0$.

We now return to the pseudoscalar case for $T = 1.5\, T_c$. In Fig. 2.35 we show $\mathrm{Im} C_P(P_0, T)/P_0^2$ for our model [solid line], for $G_P(T) = 0$ [dashed line], and for the case $G_P(T) = G_P = 13.49\,\mathrm{GeV}^{-2}$. We recall that our model, with the temperature-dependent coupling parameter, gave rise to a excellent fit to the data, as seen in Fig. 2.25. It is also of interest to present values of $\sigma_P(\omega, T) = (1/\pi)\mathrm{Im} C_P(\omega, T)/\omega^2$ for $T = 1.5\, T_c$. In Fig. 2.36, the result of our model is shown as a solid line, the dot-dashed line is for $G_P(T) = 0$, and the dotted line is obtained when $G_P(T) = G_P = 13.49\,\mathrm{GeV}^{-2}$. It is seen, that for small values

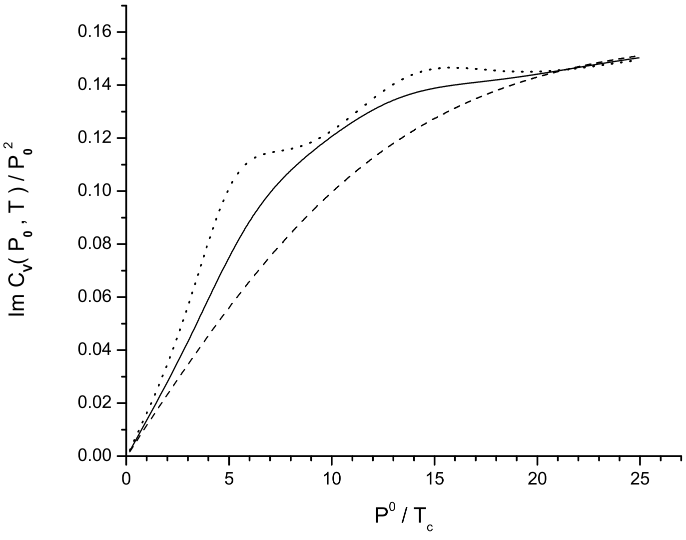

Figure 2.34: Values of $\mathrm{Im}\, C_V(P_0, T)/P_0^2$ are shown for $T = 3.0\, T_c$. The solid line is the result of our model with temperature-dependent coupling parameters, the dotted line is obtained in the absence of the temperature dependence ($G_V(T) = G_V = 11.46\,\mathrm{GeV}^{-2}$), and the dashed line represents the result for $G_V(T) = 0$.

of P_0, on the whole, the dotted line lies below the other curves, giving rise to the behavior seen in Fig. 2.25 for $\tau T \simeq 0.5$.

It is worth mentioning that we have some additional evidence of the utility of temperature-dependent coupling parameters for the NJL model. We note that the confinement-deconfinement transition takes place in the range $150\,\mathrm{MeV} \leq T_c \leq 170\,\mathrm{MeV}$ for QCD with dynamical quarks. We then inspect Fig. 5 of Ref. (23), where the constituent quark mass of the NJL model is presented as a function of temperature for the case of a temperature-independent coupling

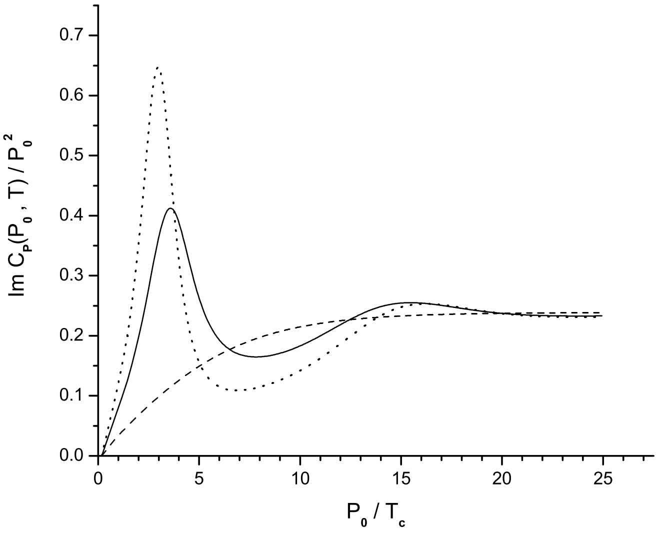

Figure 2.35: Values of $\mathrm{Im}\, C_P(P_0, T)/P_0^2$ are shown for $T = 1.5\, T_c$. Here, the solid line is the result of our model, the dashed line represent the result for $G_P(T) = 0$, while the dotted line is obtained when we use $G_P(T) = G_P = 13.49\,\mathrm{GeV}^{-2}$. [See Fig. 2.25 for the values of $G_P(\tau, T)/T^3$ calculated for $T = 1.5\, T_c$, using the values of $\mathrm{Im}\, C_P(P_0, T)/P_0^2$ shown here as the solid and dotted line.]

constant. The mass value is 330 MeV at $T = 0$ and is about $260 - 300$ MeV when $150\,\mathrm{MeV} \leq T \leq 170\,\mathrm{MeV}$. Thus, we do not see the (partial) restoration of the chiral symmetry that is expected for $T \sim T_c$. On the other hand, we see in Fig. 1 of Ref. (10), where we have used a temperature-dependent coupling parameter, that we have $m_u = 364$ MeV at $T = 0$ and $m_u(T)$ in the range of 50 to 100 MeV for $150\,\mathrm{MeV} \leq T \leq 170\,\mathrm{MeV}$. That is much more in accord with the (partial) restoration of chiral symmetry when $T \sim T_c$. If we wish to consider

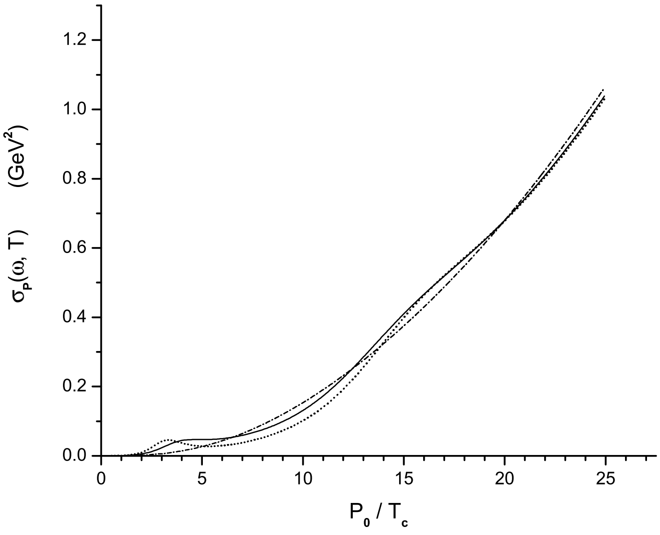

Figure 2.36: Values of $\sigma_P(\omega, T) = (1/\pi)\mathrm{Im}\, C_P(P_0, T)$ are shown for $T = 1.5\, T_c$. Here, the solid line corresponds to our model, with $G_P(T) = G_P\,[1 - 0.17\,(T/T_c)]$, the dot-dashed line is obtained when $G_P(T) = 0$, and the dashed line is for the case $G_P(T) = G_P = 13.49\,\mathrm{GeV}^{-2}$. (See Fig. 2.37.)

the NJL as a useful low-energy model of QCD, it is much easier to discuss the confinement-deconfinement transition if we use temperature-dependent coupling parameters.

For ease of reference,we have calculated the constituent mass of the up quark using the equation for the temperature-dependent constituent mass given in Ref. (11). We have used a current quark mass of $m^0 = 5.5\,\mathrm{MeV}$ and a momentum cutoff of $\Lambda = 0.631\,\mathrm{GeV}$. In Fig. 2.37, the dotted curve shows the result obtained with $G = 5.691\,\mathrm{GeV}^{-2}$ (in the notation of Ref. (11)). From Fig. 2.37 we see that

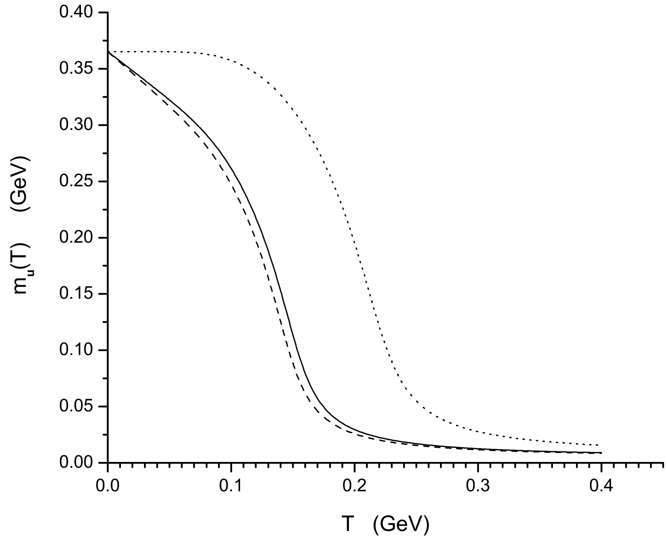

Figure 2.37: We exhibit the values of $m_u(T)$ obtained using Eq. (5.38) of Ref. (11), with $m^0 = 5.50\,\mathrm{MeV}$ and $\Lambda = 0.631\,\mathrm{GeV}$. The dotted curve corresponds to the use of a constant value $G = 5.691\,\mathrm{GeV}^{-2}$, in the notation of Ref. (11). For the solid and dashed curves we have used $G(T) = G\,[1 - 0.17(T/T_c)]$. For the solid curve we have put $T_c = 0.170\,\mathrm{GeV}$, while for the dashed curve, we have used $T_c = 0.150\,\mathrm{GeV}$ in our parametrization of $G(T)$.

at $T = 0.150\,\mathrm{GeV}$, $m_u = 0.318\,\mathrm{GeV}$, while at $T = 0.170\,\mathrm{GeV}$, $m_u = 0.276\,\mathrm{GeV}$. The dashed and solid curves represent the result when $G(T) = G[1 - 0.17(T/T_c)]$. For the solid curve ($T_c = 0.170\,\mathrm{GeV}$), $m_u = 77\,\mathrm{MeV}$ at $T = 0.170\,\mathrm{GeV}$. For the dashed curve ($T_c = 0.150\,\mathrm{GeV}$), $m_u = 54\,\mathrm{MeV}$ at $T = 0.150\,\mathrm{GeV}$. Again, we see that it is much easier to discuss the (partial) restoration of chiral symmetry at the confinement-deconfinement transition when we use the temperature-dependent

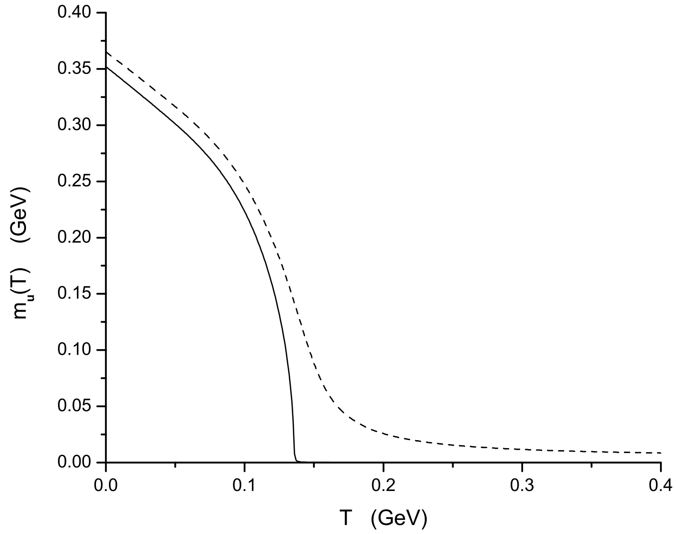

Figure 2.38: Values of $m_u(T)$ are shown. The dashed curve is calculated with $m^0 = 5.50\,\mathrm{MeV}$. Here, $G(T) = G\,[1 - 0.17\,(T/T_c)]$, with $G = 5.691\,\mathrm{GeV}^{-2}$ and $T_c = 0.150\,\mathrm{GeV}$. The solid curve is calculated with the same value of $G(T)$ and T_c, but with $m^0 = 0$. From the solid curve, we see that chiral symmetry is restored at $T = 0.136\,\mathrm{GeV}$ when $m^0 = 0$.

coupling parameters of our model.

It is also of interest to exhibit the role played by the current quark mass. In Fig. 2.38, the dashed curve, which was calculated for $T_c = 0.150\,\mathrm{GeV}$, is the same as the dashed curve in Fig. 2.37. In Fig. 2.38, the solid curve shows the result when $m^0 = 0$. Here, we see restoration of chiral symmetry at $T = 0.136\,\mathrm{GeV}$, when $G(T) = G[1 - 0.17(T/T_c)]$ with $T_c = 0.150\,\mathrm{GeV}$.

We note that the value of $T_c = 0.136\,\mathrm{GeV}$ is still within the uncertainty of the transition temperature for three-flavor QCD. For example, in Ref. (24) the transition temperatures are given for two-flavor and three-flavor QCD. In the latter case, $T_c = 154 \pm 8\,\mathrm{MeV}$, with a suggested systematic error similar to the statistical error, so that $T_c = 154 \pm 8 \pm 8\,\mathrm{MeV}$ (24). (We have used coupling constants determined in our studies of the three-flavor NJL model, so that consideration of the transition temperature for that case is appropriate.)

If we wish to assign a physical interpretation of the parameter T_c in the expression for $G(T)$, we may use $G(T) = G[1 - 0.135(T/T_c)]$ with $T_c = 0.150\,\mathrm{GeV}$. That choice gives rise to restoration of chiral symmetry at $T = T_c = 0.150\,\mathrm{GeV}$ in the NJL model with $m^0 = 0$. If we maintain the value $m^0 = 0$, but use a constant value for $G(T) = 5.691\,\mathrm{GeV}^{-2}$, with $\Lambda = 0.631\,\mathrm{GeV}$, we find restoration of chiral symmetry at $T_c = 208\,\mathrm{MeV}$.

The calculations reported in Figs. 2.37 and 2.38 may also be made using our Gaussian cutoff, $\exp(-\vec{k}^2/\alpha^2)$, with $\alpha = 0.605\,\mathrm{GeV}$. For example, we may consider the dashed curve of Fig. 2.38. If we use the Gaussian cutoff and use $G = 6.004\,\mathrm{GeV}^{-2}$, instead of $G = 5.691\,\mathrm{GeV}^{-2}$, we obtain a curve that is very close to the dashed curve of Fig. 2.38 for $T > 0.080\,\mathrm{GeV}$. However, the mass at $T = 0$ is $382\,\mathrm{MeV}$ instead of $364\,\mathrm{MeV}$ which was the value obtained using the sharp cutoff of $\Lambda = 0.631\,\mathrm{GeV}$ and $G = 5.691\,\mathrm{GeV}^{-2}$.

We have performed what are essentially parameter-free calculations of hadronic spectral functions and have computed the corresponding Euclidean-time correlation functions. The values of the coupling parameters, G_P and G_V, were fixed in calculations of meson properties at $T = 0$. One interesting feature of our analysis is the use of temperature-dependent coupling constants in the NJL model. In the present work, we have provided some justification for the introduction of such constants. Our work suggests that the coupling constants of the NJL model may also be density-dependent, since one expects that high density may play a similar role as high temperature, leading ultimately to a weakly interacting system at high density. We have introduced density-dependent coupling constants in Ref. (25) where we considered the confinement-deconfinement transition in the presence of matter. Since the study of matter at high density is a topic of active investigation (26; 27; 28; 29; 30; 31; 32), our suggestion of density-dependent coupling constants may have important consequences for such studies.

Chapter 3

Calculation of the Excitations of Dense Quark Matter at Zero Temperature

3.1 Introduction

A good deal is known concerning the properties of QCD at finite temperature. However, the properties of QCD at finite matter density are not well known, since the lattice simulations of QCD at finite chemical potential are only in a relatively early stage of development (33; 34; 35; 36; 37; 38). We have studied the excitations of the quark-gluon plasma by calculating hadronic current correlation functions at finite temperature in last chapter. In this chapter we report upon calculations of such correlators at finite matter density in the deconfined phase. As in the large number of applications of the NJL model and related models to the study of high-density matter (26; 27; 28; 29), we do not consider explicit gluon degrees of freedom. Our calculations do not take into account the formation of diquark condensates associated with color superconductivity. One reason for not studying diquark condensates and related matters at this time is that we have some concerns as to the use of the NJL model with constant values of the coupling constants at high density or high temperature. It is easier to discuss the matter of temperature-dependent effective coupling constants than to discuss density-dependent coupling constants, since a good deal is known about QCD thermodynamics at finite temperature. We denote the critical temperature for the confinement-deconfinement transition as T_c and have used $T_c = 170$ MeV in our work. From studies of a pure gluon system in QCD, it is found that at high temperatures one approaches a weakly interacting system slowly, with some nonperturbative effects still present at temperatures $T = 3T_c$ or $4T_c$ (12). For definiteness, we assume that we can neglect nonperturbative effects for $T \gtrsim 6T_c$. For these high temperatures we would expect to be able to calculate hadronic current correlators using the NJL model and obtain the result expected in lowest-order perturbation theory at energies for which the effective Lagrangian may be used. (In that regard, we limit our applications to $P^2 < 4$ GeV^2.) However, we found in our studies that the calculated hadronic current correlations functions had resonant features for $T \sim 6T_c$, when *temperature-independent* coupling constants were used (39). That was one of a number of reasons that we replaced the temperature-independent coupling constants of the NJL model by $G(T) = G[1 - 0.17T/T_c]$. (We remark that other dependence on the parameter T/T_c may be assumed, however, we have only explored the linear dependence described here.) By analogy, we may introduce $G(\rho) = G[1 - \beta\rho/\rho_c]$ where ρ_c is the critical density for the confinement-deconfinement transition. In our earlier work (25) we took $\rho_c = 2.25\rho_{NM}$, where ρ_{NM} is the density of nuclear matter. Our introduction of the parameter β was not done in a systematic fashion in Ref.

(25), but the values used had $\beta \simeq 0.18$. For the present work, we have used the same value of $\rho_c = 2.25\rho_{NM}$ and have taken $\beta = 0.17$. Therefore, for $\rho \gtrsim 6\rho_c$, we have assumed that the system has limited nonperturbative features. Since we are not describing diquark condensation in this work, we might limit ourselves to consideration of ρ values larger than, but not too different from ρ_c. However, here we will also study the larger values of $\rho \lesssim 6\rho_c$ in order to gain information about a possible density-dependence of the NJL coupling constants, in analogy to what was done in the case of our finite temperature studies (10; 17; 39).

Our calculations are made for zero values of the chemical potential. Thus, we can present our results for hadronic current correlators for various values of ρ/ρ_c. When calculations are made in that manner, we can present a particularly transparent discussion of the role of "Pauli blocking".

Our model for quark matter is that of two ideal Fermi gases of up and down quarks with Fermi momentum p_F. The density of the quark matter is given by $\rho_q = (2N_c/3\pi^2)p_F^3$, where $N_c = 3$ is the number of colors. That expression may be put in contrast to the expression for the density of nuclear matter, $\rho_{NM} = (2/3\pi^2)k_F^3$, where k_F is the Fermi momentum of the ideal gas of nucleons. With our form of $G(\rho)$ in our model, we have assumed that at $\rho_q = 5.88\rho_c = 13.2\rho_{NM}$ the system is weakly interacting, since $G(\rho) = 0$ at that density. We may ask if we can apply the NJL model at such high densities. When $\rho_q = 13.2\rho_{NM}$, we find $p_F = 1.64k_F = 0.44$ GeV. Here we have used $k_F = 0.268$ GeV for nuclear matter.

Since a typical (sharp) three-momentum cutoff for the standard NJL model is 0.631 GeV (8; 39), we see that it is still possible to use the NJL model at the largest density considered here. (It is possible to extend the range of application by using a larger momentum cutoff for the NJL model. However, the cutoff is usually fixed by fitting the pion decay constant, so that the range of variation of the cutoff parameter is limited (8; 9; 11).)

In this work we study the correlators which involve the excitation of states with the quantum numbers of the ρ, π, f_0 and η mesons. In the following discussion ρ will represent the density of quark matter. However, we will sometimes use the notation ρ_q for that quantity.

3.2 Calculation of Hadronic Current Correlation Functions

The Lagrangian we use in our calculations is defined as before. [See Eq. (2.3).] In this work we make use of the density-dependent constituent quark masses that were calculated in Refs. (25; 40) using a mean-field approximation. The up (or down) quark mass $m_u(\rho)$ is rather small for $\rho > \rho_c$ and has relatively little effect when calculating the hadronic current correlators. The strange quark mass for $\rho \gtrsim \rho_c$ is approximately constant with $m_s(\rho) \simeq 440$ MeV (25). (The difference between the behavior of the up and down quark mass and that of the strange quark mass is due to the fact that the quark matter we consider is nonstrange.)

In Fig. 3.1a we show the basic vacuum-polarization diagram of the NJL

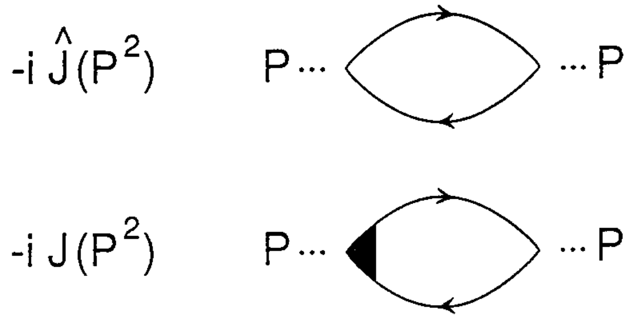

Figure 3.1: (a) The basic vacuum polarization diagram of the NJL model is shown. The lines represent a constituent quark and antiquark of mass $m(\rho_q)$. (b) The filled region represents a confinement vertex used for calculations made for $\rho \leq \rho_c$ (25).

model, where the lines denote either constituent quarks or antiquarks. (In Fig. 3.1b we show the introduction of a confinement vertex which is needed in our studies for $T < T_c$ or $\rho < \rho_c$. Since we are considering the deconfined phase, we can disregard the confinement vertex for this work.) With reference to Fig. 3.1, we denote the quark momentum as $P/2 + k$ and the antiquark momentum as $-P/2 + k$, and work in the frame where $\vec{P} = 0$.

In forming the imaginary parts of the vacuum polarization functions, the quark and antiquark go on mass shell, so that we have $\vec{k}^2 = (P^0)^2/4 - m^2(\rho)$. It is easy to see that there is a minimum value of $|\vec{k}| = p_F$, where p_F is the Fermi momentum of either the up or down ideal quark gases. For smaller values of $|\vec{k}|$ the excitation is "blocked" by the Pauli Principle. Thus, we see that in calculating the imaginary part of a vacuum polarization function, one obtains nonzero values above a minimum value of P^0, $(P^0)^2_{min} = 4(p_F^2 + m^2(\rho))$, where p_F is related to the quark density by the expression $p_F^3 = (3\pi^2/2N_c)\rho_q$, given earlier.

We now consider the imaginary part of the vacuum polarization function corresponding to scalar currents. We find in the case an up (or down) quark is excited

$$\mathrm{Im} J^S(P^2) = N_c \frac{P_0^2}{4\pi} \left(1 - \frac{4m_u^2(\rho)}{P_0^2}\right)^{3/2} e^{-\vec{k}^2/\alpha^2} \theta[P_0^2 - 4(p_F^2 + m_u^2(\rho))] \,. \tag{3.1}$$

This expression contains a factor of 2 arising from the flavor trace. Here $\vec{k}^2 = P_0^2/4 - m_u^2(\rho)$ appears in the Gaussian regulator. (We have used Gaussian regulators for most of our calculations made using the NJL model. The value of $\alpha = 0.605$ GeV yields results that are similar to those obtained with the sharp three-momentum cutoff parameter $\Lambda = 0.631$ GeV.) For pseudoscalar mesons, we may use Eq. (3.1) with the phase-factor exponent of 3/2 replace by 1/2 when the constituent mass is small (17). The real parts of the vacuum polarization functions are obtained by means of a dispersion relation.

We now consider the calculation of density-dependent hadronic current correlation functions. The general form of the correlator is a transform of a time-ordered product of currents,

$$C(P^2, \rho) = i \int d^4x e^{ip\cdot x} \ll \mathrm{T}(j(x)j(0) \gg \,, \tag{3.2}$$

where the double bracket is a reminder that we are considering the finite density case.

For the study of pseudoscalar states, we may consider currents of the form $j_{P,i}(x) = \bar{q}(x)i\gamma_5\lambda^i q(x)$ where, in the case of the π mesons, $i = 1, 2$, and 3. For the study of pseudoscalar-isoscalar mesons, we again introduce $j_{P,i}(x) = \bar{q}(x)i\gamma_5\lambda^i q(x)$, but here $i = 0$ for the flavor-singlet current and $i = 8$ for the flavor-octet current.

In the case of the π mesons, the correlator may be expressed in terms of the basic vacuum polarization function of the NJL model, $J_P(P^2, \rho)$. Thus,

$$C_\pi(P^2, \rho) = J_P(P^2, \rho)\frac{1}{1 - G_\pi(\rho)J_P(P^2, \rho)}\,, \tag{3.3}$$

where $G_\pi(\rho)$ is the coupling constant appropriate for our study of the π mesons. (We have found $G_\pi(0) = 13.49$ GeV^{-2} by fitting the pion mass in a calculation made at $\rho = 0$.)

For a study of the correlators related to the ρ meson, we introduce conserved vector currents $j_{\mu,i}(x) = \bar{q}(x)\gamma_\mu\lambda^i q(x)$ with $i = 1, 2$ and 3. In this case we define

$$J_\rho^{\mu\nu}(P^2, \rho) = \left(g^{\,\mu\nu} - \frac{P^{\,\mu}P^{\,\nu}}{P^2}\right) J_\rho(P^2, \rho)\,, \tag{3.4}$$

taking into account the fact that the current $j_{\mu,i}(x)$ is conserved. We may then use the fact that

$$\begin{align} J_\rho(P^2, \rho) &= \frac{1}{3}g_{\mu\nu}J_\rho^{\mu\nu}(P^2, \rho) \tag{3.5}\\ &= \frac{2N_c}{3}\left[\frac{P_0^2 + 2m_u^2(\rho)}{4\pi}\right]\left(1 - \frac{4m_u^2(\rho)}{P_0^2}\right)^{1/2} e^{-\vec{k}^{\,2}/\alpha^2}\theta[P_0^2 - 4(p_F^2 + m_u^2(\rho))] \tag{3.6}\\ &\simeq \frac{2}{3}J_\pi(P^2, \rho) \tag{3.7} \end{align}$$

and write the approximate expression

$$\mathrm{Im}J_\rho(P^2,\rho) \simeq \frac{2}{3}\frac{N_c P_0^2}{4\pi}\left(1-\frac{4m_u^2(\rho)}{P_0^2}\right)^{1/2} e^{-\vec{k}^{\,2}/\alpha^2}\theta[P_0^2-4(p_F^2+m_u^2(\rho))] \quad (3.8)$$

for the vacuum polarization function of the vector-isovector currents. Here $\vec{k}^2 = P_0^2/4 - m_u^2(\rho)$ appears in the Gaussian regulator. Thus, we define

$$C_\rho(P^2) = J_\rho(P^2)\left[\frac{1}{1-G_V(\rho)J_\rho(P^2)}\right], \quad (3.9)$$

where we have suppressed reference to the density dependence of the correlator and the vacuum polarization function. We have used $G_V(\rho) = G_V[1-0.17\rho/\rho_c]$ with $G_V = 11.46$ GeV^{-2} for the calculations reported here.

The calculation of the correlator for scalar-isoscalar states is more complex, since there are both flavor-singlet and flavor-octet states to consider. We may define polarization functions for u, d and s quarks: $J_u(P^2,\rho)$, $J_d(P^2,\rho)$ and $J_s(P^2,\rho)$. These functions do not contain the factor of 2 arising from the flavor trace that was introduced when calculating $\mathrm{Im}J_\pi(P^2,\rho)$, $\mathrm{Im}J^S(P^2,\rho)$ and $\mathrm{Im}J_\rho(P^2,\rho)$ earlier in this section.

In terms of these polarization functions we may then define

$$J_{00}(p^2,\rho) = \frac{2}{3}[J_u(p^2,\rho)+J_d(p^2,\rho)+J_s(p^2,\rho)], \quad (3.10)$$

$$J_{08}(p^2,\rho) = \frac{\sqrt{2}}{3}[J_u(p^2,\rho)+J_d(p^2,\rho)-2J_s(p^2,\rho)], \quad (3.11)$$

and

$$J_{88}(p^2,\rho) = \frac{1}{3}[J_u(p^2,\rho)+J_d(p^2,\rho)+4J_s(p^2,\rho)]. \quad (3.12)$$

We also introduce the matrices

$$J(p^2,\rho) = \begin{bmatrix} J_{00}(p^2,\rho) & J_{08}(p^2,\rho) \\ J_{80}(p^2,\rho) & J_{88}(p^2,\rho) \end{bmatrix}, \tag{3.13}$$

$$G(\rho) = \begin{bmatrix} G_{00}(\rho) & G_{08}(\rho) \\ G_{80}(\rho) & G_{88}(\rho) \end{bmatrix}, \tag{3.14}$$

$$C(p^2,\rho) = \begin{bmatrix} C_{00}(p^2,\rho) & C_{08}(p^2,\rho) \\ C_{80}(p^2,\rho) & C_{88}(p^2,\rho) \end{bmatrix}, \tag{3.15}$$

and write the matrix relation

$$C(p^2,\rho) = J(p^2,\rho)[1 - G(\rho)J(p^2,\rho)]^{-1}\,. \tag{3.16}$$

3.3 Results of Numerical Calculations of Pseudoscalar and Vector Hadronic Current Correlation Functions, $C_\pi(P^2)$ and $C_\rho(P^2)$

In Fig. 3.2 we present values calculated for Im$C_\pi(P^2)$ for $\rho/\rho_c = 1.2$, 2.0, 3.0, 4.0 and 5.88. The threshold for each curve is given by $(P^0)^2_{min} = 4(p_F^2 + m_u^2(\rho_q))$. If $\rho_c = 2.25\rho_{NM}$, we have

$$p_F = \left(\frac{2.25}{N_c}\frac{\rho}{\rho_c}\right)^{1/3} k_F\,, \tag{3.17}$$

where k_F is the Fermi momentum of nuclear matter, $k_F = 0.286$ GeV. Thus, when $\rho/\rho_c = 5.88$, we find $p_F = 0.439$ GeV, which is less than the standard three-dimensional (sharp) cutoff of $\Lambda = 0.631$ GeV that is often used for the

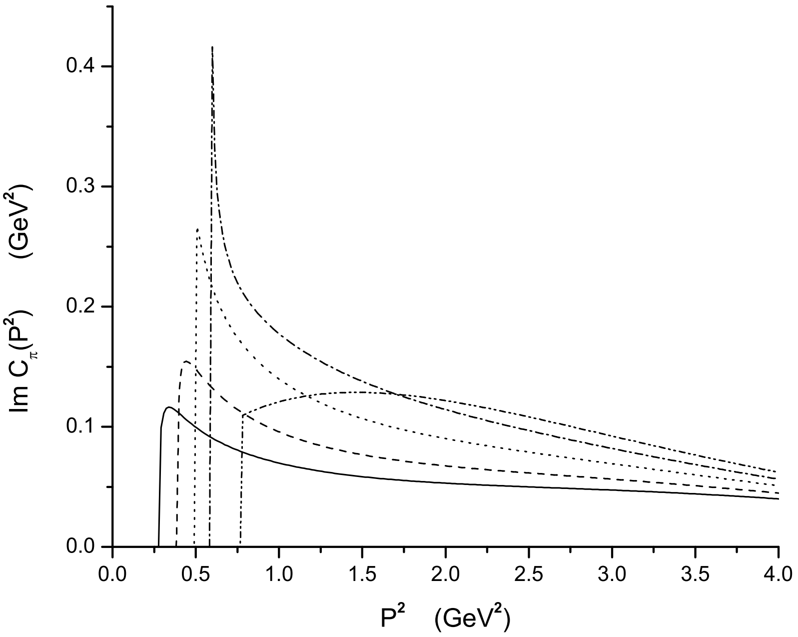

Figure 3.2: The figure presents values of Im$C_\pi(P^2)$ for various values of ρ/ρ_c. Here, ρ/ρ_c = 1.2 [solid line], 2.0 [dashed line], 3.0 [dotted line], 4.0 [dashed-dotted line] and 5.88 [dashed-(double)dotted line]. We have used G_π = 13.51 GeV^{-2}.

NJL model. It is seen from the figure that there are significant nonperturbative effects, except at $\rho/\rho_c = 5.88$, where Im$C_\pi(P^2)$ = Im$J_\pi(P^2)$. The last result follows, since $G_\pi(\rho) = 0$ for $\rho/\rho_c = 5.88$.

In Fig. 3.3 we show the results of a similar calculation of Im$C_\rho(P^2)$. Here the thresholds for the various curves are the same as those seen in Fig. 3.2.

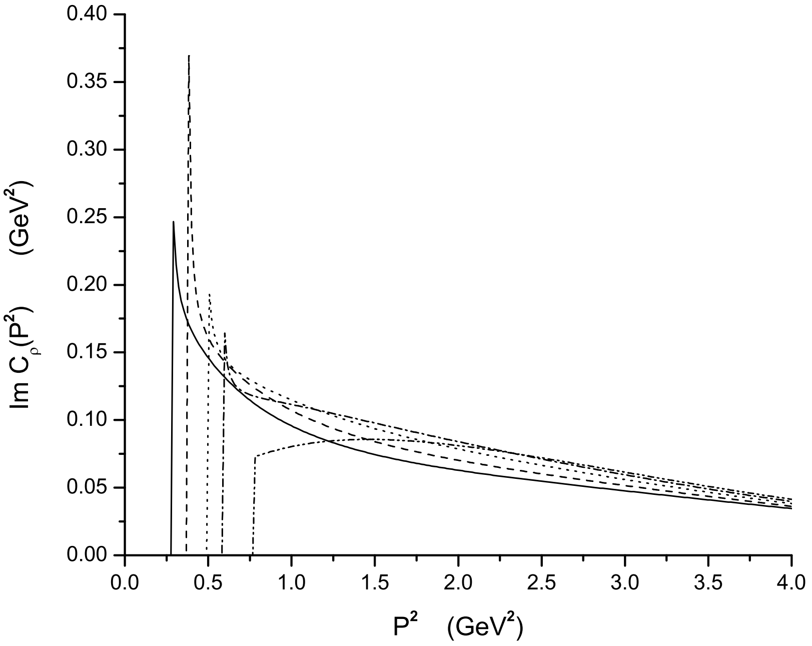

Figure 3.3: The figure shown the values of Im$C_\rho(P^2)$. [See the caption of Fig. 3.2.] Here we have used $G_V = 11.46$ GeV^{-2}.

3.4 Results of Numerical Calculations of Scalar and Pseudoscalar Correlators $C_{f_088}(P^2)$ and $C_{\eta 88}(P^2)$

In the case of the correlator of pseudoscalar-isoscalar currents, the components $C_{\eta 00}(P^2)$, $C_{\eta 08}(P^2) = C_{\eta 80}(P^2)$ and $C_{\eta 88}(P^2)$ are all important. We choose to show Im$C_{\eta 88}(P^2)$ in Fig. 3.4 for the values of ρ/ρ_c = 1.5, 2.0, 3.0, 4.0 and 5.88. The resonant structures have rather small widths when compared to the features seen in Fig. 3.2 and 3.3. It is also worth noting that each curve has two thresholds, one corresponding to $m_u(\rho)$ and the other corresponding to $m_s(\rho)$. Thus, we have $(P^0)^2_{min} = 4[p_F^2 + m_u^2(\rho)]$ or $(P^0)^2_{min} = 4[p_F^2 + m_s^2(\rho)]$.

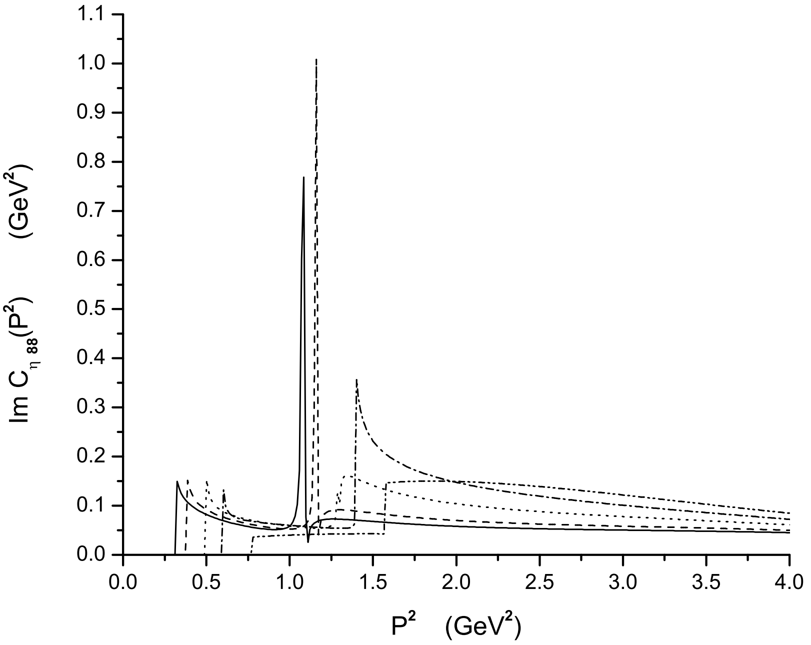

Figure 3.4: The figure shows the values calculated for the imaginary part of the correlator of pseudoscalar, flavor-octet currents Im$C_{\eta 88}(P^2)$. Here, $\rho/\rho_c = 1.5$ [solid line], 2.0 [dashed line], 3.0 [dotted line], 4.0 [dashed-dotted line], and 5.88 [dashed-(double)dotted line].

Similar remarks pertain for the scalar current correlators, $C_{f_0 00}(P^2)$, $C_{f_0 08}(P^2) = C_{f_0 80}(P^2)$ and $C_{f_0 88}(P^2)$. The values of Im$C_{f_0 88}(P^2)$ are shown in Fig. 3.5 for various values of ρ/ρ_c. Note that the resonances seen in that figure are quite narrow. That is probably due to the different phase space behavior for the f_0 (p-wave) and η (s-wave).

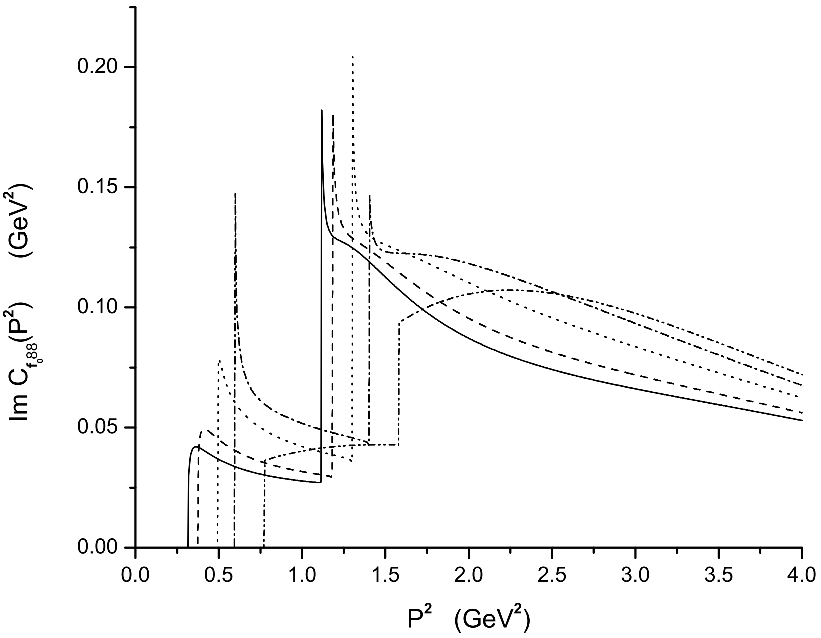

Figure 3.5: The values of the imaginary part of the correlator of scalar, flavor-octet hadronic currents, Im$C_{f_0 88}(P^2)$ is shown. [See caption of Fig. 3.4.]

3.5 Results of Numerical Calculations with Density-Dependent and Density-Independent NJL Coupling Constants

In this section we are interested in presenting some evidence for the density-dependent coupling constants used in our work (25). (As noted earlier, the argument is more easily made when we introduce temperature-dependent coupling constants, since much more is known concerning QCD thermodynamics at finite temperature than at finite density.) In the case of finite density, we have assumed that the system is weakly interacting at $\rho = 5.88\rho_c$ with $\rho_c = 2.25\rho_{NM}$. (Other values for ρ_c could be used, but here we will continue to explore the consequences

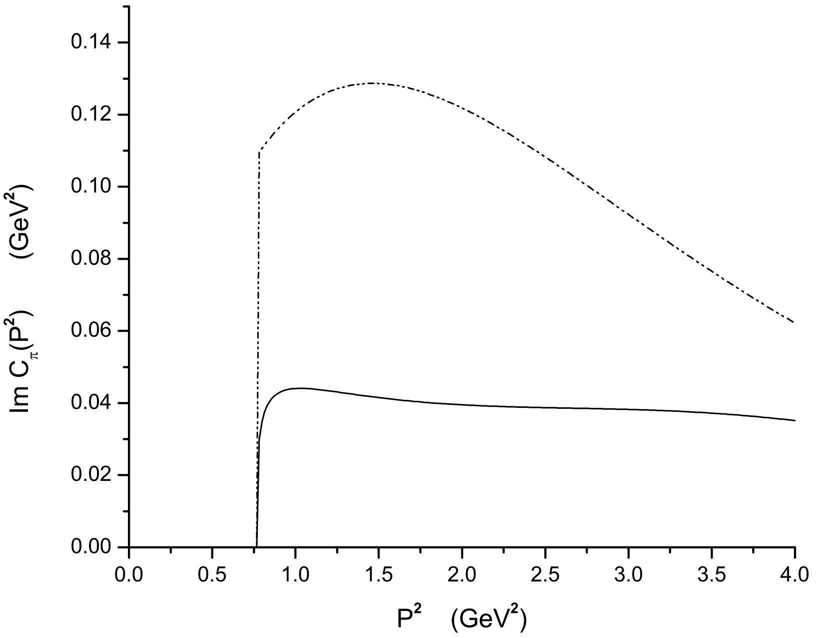

Figure 3.6: The solid line shows the values of Im$C_\pi(P^2)$ for the case of density-independent NJL coupling constants. The dashed-(double)dotted line represents Im$C_\pi(P^2)$ calculated with the density-dependent coupling constants $G_\pi(\rho) = G_\pi[1 - 0.17\rho/\rho_c]$ for $\rho/\rho_c = 5.88$.

of the choice made in our earlier work (25).) In Fig. 3.6 we compare the results of our model for Im$C_\pi(P^2)$ at $\rho/\rho_c = 5.88$ with the results obtained when we use a constant value for G_π. As seen in the figure, there is about a factor of 3 difference in the result of the two calculations. The difference in the two calculated results for Im$C_\rho(P^2)$ seen in Fig. 3.7 is not quite as marked as that seen in Fig. 3.6, but is still significant.

In Fig. 3.8 we compare the results for Im$C_{\eta 88}(P^2)$ at $\rho/\rho_c = 5.88$ for the two

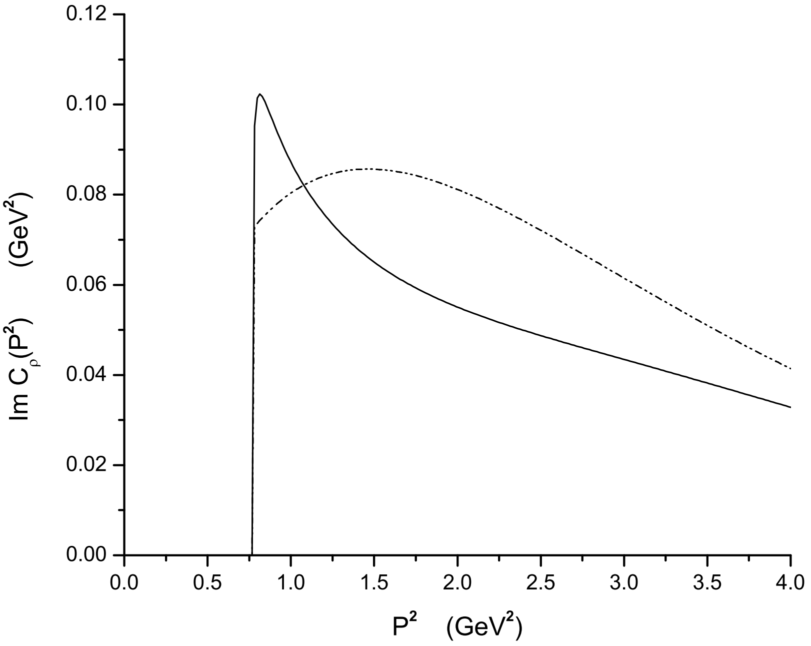

Figure 3.7: The solid line shows the values of Im$C_\rho(P^2)$ for the case of density-independent NJL coupling constants. The dashed-(double)dotted line represents Im$C_\rho(P^2)$ calculated with the density-dependent coupling constants $G_V(\rho) = G_V[1 - 0.17\rho/\rho_c]$ for $\rho/\rho_c = 5.88$.

methods of calculation. A rather dramatic difference is seen in Fig. 3.8, where we see that the calculation with constant values of G_{00}^P, G_{08}^P and G_{88}^P leads to a resonance at $P^2 = 1.53$ GeV^2. In Fig. 3.9 we show similar results for Im$C_{f_0 88}(P^2)$ with a resonance at $P^2 = 1.58$ GeV^2 in the case that constant values of G_{00}^P, G_{08}^P and G_{88}^P are used.

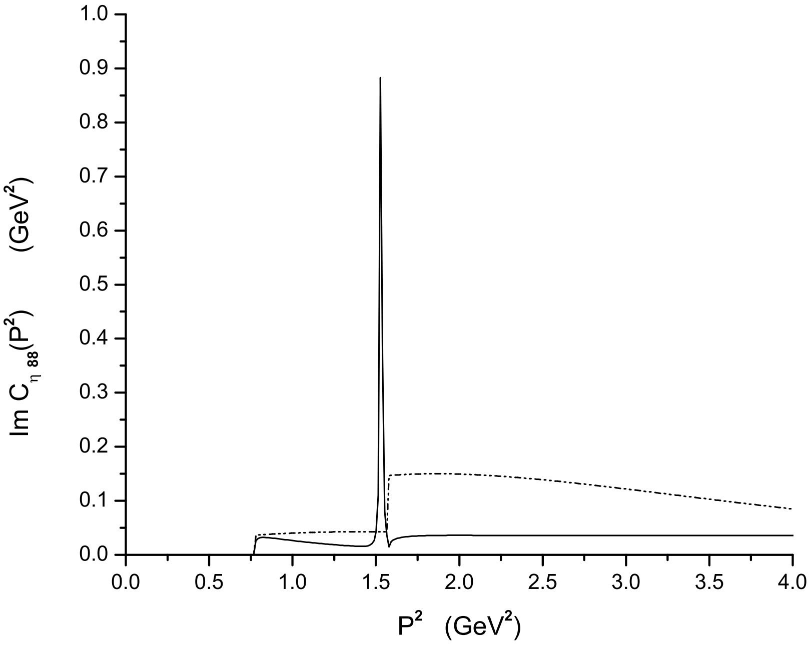

Figure 3.8: The figure shows Im$C_{\eta 88}(P^2)$ calculated for $\rho/\rho_c = 5.88$. The dashed-(double)dotted line is the result of using our density-dependent coupling parameters, while the solid line is the result when density-independent coupling parameters are used.

3.6 Discussion

In this work we have assumed that deconfinement takes place at $\rho_c = 2.25\rho_{NM}$ and that the quark gluon plasma is weakly interacting at $\rho = 5.88\rho_c = 13.2\rho_{NM}$. We have put forth some evidence that the NJL coupling constants should be density dependent to obtain a consistent formalism. We may consider what results would be obtained if we used a larger value of the density for the confinement-deconfinement transition. We have investigated the values of $\rho_c = 3.0\rho_{NM}$,

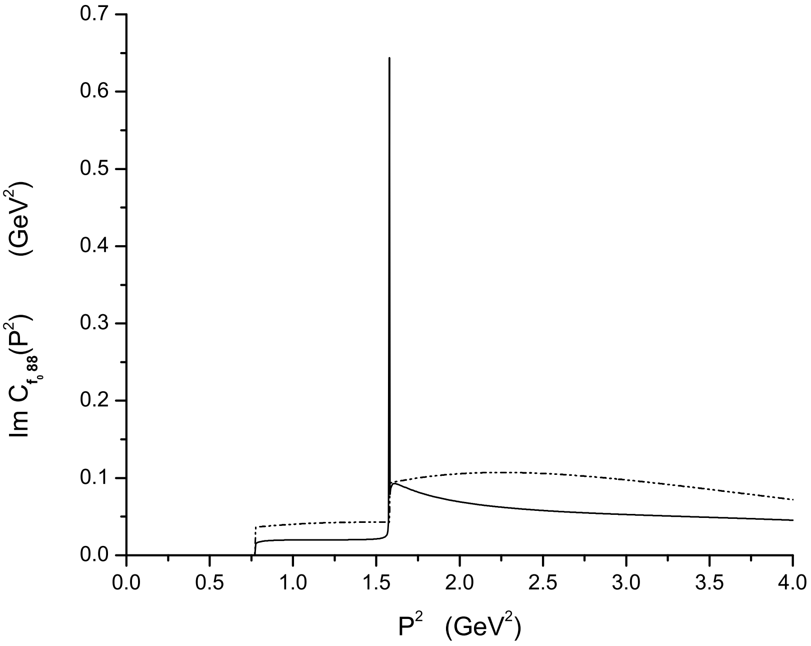

Figure 3.9: The figure shows Im$C_{f_0 88}(P^2)$ calculated for $\rho/\rho_c = 5.88$. [See the caption of Fig. 3.8.]

$\rho_c = 4.0\rho_{NM}$ and $\rho_c = 5.0\rho_{NM}$ and in each case have assumed that the quark-gluon plasma is weakly interacting for $\rho = 6.0\rho_c$. (We should note that, if ρ_c is made large, the value calculated for p_F will become larger than the value of the three-momentum NJL cutoff, $\Lambda = 0.631$ GeV, that is often used. However, our computer code still provides results under that circumstance, since we use a Gaussian regulator.) It is found in all the calculations made at the values of ρ for which we have assumed the system to be weakly interacting, that the values of the correlators calculated with constant values of the coupling constants differ significantly from the results obtained with the density-dependent coupling constants. We suggest that this matter should be resolved before we undertake studies of diquark condensation at high densities and related matters.

One characteristic of our calculation of hadronic current correlators at finite temperature and finite density in the deconfined phase is the appearance of complex resonance structure in some cases. That feature is in general agreement with the observation made in Ref. (5) "...that the correlators possess a nontrivial structure in the deconfined phase." Meson correlators were studied in finite temperature lattice QCD in Ref. (41), in which the authors state, "...Below T_c we observe little change in the meson properties as compared with $T = 0$. Above T_c we observe new features: chiral symmetry restoration and signals of plasma formation, but also an indication of persisting "mesonic" (metastable) states and different temporal and spacial masses in the mesonic channels. This suggests a complex picture of QGP in the region (1-1.5)T_c".

Chapter 4

Quark Propagation in Dense Matter

4.1 Quark and Nucleon Self-Energy in Dense Matter

4.1.1 Introduction

As is well known, the NJL model provides a microscopic dynamical description of chiral symmetry breaking with the generation of associated quark vacuum condensates and constituent masses. In the standard versions of the NJL model (8; 9; 11), the constituent quark mass that is generated in the model is a constant. However, it is known from lattice simulations of QCD that the constituent mass goes over to the current quark mass when the quark momentum, p^2, is less than about -2 GeV^2 (42). It is our belief that, if we are to use the NJL model to study dense matter, it is desirable to make the model as realistic as possible. To that end, we have introduced a nonlocal version of the NJL model (13) that is able to reproduce the Euclidean-space behavior of the quark mass seen in lattice simulations of QCD (42). To carry out that program we have introduced a momentum-dependent $q\bar{q}$ interaction in the calculation of the quark self-energy and have separated the regularization of the model from the specification of that interaction. (This procedure requires the introduction of additional parameters into the model.)

We note that the quark self-energy may be written as

$$\Sigma^{vac}(k^2) = A^{vac}(k^2) + B^{vac}(k^2)\not{k} \tag{4.1}$$

in vacuum. In matter there is another four-vector, η^μ, that describes the motion of the matter rest frame. It is useful to put $\eta^2 = 1$ and to note that, if we work in the matter rest frame, we can put $\eta^\mu = [1, 0, 0, 0]$. We define the self-energy in matter to be

$$\Sigma(k^2, \eta \cdot k) = A(k^2, \eta \cdot k) + B(k^2, \eta \cdot k)\bar{\not{k}} + C(k^2, \eta \cdot k)\not{\eta}\,, \tag{4.2}$$

where we have found it useful to introduce the four-vector

$$\bar{k}^\mu = k^\mu - (k \cdot \eta)\eta^\mu\,. \tag{4.3}$$

Note that $\bar{k}^0 = 0$ in the matter rest frame. In that frame, we may write

$$\Sigma(k^0, \vec{k}) = A(k^0, \vec{k}) - B(k^0, \vec{k})\vec{\gamma} \cdot \vec{k} + \gamma^0 C(k^0, \vec{k})\,. \tag{4.4}$$

As we will see, A and B satisfy coupled nonlinear equations, while C may be calculated independently. (Note that A and C have the same dimension, while B is dimensionless.)

We discuss our results for the case in which we neglect the dependence of A, B, and C on k^0. (We have found that the dependence on k^0 is weak for the model introduced in this work.) As a further simplification, we will at first neglect B and study the behavior of $A(\vec{k}, \rho)$, where ρ is the density of quark matter which is taken to contain equal numbers of up and down quarks. In this case, the maximum value of $A(\vec{k},\rho)$ is found at $\vec{k}=0$, leading to a simpler presentation of our results. We then go on to the consideration of the coupled equations for $A(\vec{k},\rho)$ and $B(\vec{k},\rho)$. As usual, we may introduce a density and momentum-dependent mass defined by

$$M(\vec{k},\rho)=\frac{A(\vec{k},\rho)}{1-B(\vec{k},\rho)}\,. \tag{4.5}$$

We provide values of $A(\vec{k},\rho)$, $M(\vec{k},\rho)$ and $C(\vec{k},\rho)$ in the following sections.

We note that the inclusion of $C(\vec{k},\rho)$ precludes the passage to Euclidean space. That is analogous to the corresponding problem which arises when one introduces a finite chemical potential. As we will see, $C(\vec{k},\rho)$ is quite large finite density and can only be neglected at very small densities. We note that our formalism does not maintain Lorentz invariance. (For example, our regulator depends only upon $|\vec{k}|$.) Therefore, in the following we will only calculate the contribution to $C(\vec{k},\rho)$ from the matter, which takes the form of two Fermi seas of up and down positive-energy quarks with Fermi momentum k_F.

In Ref. (13) we made use of a nonlocal version of the NJL model. We may describe the procedure we use to create the nonlocal model. We begin by writing the Lagrangian.

$$\mathcal{L}= \qquad \bar{q}(i\partial\!\!\!/-m^0)q+\frac{G_S}{2}\sum_{i=0}^{8}[(\bar{q}\lambda^i q)^2+(\bar{q}i\gamma_5\lambda^i q)^2]\,. \tag{4.6}$$

Here, the $\lambda^i\,(i=1,\cdots,8)$ are the Gell-Mann matrices and $\lambda^0=\sqrt{2/3}\,\mathbf{1}$, with $\mathbf{1}$ being the unit matrix in the flavor space. It is then useful to consider an expression involving the interaction of two currents. We replace the second term of Eq. (4.6) by a nonlocal form

$$\begin{aligned}\frac{G_S}{2}j^\mu(x)\Gamma(x,y)j_\mu(y) &= \frac{G_S}{2}\sum_{i=0}^{8}\bar{q}(x)\lambda^i\gamma^\mu f(x)q(x)\bar{q}(y)\lambda^i\gamma^\mu f(y)q(y) \quad (4.7)\\ &= \frac{G_S}{2}\sum_{i=0}^{8}\{[\bar{q}(x)\lambda^i f(x)q(y)\bar{q}(y)\lambda^i f(y)q(x)] \quad (4.8)\\ &\quad + [\bar{q}(x)\lambda^i i\gamma_5 f(x)q(y)\bar{q}(y)\lambda^i i\gamma_5 f(y)q(x)]\}\\ &\quad +\cdots\,,\end{aligned}$$

where we have used a separable form for $\Gamma(x,y) = f(x)f(y)$ and have performed a Fierz rearrangement to pass from Eq. (4.7) to Eq. (4.8). We have not written the vector and axial-vector interactions that arise in the Fierz transformation. (See Appendix B of Ref. (11).)

It is useful to describe the modifications induced by the nonlocality of the interaction when performing momentum-space calculations. In such calculations we find that we need to replace G_S by $f(k_2-k_3)G_S f(k_1-k_4)$ where k_1 and k_2 are the quark momenta entering the interaction region and k_3 and k_4 are the momenta leaving the interaction. For the calculations reported here, $k_1 = k_2 = k$ and $k_3 = k_4 = k'$, so that the replacement is $G_S(k-k') = f(k-k')G_S f(k-k')$. In this work we take $f(k) = \exp[-(k-k')^{2n}/2\beta^8]$ with $n = 4$ and $\beta = 20$ GeV.

We now consider the more general nonlocal Lagrangian which includes vector and axial-vector interactions

$$\begin{aligned}\mathcal{L} = \quad & \bar{q}(i\partial\!\!\!/ - m^0)q + \frac{G_S}{2}\sum_{i=0}^{8}\{[\bar{q}(x)\lambda^i f(x)q(y)\bar{q}(y)\lambda^i f(y)q(x)] \\ & \qquad\qquad + [\bar{q}(x)\lambda^i i\gamma_5 f(x)q(y)\bar{q}(y)\lambda^i i\gamma_5 f(y)q(x)]\} \\ & -\frac{G_V}{2}\sum_{i=0}^{8}\{[\bar{q}(x)\lambda^i\gamma_\mu f(x)q(y)\bar{q}(y)\lambda^i\gamma^\mu f(y)q(x)] \\ & \qquad\qquad + [\bar{q}(x)\lambda^i\gamma_\mu\gamma_5 f(x)q(y)\bar{q}(y)\lambda^i\gamma^\mu\gamma_5 f(y)q(x)]\}\end{aligned} \tag{4.9}$$

Here G_S and G_V are independent parameters. The term proportional to G_V is important in the study of the ω, ρ, a_1 and ϕ mesons , for example. In our work we have studied the properties of these mesons and their radial excitations in the local version of the Lagrangian (18). The Lagrangian of Eq. (4.9) was used in Ref. (13) with $G_V = 0$. We also included the 't Hooft interaction and our model of confinement. In Ref. (13) both the condensate values and self-energies were given for the up (down) and strange quarks. For the present work we neglect the 't Hooft interaction and our model of confinement. Here, we also drop the strange quark from consideration, so that the quark current mass matrix is $m^0 = diag(m_u^0, m_d^0)$ with $m_u^0 = m_d^0$. Since the 't Hooft interaction contributes to the self-energy (13), its neglect leads us to use larger values of G_S than we would use if the 't Hooft interaction were included in our analysis.

4.1.2 The Quark Self-Energy

In our earlier work we obtained the quark self-energy from the solution of the equation depicted in Fig. 4.1 (13). There, the open circle is a momentum-

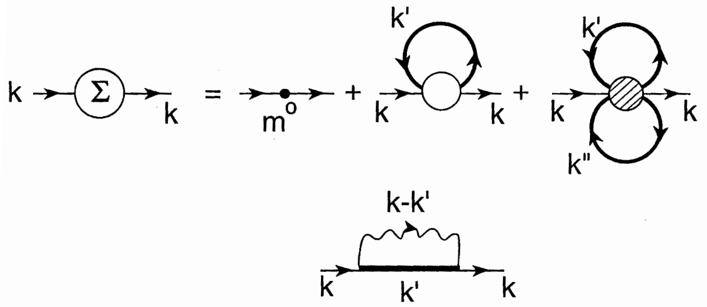

Figure 4.1: The equation for the quark self-energy that was solved in Euclidean space in Ref. (13) is shown. Here, m^0 is the current quark mass. The open circle represents the momentum-dependent $q\bar{q}$ interaction in the nonlocal model. The third term on the right-hand side of the figure represents the 't Hooft interaction and the fourth term arises from our model of confinement. The heavy lines are quark propagators which include the self-energy, $\Sigma(k)$, in their definition.

dependent quark interaction. The corresponding nonlocal Lagrangian is given in Ref. (13). On the right-hand side of Fig. 4.1, the 't Hooft interaction (third term) and the confinement interaction (fourth term) are neglected for the purposes of this work. In the second term we have contributions from the negative-energy states in vacuum as well as the positive-energy states at finite density, specified by the quark Fermi momentum, k_F, of the up and down quark Fermi seas.

In general, the quark propagator is

$$iS(k^2, k\cdot\eta) = \frac{i}{\not{k} - \Sigma(k^2, k\cdot\eta) + i\epsilon}\,, \tag{4.10}$$

which we will write as

$$iS(k^0,\vec{k}) = \frac{i}{(k^0 - C(k^0,\vec{k}))\gamma^0 - (1 - B(k^0,\vec{k}))\vec{\gamma}\cdot\vec{k} - A(k^0,\vec{k}) + i\epsilon}\,, \tag{4.11}$$

in the matter rest frame. In the following we will neglect the k^0 dependence of the quantities in Eq. (4.13). Further, $A(\vec{k})$, $B(\vec{k})$ and $C(\vec{k})$ are density-dependent, in general. (On occasion we will write $A(\vec{k},\rho)$, etc.) Note that

$$\begin{aligned}(k^0 - C(\vec{k}))^2 - (1 - B(\vec{k}))^2\vec{k}^2 - A^2(\vec{k}) + i\epsilon \\ = [k^0 - E^+(\vec{k}) + i\epsilon][k^0 - E^-(\vec{k}) - i\epsilon]\end{aligned} \tag{4.12}$$

with

$$E^{\pm}(\vec{k}) = C(\vec{k}) \pm \sqrt{\vec{k}^2(1 - B(\vec{k}))^2 + A^2(\vec{k}^2)}\,. \tag{4.13}$$

Here $E^+(\vec{k})$ may be interpreted as the (on-mass-shell) energy of the positive-energy states, while $E^-(\vec{k})$ refers to the negative-energy states. These quantities appear in the representation of the propagator given in Eq. (4.24).

In order to simplify the notation somewhat, we write

$$iS(k^0,\vec{k}) = \frac{i}{\not{\Pi}(k^0,\vec{k}) - A(\vec{k}) + i\epsilon}\,, \tag{4.14}$$

where we have defined a four-component quantity

$$\Pi^\mu(k^0,\vec{k}) = [k^0 - C(\vec{k}), (1 - B(\vec{k}))\vec{k}]\,. \tag{4.15}$$

In vacuum, we find

$$A(\vec{k}) = m^0 - 2G_S\rho_S(\vec{k})\,, \tag{4.16}$$

where $\rho_S(\vec{k})$ is real and negative scalar quantity,

$$\rho_S(\vec{k}) = iN_C(-1)\int\frac{d^4k'}{(2\pi)^4}\,\frac{4A(\vec{k}')f^2(k-k')}{\Pi^2(k'^0,\vec{k}') - A^2(\vec{k}') + i\epsilon}\,. \tag{4.17}$$

Here, $N_c = 3$ is the number of colors. The minus sign in the last equation is due to the closed Fermion loop in Fig. 4.1 and the factor of 4 comes from forming the trace associated with the closed loop. We see that $\rho_S(\vec{k})$ does not depend upon k^0, since we are making an on-shell approximation in the calculation of $f(k-k')$.

If we put $f(k-k') = 1$, $\rho_S(\vec{k}) \to \langle\bar{u}u\rangle$ with

$$\langle\bar{u}u\rangle = iN_C(-1)\int\frac{d^4k'}{(2\pi)^4}\,\frac{4A(\vec{k}')}{\Pi^2(k'^0,\vec{k}') - A^2(\vec{k}') + i\epsilon} \tag{4.18}$$

being the up quark vacuum condensate.

When we take $f(k-k') = 1$, we have $A(\vec{k}) = m$ and thus regain the equations of the local version of the NJL model (8; 9; 11). In that case we have

$$m_u = m_u^0 - 2G_S\langle\bar{u}u\rangle\,, \tag{4.19}$$

and an analogous equation for the d quark. (Note that our G_S is one-half of the G_S defined in Ref. (9).)

The evaluation of $\rho_S(\vec{k})$ or the quark condensate proceeds by closing to contour in the complex k^0 plane. In the vacuum we find

$$\rho_S(\vec{k}) = -2N_C\int\frac{d^3k'}{(2\pi)^3}\,\frac{f^2(k-k')A(\vec{k}')}{\sqrt{\vec{k}'^2(1-B(\vec{k}'))^2 + A^2(\vec{k}')}}\,. \tag{4.20}$$

We define

$$E(\vec{k}) = \sqrt{\vec{k}^2(1-B(\vec{k}))^2 + A^2(\vec{k})}\,, \tag{4.21}$$

and

$$(k-k')^2 = (E(\vec{k}) - E(\vec{k}'))^2 - (\vec{k}-\vec{k}')^2\,, \tag{4.22}$$

so that $f(k-k')$ depends only upon $|\vec{k}|$, $|\vec{k}'|$ and the angle between $\vec{k}$ and $\vec{k}'$.

Integrals such as that in Eq. (4.20) require regularization. For our calculations we insert a factor $\exp[-\vec{k}'^2/\alpha^2]$ with $\alpha = 0.60$ GeV. (We have used the same Gaussian regulator in our calculations of meson spectra, where we have used $\alpha = 0.605$ GeV (43; 44; 45). However, these calculations included a model of confinement, so that we can not directly take over the parameters G_S, G_V and G_D used in those works. Note that the value of $\alpha = 0.60$ GeV for the Gaussian regular yields results that are similar to those obtained when the three-dimensional cutoff, $|\vec{k}| \leq \Lambda_3$, with $\Lambda_3 \simeq 0.62$ GeV, is used. We have found that the use of the Gaussian regulator yields more satisfactory results when calculating radial excitations of various light mesons.) We remark that an expression for the condensate $\langle \bar{u}u \rangle$ may be obtained by using Eq. (4.20) with $f(k-k') = 1$.

In the presence of matter it is useful to separate the propagator into two parts, one of which will give rise to the explicitly density-dependent terms. In this regard, it is useful to generalize Eq. (5.8) of Ref. (11) so that we can treat the self-energy given in Eq. (4.4). We define

$$\Lambda^{(\pm)}(\pm\vec{k}) = \frac{\pm E(\vec{k})\gamma^0 - \vec{\gamma}\cdot\vec{k}(1-B(\vec{k})) + A(\vec{k})}{2A(\vec{k})}\,, \tag{4.23}$$

where $E(\vec{k}) = [\vec{k}^2(1-B(\vec{k}))^2 + A^2(\vec{k})]^{1/2}$. Then

$$\begin{aligned} S(k) = \quad & \frac{A(\vec{k})}{E(\vec{k})}\left[\frac{\Lambda^{(+)}(\vec{k})}{k^0 - E^{+}(\vec{k})} - \frac{\Lambda^{(-)}(-\vec{k})}{k^0 - E^{-}(\vec{k})}\right] \qquad (4.24) \\ + \quad & 2\pi i \frac{A(\vec{k})}{E(\vec{k})}\Lambda^{(+)}(\vec{k})\,\theta(k_F - |\vec{k}|)\,\delta(k^0 - E^{+}(\vec{k})) \end{aligned}$$

In the limit that $A(\vec{k}) \to m^*$ and $B(\vec{k}) = C(\vec{k}) = 0$, we have, with $E^*(\vec{k}) = \sqrt{\vec{k}^2 + m^{*2}}$,

$$\begin{aligned} S(k) &= \frac{m^*}{E^*(\vec{k})}\left[\frac{\Lambda^{(+)}(\vec{k})}{k^0 - E^*(\vec{k})} - \frac{\Lambda^{(-)}(-\vec{k})}{k^0 + E^*(\vec{k})}\right] \qquad (4.25) \\ &+ 2\pi i \frac{m^*}{E^*(\vec{k})}\Lambda^{(+)}(\vec{k})\,\theta(k_F - |\vec{k}|)\,\delta(k^0 - E^*(\vec{k})) \\ &= \frac{\not{k} + m^*}{k^2 - m^{*2}} + \frac{i\pi}{E^*(\vec{k})}(\not{k} + m^*)\,\theta(k_F - |\vec{k}|)\,\delta(k^0 - E^*(\vec{k}))\,, \qquad (4.26) \end{aligned}$$

which agrees with Eq. (5.8) of Ref. (11).

In the presence of matter, we have

$$A(\vec{k}, \rho) = m^0 - 2G_S[\rho_S^{vac}(\vec{k}) - \rho_S^{mat}(\vec{k})]\,, \qquad (4.27)$$

where $\rho_S^{mat}(\vec{k})$ is calculated in the same manner as $\rho_S^{vac}(\vec{k})$, except that the upper limit of the integral over $|\vec{k}'|$ is k_F,

$$\rho_S^{mat}(\vec{k}) = -2N_C \int_0^{k_F} \frac{d^3k'}{(2\pi)^3} \frac{A(\vec{k}')}{\sqrt{\vec{k}'^2(1 - B(\vec{k}'))^2 + A^2(\vec{k}')}}\,. \qquad (4.28)$$

Equation (4.24) is a generalization of a corresponding equation that may be found in Klevansky's review. (See Eqs. (5.18) of Ref. (11).)

If we neglect $B(\vec{k})$, Eqs. (4.17) and (4.20) provide a nonlinear equation for $A(\vec{k})$ which may be solved by iteration. The results of such a calculation are reported in Table 4.1 where, for nuclear matter, we put $k_F = 0.268$ GeV. In Fig. 4.2 and 4.3 we show that values of the condensate $\langle \bar{u}u \rangle$ and $A(0,\rho)$ as a function of the density. These results may be usefully discussed in terms of the relation (46)

$$\langle \bar{u}u \rangle_\rho = \langle \bar{u}u \rangle_0 \left(1 - \frac{\sigma_N \rho_N}{f_\pi^2 m_\pi^2} + \cdots \right) . \tag{4.29}$$

Here σ_N is the pion-nucleon sigma term and ρ_N is the density of nucleons. If we put $\sigma_N = 0.050$ GeV, $\rho_N = (0.109\,\mathrm{GeV})^3$, $f_\pi = 0.0942$ GeV and $m_\pi = 0.138$ GeV, we find a 38% reduction of the condensate at nuclear matter density, which agrees with our results given in Table 4.1 and Fig. 4.2. It is of interest to note that the linear dependence on the density implied by Eq. (4.29) appears to be valid up to about twice nuclear matter density. However, one may be concerned that, since we study quark matter rather than nuclear matter, Eq. (4.29) may not be appropriate. Consider, however, the relation

$$\langle \bar{u}u \rangle_\rho = \langle \bar{u}u \rangle_0 \left(1 - \frac{\sigma_q \rho_q}{f_\pi^2 m_\pi^2} + \cdots \right) , \tag{4.30}$$

where σ_q is the quark sigma term and ρ_q is the number density of the quarks, which we may put equal to $3\rho_N$. Thus, if $3\sigma_q = \sigma_N$, we may use Eq. (4.29). The fact that $\sigma_q \simeq 15$ MeV has been discussed by Vogl and Weise (9). We have also discussed this matter in great detail in Ref. (46), where we calculate similar values of σ_q using the standard version of the NJL model. We conclude that the use of Eq. (4.29), or Eq. (4.30), with an appropriate value of σ_q, is satisfactory.

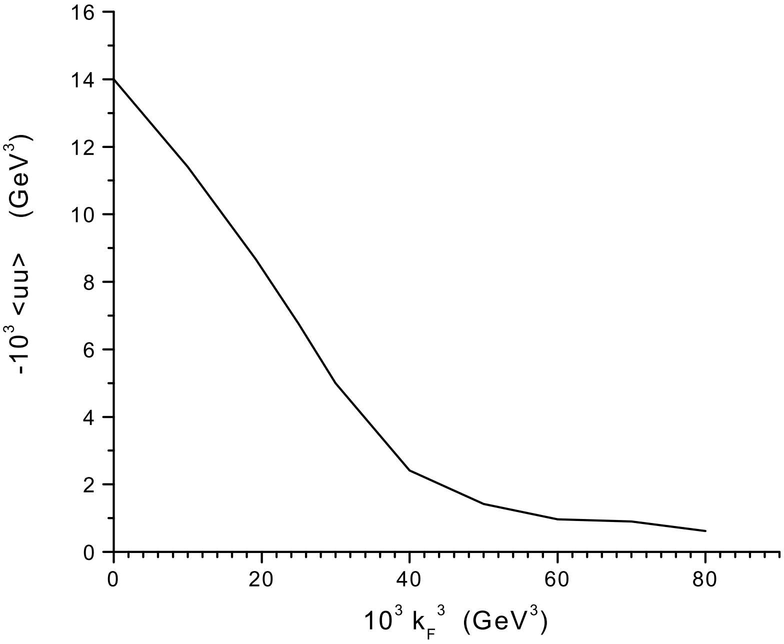

Figure 4.2: Values of the condensate $\langle \bar{u}u \rangle$ are given as a function of $10^3 k_F^3$. For nuclear matter $10^3 k_F^3 = 19.2$ GeV^3. [See Table 4.1.] Here $G_S = 13.0$ GeV^{-2} and $B(\vec{k}, \rho)$ is put equal to zero.

For example, if $\sigma_q = \sigma_N/3$, as suggested in Ref. (9), the two relations imply the same density dependence of the condensate.

In Fig. 4.3 we show $A(0, \rho)$ which is the density-dependent mass parameter of the theory when $B(\vec{k}, \rho) = 0$. We see that $A(0, \rho)$ follows the trend seen in Fig. 4.2 for the density dependence of the condensate.

$10^3 k_F^3$ (GeV^3)	$\langle \bar{u}u \rangle$ (GeV^3)	$A(0,\rho)$ (GeV)
0	$(-0.241)^3$	0.371
10	$(-0.225)^3$	0.298
19.2(nm)	$(-0.205)^3$	0.226
25	$(-0.189)^3$	0.177
30	$(-0.171)^3$	0.133
40	$(-0.134)^3$	0.077
50	$(-0.113)^3$	0.041
60	$(-0.0990)^3$	0.030
70	$(-0.0915)^3$	0.024
80	$(-0.0853)^3$	0.021
90	$(-0.0805)^3$	0.018

Table 4.1: Values of the condensate and $A(0,\rho)$ are given for $G_S = G_V = 13.0$ GeV^{-2} and $m_u^0 = m_d^0 = 0.005$ GeV. We note the reduction of the condensate of 38% and a 40% reduction of $A(0,\rho)$ at nuclear matter density [$10^3 k_F^3 = 19.2$ GeV^3]. Here $\alpha = 0.60$ GeV is used in the Gaussian regulator $\exp[-\vec{k}^2/\alpha^2]$.

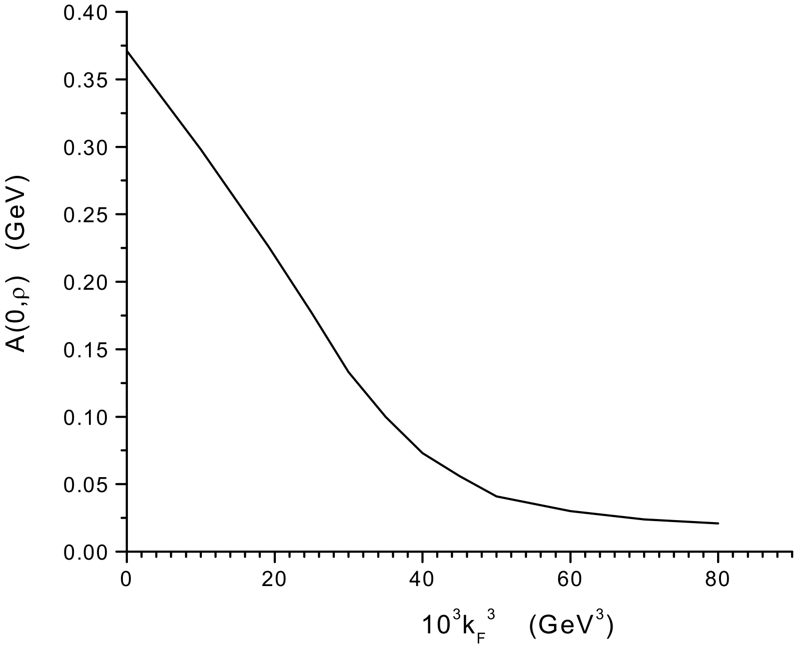

Figure 4.3: Values of $A(0,\rho)$ are given as a function of $10^3 k_F^3$. [See Table 4.1 and the caption to Fig. 4.2.]

4.1.3 Lorentz-Vector Terms of the Quark Self-Energy

We now write $\Sigma(\vec{k}) = \Sigma_S(\vec{k}) + \Sigma_V(\vec{k})$ where

$$\Sigma_V(\vec{k}) = -\vec{\gamma}\cdot\vec{k}B(\vec{k}) + \gamma^0 C(\vec{k})\,. \tag{4.31}$$

For the calculation of $C(\vec{k})$ we obtain the contribution from the last term in Eq. (4.27), with the result that

$$C(\vec{k}) = 2G_V\rho_2^V(\vec{k}) \tag{4.32}$$

with

$$\rho_2^V(\vec{k}) = 2N_C \int^{k_F} \frac{d^3k\,'}{(2\pi)^3}\, f^{\,2}(k-k\,')\,. \tag{4.33}$$

If we compare Eq. (4.33) to Eq. (4.22) for $\rho_S(\vec{k})$, we see that the Dirac matrix γ_0 that appears in the quark loop in the calculation of $\rho_2^V(\vec{k})$ has the effect of removing the factor $A(\vec{k}\,')/[\vec{k}\,'^2(1-B(\vec{k}\,'^2))^2+A^2(\vec{k}\,')]^{1/2}$ from under the integral. In the local NJL model that factor is just $m/E(\vec{k}\,')$, whose appearance is characteristic of the evaluation of a scalar quantity.

An expression for $B(\vec{k})$ may be found from the relation

$$-\,i[-\vec{\gamma}\cdot\vec{k}B(\vec{k})] = (-2G_V i)(-1)i\int \frac{d^4k\,'}{(2\pi)^4}\, S(k\,')f^{\,2}(k-k\,') \tag{4.34}$$

if we only keep the term proportional to $\vec{\gamma}\cdot\vec{k}'$ in the expression for the quark propagator. In vacuum we may compare corresponding terms in Eq. (4.34)

$$-\,\vec{\gamma}\cdot\vec{k}B(\vec{k}) = -2G_V\int\frac{d^4k'}{(2\pi)^4}\,\frac{-\vec{\gamma}\cdot\vec{k}'[1-B(\vec{k}')]}{[k_0'-E^+(\vec{k}')+i\epsilon][k_0'+E^-(\vec{k}')-i\epsilon]}\,. \tag{4.35}$$

Thus,

$$B^{vac}(\vec{k}) = 2G_V\rho_1^{vac}(\vec{k})\,, \tag{4.36}$$

with

$$|\vec{k}|\rho_1^{vac}(\vec{k}) = 2N_C\int\frac{d^3k\,'}{(2\pi)^3}\,\frac{|\vec{k}'|(\hat{k}\cdot\hat{k}\,')f^{\,2}(k-k\,')[1-B(\vec{k}')]}{\sqrt{\vec{k}\,'^2[1-B(\vec{k}')]^2+A^2(\vec{k}')}}\,. \tag{4.37}$$

Here, $\hat{k}$ and $\hat{k}\,'$ are unit vectors. As in the calculation of $A(\vec{k})$, Eq. (4.36) is generalized to read

$$B(\vec{k}) = 2G_V[\rho_1^{vac}(\vec{k})-\rho_1^{mat}(\vec{k})]\,, \tag{4.38}$$

where $\rho_1^{mat}(\vec{k})$ is calculated using Eq. (4.37) with an upper limit on $|\vec{k}'|$ of k_F.

In Table 4.2 we present results of our calculation of the condensate $A(0,\rho)$, $A(0,\rho)/[1-B(0,\rho)]$, $C(0,\rho)$, $B(0,\rho)$ and $A(0,\rho)-A(0,0)$. We also define

$$U_S(\vec{k},\rho) = A(\vec{k},\rho) - A(\vec{k},0)\,, \tag{4.39}$$

where $U_S(\vec{k},\rho)$ is the density-dependent modification of $A(\vec{k},0)$ in matter.

It may be seen from the values given in Table 4.2 that there is a thirty percent reduction of the condensate at the density of nuclear matter, while the value of $A(0)$ is reduced by thirty-nine percent. We would obtain a thirty percent reduction of the condensate if we put $\sigma_N = 39$ MeV in Eq. (4.29).

In Fig. 4.4 and 4.5 we exhibit values of $A(\vec{k},\rho)$ and $A(\vec{k},\rho)/[1-B(\vec{k},\rho)]$ for various densities and in Fig. 4.6 we present values of $C(\vec{k},\rho)$. Figure 4.7 shows the values of $U_S(\vec{k},\rho_{NM})$ and $C(\vec{k},\rho_{NM})$.

4.1.4 The Nucleon Self-Energy in Matter

If one uses the Dirac equation to describe the interaction of a nucleon with a nucleon, or with nuclear matter, it is found that a strong scalar attraction is needed as well as a strong vector repulsion (47; 48). The scalar field is of the order of -400 MeV and the vector field is about 300 MeV. It is of interest to see if the nucleon self-energy, $\Sigma_N = V_S + \gamma^0 V_V$, can be calculated in terms of the quark self-energy obtained in this work. To carry out this program we use a simple model of the nucleon in which a quark is coupled to a scalar diquark.

$10^3 k_F^3$ (GeV^3)	$\langle\bar{u}u\rangle$ (GeV^3)	$A(0,\rho)$ (GeV)	$\frac{A(0,\rho)}{1-B(0,\rho)}$ (GeV)	$U_S(0,\rho)$ (GeV)	$C(0,\rho)$ (GeV)	$B(0,\rho)$
0	$(-0.2401)^3$	0.365	0.347	0	0	-0.0544
10	$(-0.2279)^3$	0.292	0.272	-0.073	0.0794	-0.0736
19.2	$(-0.2128)^3$	0.223	0.203	-0.142	0.0988	-0.1019
30	$(-0.1755)^3$	0.114	0.0942	-0.252	0.115	-0.210
40	$(-0.1441)^3$	0.0606	0.0435	-0.304	0.126	-0.394
50	$(-0.1291)^3$	0.0432	0.0279	-0.322	0.136	-0.545

Table 4.2: Various values are given for the case $G_S = 13.5$ GeV^{-2}, $G_V = 10.0$ GeV^{-2}, $m_u^0 = m_d^0 = 0.005$ GeV and $\alpha = 0.60$ GeV. Note a reduction of 27% for the condensate and 35% for $A(0,\rho)$ at nuclear matter density.

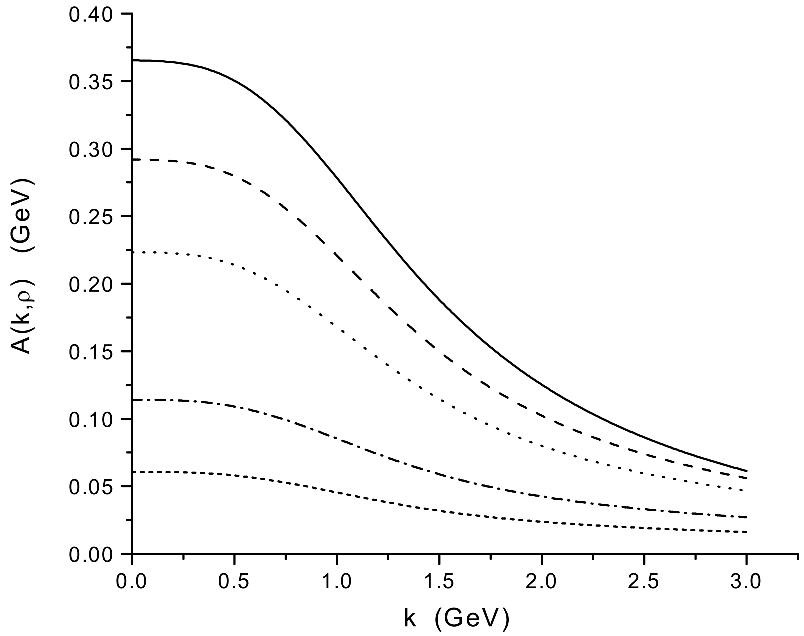

Figure 4.4: Values of $A(\vec{k},\rho)$ are given as a function of $|\vec{k}|$ for various densities: $10^3 k_F^3 = 0$ [solid line], 10.0 GeV^3 [dashed line], 19.2 GeV^3 [dotted line], 30.0 GeV^3 [dot-dash line] and 40.0 GeV^3 [short dash]. Here $G_S = 13.5$ GeV^{-2}, $G_V = 10.0$ GeV^{-2}, $m^0 = 0.005$ GeV and $\alpha = 0.60$ GeV. [See Table 4.2.]

The full complexity of the wave function, including vector diquarks, and various relativistic effects is discussed in Ref. (49).

We can calculate the nucleon self-energy in nuclear matter using a triangle diagram in which one of the lower two vertices of the triangle represents a vertex function for a zero-momentum nucleon to emit a quark of momentum $\vec{k}$ leaving a spectator (on-mass-shell) diquark of momentum $-\vec{k}$. The other lower vertex represents the inverse process. At the upper vertex we insert the quark self-energy,

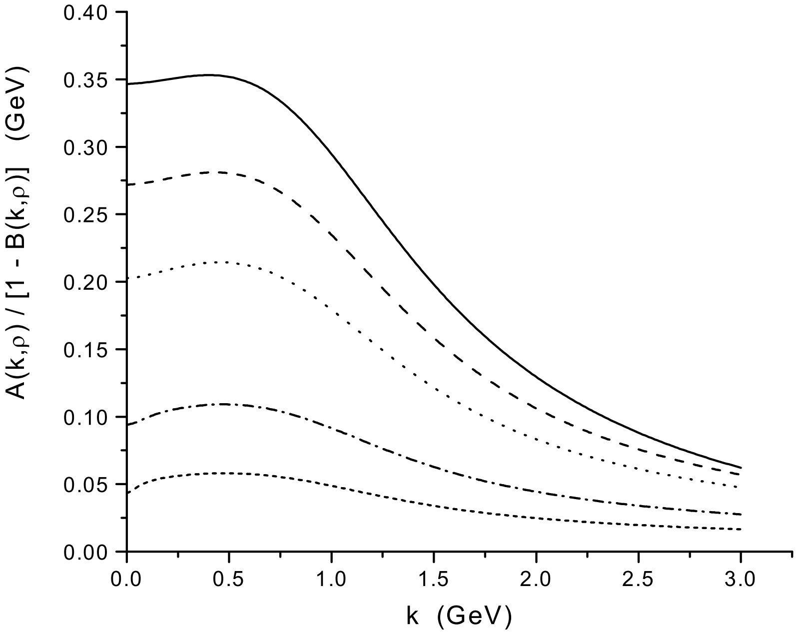

Figure 4.5: The quantity $M(\vec{k}, \rho) = A(\vec{k}, \rho)/[1 - B(\vec{k}, \rho)]$, which plays the role of a momentum- and density-dependent mass parameter, is shown. [See Table 4.2 and the caption of Fig. 4.4.]

$\Sigma(\vec{k}) = U_S(\vec{k}) + \gamma^0 C(\vec{k})$ calculated in this work and integrate over $\vec{k}$. We make use of Fig. 4.4 of Ref. (49) and parametrize the product of the vertex function and the quark Greens function by the quark-diquark wave function

$$\psi(\vec{k}) = \frac{1}{\sqrt{N}}\, e^{-k^2/\lambda^2} u(\vec{k}, s)\,, \tag{4.40}$$

where $u(\vec{k}, s)$ is a spinor for a quark of momentum $\vec{k}$ and spin projection s (49).

The normalization for a single quark is obtained from the relation

$$\frac{1}{N}\int \frac{d^3k}{(2\pi)^3}\, e^{-2\vec{k}^2/\lambda^2} \left(1 + \frac{\vec{k}^2}{[E_q(\vec{k}) + m_q]^2}\right) = 1\,, \tag{4.41}$$

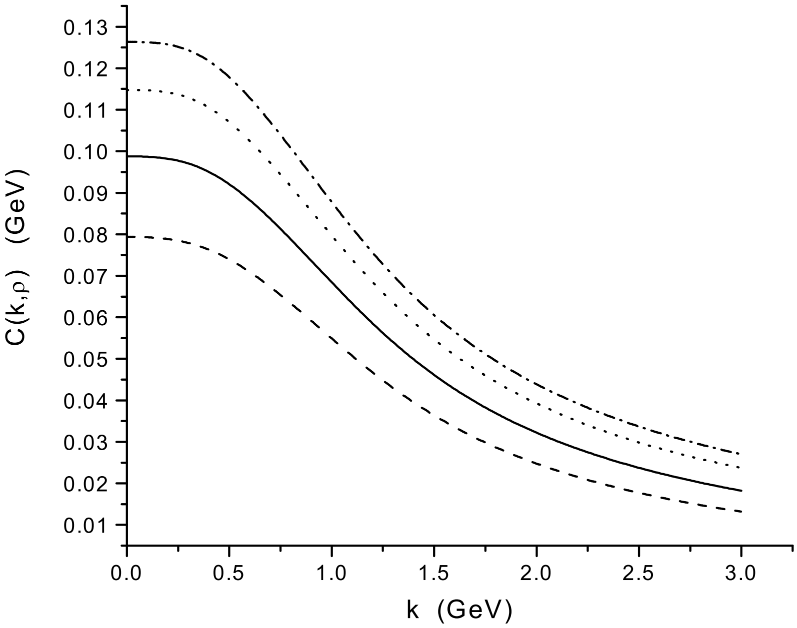

Figure 4.6: Values of $C(\vec{k},\rho)$ are shown for various densities: $10^3 k_F^3 = 10.0$, 19.2, 30 and 40 GeV^3. [See the caption for Fig. 4.4.] Here $G_S = 13.5$ GeV^{-2}, $G_V = 10.0$ GeV^{-2}, $m^0 = 0.005$ GeV and $\alpha = 0.60$ GeV.

where we put $\lambda = 0.18$ GeV to correspond to the results of Ref. (49). We may then relate the nucleon self-energy to the quark self-energy. For a nucleon of momentum $\vec{p} = 0$, we have, with $E_q(\vec{k}) = [\vec{k}^2 + m_q^2]^{1/2}$, and $m_q = 0.364$ GeV,

$$V_V = \frac{3}{N}\int \frac{d^3k}{(2\pi)^3}\, C(\vec{k})\, e^{-2\vec{k}^2/\lambda^2} \left(1 + \frac{\vec{k}^2}{[E_q(\vec{k}) + m_q]^2}\right), \tag{4.42}$$

and

$$V_S = \frac{3}{N}\int \frac{d^3k}{(2\pi)^3}\, U_S(\vec{k})\, e^{-2\vec{k}^2/\lambda^2} \left(1 - \frac{\vec{k}^2}{[E_q(\vec{k}) + m_q]^2}\right). \tag{4.43}$$

The difference of sign in the bracket appearing in Eqs. (4.42) and (4.43) is due

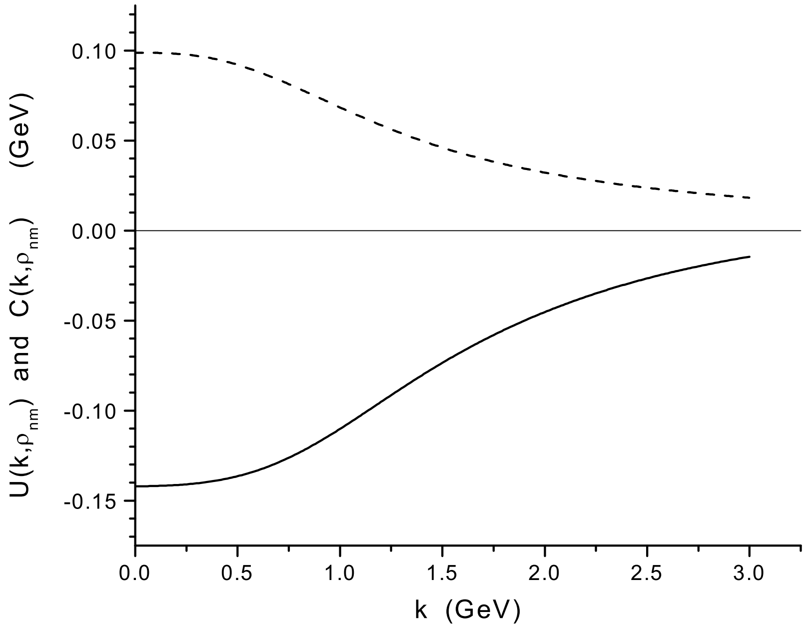

Figure 4.7: The values of $U(k,\rho_{NM}) = A(k,\rho_{NM}) - A(k,0)$ [solid line] and $C(k,\rho_{NM})$ [dashed line] are shown. $U(k,\rho_{NM})$ represents the density-dependent correction to the vacuum value of the scalar term of the quark self-energy.

to the different behavior of the Dirac matrices, $\mathbf{1}$ and γ^0, at the upper vertex of the triangle.

Since the momentum content of the quark-diquark wave function is small (48), we expect that $V_V \simeq 3U_S(0)$ and $U_S \simeq 3C(0)$, so that $V_V \simeq 296$ MeV and $V_S \simeq -426$ MeV. A more careful evaluation of the integrals in Eqs. (4.42) and (4.43) yields $V_V = 295$ MeV and $V_S = 392$ MeV which is in general accord with the values given in Refs. (47) and (48).

4.1.5 Discussion

In the present study we have considered the important vector interactions of extended NJL model. Of particular interest is the behavior of the quark condensate at finite density. We find that the linear behavior in the density exhibited in Eq. (4.29) holds in our model up to about twice nuclear matter density. Also, we note that the use of a nonzero current quark mass is important for that result, since in the absence of an explicitly chiral symmetry breaking term, the model exhibits a first-order phase transition at a density slightly below that of a nuclear matter (50).

Another point of interest are the results shown in Fig. 4.7. The quark self-energy is similar to that found in relativistic nuclear physics, with strong scalar attraction and strong vector repulsion. The simple calculation reported in Section IV suggests that the quark self-energy, when multiplied by 3, provides a satisfactory estimate of the nucleon self-energy that is in accord with results of relativistic nuclear physics (47; 48). The modification of the picture given here is presented in the next section and is more consistent with recent experimental results.

4.2 Quark Propagation in the Quark-Gluon Plasma

4.2.1 Introduction

The description of the quark-gluon plasma in terms of hydrodynamics has been advocated by the Stony Brook group (51; 52; 53). That description appears to be in accord with the experimental data. In such a description the motion of the quarks is characterized by an extremely short mean-free-path. The origin of that behavior is thought to be due to the relatively low-energy resonances in the $q\bar{q}$ system leading to very large scattering lengths. These resonances have been found in lattice studies of QCD which make use of the maximum entropy method (MEM) (1; 2; 3; 4; 5; 6). Similar resonances are found in the scalar, pseudoscalar, vector and axial-vector $q\bar{q}$ channels (54). Recently, an extensive exploration of charmonium studies in the confined and deconfined regions using lattice methods has been reported in Ref. (20). In that work results are given for the dependence of the resonance excitation on the total momentum of the $q\bar{q}$ pair. We have studied that dependence for light quark systems in Ref. (21) and have found similar behavior to that reported in Ref. (20). (We will make use of the results presented in Ref. (21) in the present work in which we calculate the imaginary part of the optical potential and the mean-free-path for a quark in the quark-gluon plasma.) We use a chiral model with rather large momentum cutoff. That model is meant to provide an approximate description of the instanton dynamics advocated by the Stony Brook group (51; 52; 53).

In the study of hadronic current correlators it is important to use a model which respects chiral symmetry when $m^0 = 0$. Therefore, we make use of the Lagrangian of Eq. (2.3), while neglecting the 't Hooft interaction and $\mathcal{L}_{conf}$. In order to make contact with the results of lattice simulations we use the model with the number of flavors $N_f = 1$. Therefore, the λ^i matrices in Eq. (2.3) may be replaced by unity. We then use

$$\begin{aligned} \mathcal{L} &= \bar{q}(i\partial\!\!\!/ - m^0)q + \frac{G_S}{2}[(\bar{q}q)^2 + (\bar{q}i\gamma_5 q)^2] \\ &- \frac{G_V}{2}[(\bar{q}\gamma_\mu q)^2 + (\bar{q}\gamma_5\gamma_\mu q)^2] \end{aligned} \tag{4.44}$$

in order to calculate the hadronic current correlation functions. Thus, there are essentially three parameters to consider, G_S, G_V and a Gaussian cutoff parameter α, which restricts the momentum integrals through a factor $\exp[-\vec{k}^2/\alpha^2]$. As suggested by the Stony Brook group, we consider the NJL model and the associated chiral Lagrangian of Eq. (4.44) as providing a simplified representation of the instanton dynamics important for the problems considered in this work. Since the results obtained for the hadronic current correlation functions are similar in the scalar, pseudoscalar, vector and axial-vector channels, we carry out our calculations for the scalar $q\bar{q}$ states and multiple our results for the optical potential by 4. The parameters G and α were fixed in our earlier studies (21). We take G =1.0 GeV^{-2} and $\alpha = 4.4$ GeV. These values provide good fits (21) to the hadronic current correlation functions found in the lattice studies (54). In order to calculate the optical potential for a quark we consider the quark moving in an antiquark distribution characterized by a temperature-dependent occupation factor $n(\vec{p}_1)$ which depends upon the chemical potential μ. The energy of a quark is given by $E(\vec{p}) = [\vec{p}^{\,2} + m^2]^{1/2}$. We follow the work of Shuryak (51), for example, and put $m = 1$ GeV. In Shuryak's work this mass is not the current quark mass, but is called the "chiral mass". (We would prefer to call the 1 GeV mass, the "thermal mass", however, the terminology used is not important for this work.) The quark thermal mass is given in Ref. (12), with $C_F = 4/3$, as

$$m^2 = \frac{1}{8} g^2 C_F (T^2 + \frac{\mu^2}{\pi^2}), \tag{4.45}$$

for the case of a finite chemical potential. The thermal gluon mass is

$$m_g^2 = \frac{1}{6} g^2 T^2 (C_A + \frac{1}{2} N_f). \tag{4.46}$$

(The relation between thermal masses in QED and QCD is given on p.146 of Ref. (12).) In studies of baryon matter, the chemical potentials used are often about 300 MeV or less. However, once we introduce a thermal mass of about 1 GeV, we need to determine the chemical potential for the quarks. In this work we will consider a chemical potential of about 1 GeV, although the calculations are easily made for other values. Once we put $m = 1$ GeV, the chemical potential is the only parameter which is varied in our study.

4.2.2 Calculation of the Quark Optical Potential

It is useful to contrast the calculation of the quark optical potential with the calculation of the nucleon optical potential that is to be used in the Dirac equation. The latter calculation is discussed in detail in Ref. (48). In that calculation of the nucleon-nucleus potential one calculates the T-matrix for nucleon-nucleon scattering using the one-boson-exchange (OBE) model. In that case the mesons of the OBE model undergo t-channel and u-channel exchange between the nucleons. The result is that the imaginary part of the optical potential has a magnitude of about 10 MeV (48). That in turn leads to a mean-free-path of about 10 fm for a 500 MeV nucleon. Many years ago, the relatively large value for the nucleon mean-free-path lead to the characterization of the optical model for nucleon-nucleus scattering as the “cloudy crystal ball” model. When we study quark propagation in the quark-gluon plasma we may consider a similar calculation of the optical potential at finite temperature. In the case of the quark-antiquark interaction the T matrix is dominated by s-channel resonances of the type found in the MEM studies. As we will see, the interaction in this case is quite strong, leading to a small mean-free-path. The resulting model is called the “sticky molasses” model (51; 52; 53) as opposed to the “cloudy crystal ball” model used to describe nucleon-nucleus scattering. We now consider the potential seen by a quark of momentum $\vec{p}_2$ and average over the quark spin s_2. (We will consider quarks of a single flavor, since that was done in the MEM studies that we have used to fix the parameters of our model.) In Ref. (48) the relativistic optical potential was denoted as $\Sigma(\vec{p}, s)$ and, for this work, we consider

$$\Sigma^{++}(\vec{p}_2) = \frac{1}{2}\sum_{s_2} \bar{u}(\vec{p}_2, s_2)\Sigma(\vec{p}_2, s_2)u(\vec{p}_2, s_2). \tag{4.47}$$

It is useful to introduce (55)

$$U(\vec{p}_2) = N\sqrt{\frac{m}{E(\vec{p}_2)}}\Sigma^{++}(\vec{p}_2)\sqrt{\frac{m}{E(\vec{p}_2)}}. \tag{4.48}$$

Here the factor of $N = 4$ takes into account the sum of the interactions in the scalar, pseudoscalar, vector and axial-vector channels which are taken to be equal for the purposes of this work. The approximate equality of the interactions in these channels may be seen in Ref. (54). (Note that values of $U(\vec{p})$ are given in Ref. (48) for the case of nucleon-nucleus scattering.)

If p_1 is the momentum of the antiquark in the medium, we may introduce the four-vector

$$P^\mu = (p_1 + p_2)^\mu. \tag{4.49}$$

Now

$$\begin{aligned} P^2 &= P_0^2 - \vec{P}^{\,2} && (4.50)\\ &= (E(\vec{p}_1) + E(\vec{p}_2))^2 - (\vec{p}_1^{\,2} + \vec{p}_2^{\,2} + 2|\vec{p}_1||\vec{p}_2|\cos\theta). && (4.51) \end{aligned}$$

Here, we take $\vec{p}_2$ along the z axis. We define

$$t(\vec{p}_1, \vec{p}_2) = \frac{1}{\pi P^2}\left[\frac{G}{1 - GJ(\vec{p}_1, \vec{p}_2)}\right], \tag{4.52}$$

where $J(\vec{p}_1, \vec{p}_2)$ is the $q\bar{q}$ vacuum polarization function defined as before. (We remark that we may also use the notation $t(P^2, p_2)$ for the quantity defined in Eq. (4.52).)

It is also useful to introduce the occupation factor $n(\vec{p}_1)$:

$$n(\vec{p}_1) = \frac{1}{e^{\beta[E(\vec{p}_1)-\mu]}+1}, \tag{4.53}$$

with $\beta = 1/T$ and $E(\vec{p}_1) = [\vec{p}_1^{\,2} + m^2]^{1/2}$. We recall

$$\sum_{s_2} u(p_2, s_2)\bar{u}(p_2, s_2) = \left(\frac{\not{p}_2 + m}{2m}\right), \tag{4.54}$$

$$\sum_{s_1} v(p_1, s_1)\bar{v}(p_1, s_1) = \left(\frac{\not{p}_1 - m}{2m}\right), \tag{4.55}$$

and note that

$$\mathrm{Tr}\left(\frac{\not{p}_2 + m}{2m}\right)\left(\frac{\not{p}_1 - m}{2m}\right) = \left[\frac{(E_1E_2 - \vec{p}_1\cdot\vec{p}_2) - m^2}{m^2}\right]. \tag{4.56}$$

Thus,

$$\begin{aligned}\mathrm{Im}\Sigma^{++}(p_2) = -\frac{1}{2}\int \frac{d\vec{p}_1}{(2\pi)^3}\frac{m}{E(\vec{p}_1)}\mathrm{Im}\left[\frac{G}{1 - GJ(\vec{p}_1, \vec{p}_2)}\right] \\ \times\left[\frac{E_1E_2 - \vec{p}_1\cdot\vec{p}_2 - m^2}{m^2}\right] n(\vec{p}_1),\end{aligned} \tag{4.57}$$

and

$$\begin{aligned}U(\vec{p}_2) = -\frac{N}{2}\frac{m}{E(\vec{p}_2)}\int \frac{d\vec{p}_1}{(2\pi)^3}\frac{m}{E(\vec{p}_1)}\pi P^2 t(\vec{p}_1, \vec{p}_2) \\ \times\left[\frac{E_1E_2 - \vec{p}_1\cdot\vec{p}_2 - m^2}{m^2}\right] n(\vec{p}_1).\end{aligned} \tag{4.58}$$

Here $E_1 = E(\vec{p}_1)$, $E_2 = E(\vec{p}_2)$ and we have made use of Eqs. (4.48) and (4.52). Values of $t(P^2, p_2)$ are shown in Fig. 4.8 for values of $|\vec{p}_2|$ ranging from 0.01 GeV to 0.31 GeV. In Fig. 4.9 we show the values of $n(\vec{p}_1)$ for the three values of μ

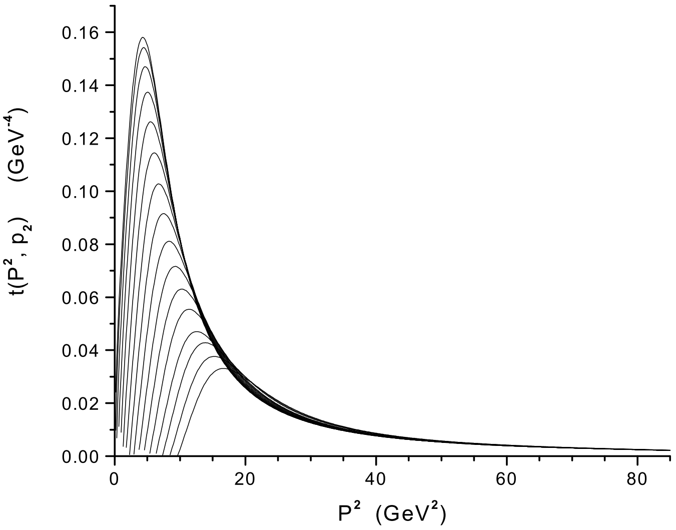

Figure 4.8: Values of $t(P^2, p_2)$ are shown for various values of the quark momentum $|\vec{p}_2|$. Starting with the uppermost curve, the $|\vec{p}_2|$ values in GeV units are 0.01, 0.03, 0.05, 0.07, 0.09, 0.11, 0.13, 0.15, 0.17, 0.19, 0.21, 0.23, 0.25, 0.27, 0.29 and 0.31. (For large P^2, we have $t(P^2, p_2) \simeq (1/\pi P^2)G$.) Here $P^2 = (p_1 + p_2)^2$, where p_1 is the antiquark momentum.

considered here and in Fig. 4.10 we present values of $\mathrm{Im}U(\vec{p}_2)$ for those values of μ. In Fig. 4.11 we show the values for the mean-free-path

$$\lambda = \frac{|\vec{p}_2|}{m} \frac{1}{|\mathrm{Im}U(\vec{p}_2)|}. \tag{4.59}$$

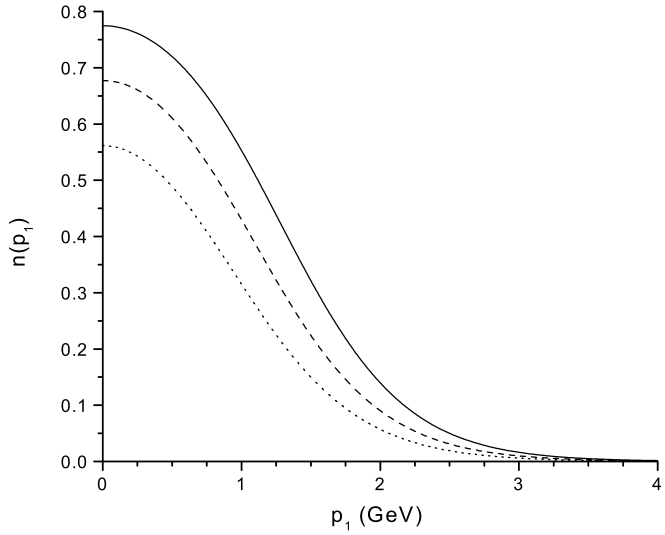

Figure 4.9: Values of $n(p_1)$ are shown for $\mu = 1.1\,\mathrm{GeV}$ (dotted curve), $\mu = 1.3\,\mathrm{GeV}$ (dashed curve) and $\mu = 1.5\,\mathrm{GeV}$ (solid curve). Here $T = 1.5\,T_c$ with $T_c = 270\,\mathrm{MeV}$.

4.2.3 Discussion

Information is available concerning the *baryon* chemical potential. That chemical potential is parameterized in Ref. (56) as

$$\mu_B = \frac{1270\,\mathrm{MeV}}{\left(1 + \dfrac{\sqrt{S_{NN}}}{4.3}\right)}, \tag{4.60}$$

and varies strongly with $\sqrt{S_{NN}}$, which is in GeV units in Eq. (4.60). For $\sqrt{S_{NN}}$ = 200 GeV, we have μ_B = 26.7 MeV.

Of particular significance for our results is the choice of the chemical potential for the quarks. We have taken $\mu \simeq 1$ GeV. In the case of the quarks, the choice

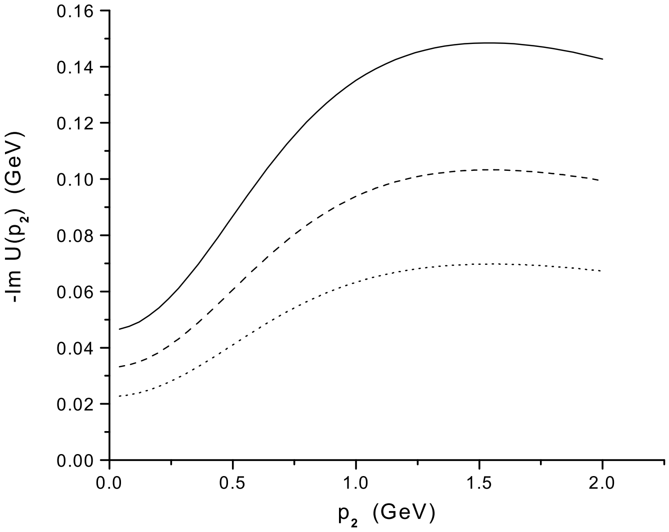

Figure 4.10: The imaginary part of the quark optical potential is shown for $\mu = 1.1\,\mathrm{GeV}$ (dotted curve), $\mu = 1.3\,\mathrm{GeV}$ (dashed curve) and $\mu = 1.5\,\mathrm{GeV}$ (solid curve). (We recall that the nucleon-nucleus imaginary optical potential is about $0.01\,\mathrm{GeV}$ in magnitude (48).)

of $\mu \simeq 1$ GeV leads to small mean-free-paths consistent with the suggestion of Shuryak that the resonances seen in the MEM analysis of the lattice results are responsible for the small mean-free-paths of the “sticky molasses” model.

We remark that in nuclear matter the baryon density is 0.17 fm^{-3} or 0.51 quarks/fm^3 if we consider the nucleon to be composed of three quarks. For the values of $n(\vec{p}_1)$ shown in Fig. 4.9 for the case $\mu = 1.3$ GeV, we may calculate the density of antiquarks to be 5.91 fm^{-3}, so that the density of quarks and antiquarks is about 12 fm^{-3} in our model. We remark that the energy density at

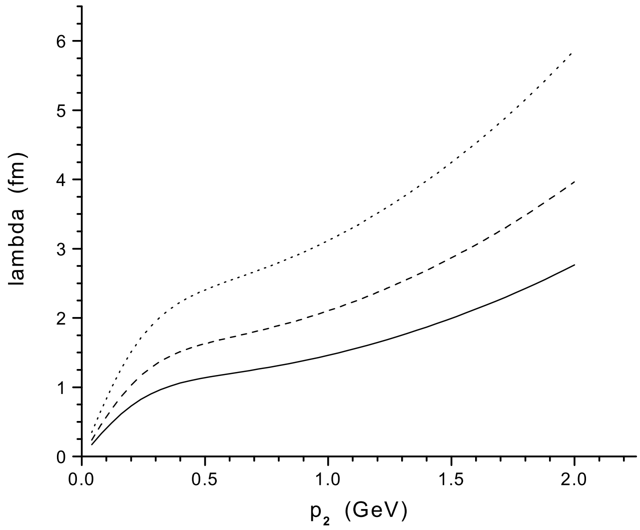

Figure 4.11: Values of $\lambda(p_2)$ are shown for $\mu = 1.1\,\mathrm{GeV}$ (dotted curve), $\mu = 1.3\,\mathrm{GeV}$ (dashed curve) and $\mu = 1.5\,\mathrm{GeV}$ (solid curve).

RHIC for $\sqrt{S_{NN}} = 200$ GeV is 4.1 GeV/fm^3 (56), which is about 26 times the energy density of nuclear matter, which is approximately 0.16 GeV/fm^3.

In this work we have attempted to provide a quantitative analysis of the suggestion (51) that the large $q\bar{q}$ resonant scattering cross sections are responsible for the small quark mean-free-paths, with the associated relevance of the hydrodynamic description of the system that is created in high-energy nucleus-nucleus collisions. We have considered the interaction in the scalar, pseudoscalar, vector and axial-vector channels of the $q\bar{q}$ system. It is possible that there are important resonances of qq character, as well as the $q\bar{q}$ resonances considered here. Such qq states are depicted in Fig. 8a of Ref. (51). It would be of interest to see if such states are found in lattice studies using the MEM scheme.

Chapter 5

Conclusions

We have explored the application of the Nambu–Jona-Lasinio model in the study of the quark-gluon plasma at high temperature and density. At quite high density one expects the formation of diquarks and possibly other interesting structures. The high-density regime is of particular interest in the study of neutron stars, a topic we do not discuss. We have been mainly concerned with the calculation of resonances in hadronic current correlation functions. In that regard, our work has been stimulated by the results of lattice gauge calculations of hadronic correlators in which resonances have been found. Of particular interest is the fact that the presence of resonances leads to quite small quark mean-free paths and ultimately to the success of a hydrodynamic description of the quark-gluon plasma in the early stages of formation of the compound system.

There have been few applications of the NJL model at high temperature. The inclusion of temperature-dependent coupling constants and masses leads to a degree of uncertainty in the formalism and lattice studies may provide some guide as to how to proceed. It is well known that perturbation theory at finite temperature is quite difficult to formulate and systematic studies have not been made using first principles. We hope that our efforts will suggest new approaches for the study of the strongly interacting quark-gluon plasma.

References

[1] I. Wetzorke, F. Karsch, E. Laermann, P. Petreczky, and S. Stickan, Nucl. Phys. B (Proc. Suppl.) **106**, 510 (2002).

[2] F. Karsch, S. Datta, E. Laermann, P. Petreczky, and S. Stickan, and I. Wetzorke, Nucl. Phys. A **715**, 701 (2003).

[3] F. Karsch, E.Laermann, P. Petreczky, S. Stickan, and I. Wetzorke, Phys. Lett. B **530**, 147 (2002).

[4] M. Asakawa, T. Hatsuda and Y. Nakahara, Nucl. Phys. A **715**, 863 (2003).

[5] T. Umeda, K. Nomura and H. Matsufuru, Eur. Phys. J. C **39**, S1.9 (2005).

[6] I. Wetzorke, hep-lat/0305012. (Invited talk at the 'Seventh Workshop on Quantum Chromodynamics', Villefranche-sur-mer, France, Jan. 6-10, 2003).

[7] C. M. Shakin and Huangsheng Wang, Phys. Rev. D **65**, 094003 (2002).

[8] T. Hatsuda and T. Kunihiro, Phys. Rep. **247**, 221 (1994).

[9] U. Vogl and W. Weise, Prog. Part. Nucl. Phys. **27**, 195 (1991).

[10] Hu Li and C. M. Shakin, hep-ph/0209136.

[11] S. P. Klevansky, Rev. Mod. Phys. **64**, 649 (1992).

[12] M. Le Bellac, *Thermal Field Theory* (Cambridge Univ. Press, Cambridge, 1996).

[13] Bing He, Hu Li, C. M. Shakin, and Qing Sun, nucl-th/0203010.

[14] R. L. Kobes and G. W. Semenoff, Nucl. Phys. B **260**, 714 (1985).

[15] C. M. Shakin, Wei-Dong Sun, and J. Szweda, Ann of Phys. (NY) **241**, 37 (1995).

[16] F. Karsch, M. G. Mustafa, M. H. Thoma, Phys. Lett. B **497**, 249 (2001).

[17] Hu Li and C. M. Shakin, hep-ph/0209258.

[18] L. S. Celenza, Bo Huang, Huangshen Wang, and C. M. Shakin, Phys. Rev. C **60**, 025202 (1999).

[19] P. Petreczky, J. Phys. G **30**, S431-S440 (2004).

[20] S. Datta, F. Karsch, P. Petreczky and I. Wetzorke, Phys. Rev. D **69**, 094507 (2004).

[21] Xiangdong Li, Hu Li, C.M. Shakin, and Qing Sun, Phys. Rev. C **70**, 048201 (2004).

[22] W. Florkowski, Acta Phys. Polon. B **28**, 2079 (1997).

[23] S. Schmidt, D. Blaschke and Y. L. Kalinovsky, Phys. Rev. C **50**, 435 (1994).

[24] F. Karsch, Lect. Notes Phys. **583**, 209 (2002), hep-lat/0106019.

[25] Hu Li and C. M. Shakin, Phys. Rev. D **66**, 074016 (2002).

[26] For reviews, see K. Rajagopal and F. Wilczek, in *At the Frontier of Particle Physics/Handbook of QCD*, M. Shifman ed. (World Scientific, Singapore 2001); M. Alford, Annu. Rev. Nucl. Part. Sci. **51**, 131 (2001).

[27] M. Alford, K. Rajagopal and F. Wilczek, Phys. Lett. B **422**, 247 (1998).

[28] R. Rapp, T. Schäfer, E. V. Shuryak and M. Velkovsky, Phys. Rev. Lett. **81**, 53 (1998).

[29] M. Alford, J. Berges and K. Rajagopal, Nucl. Phys. B **558**, 219 (1999).

[30] J. Kundu and K. Rajagopal, Phys. Rev. D **65**, 094022 (2002).

[31] S. Datta, F. Karsch, P. Petreczky and I. Wetzorke, hep-lat/0208012.

[32] S. Digal, P. Petreczky, and H. Satz, Phys. Rev. D **64**, 094015 (2001).

[33] C. R. Allton, S. Ejiri, S. J. Hands, O. Kaczmarek, F. Karsch, E. Laermann, Ch. Schmidt, and L. Scorzato, Phys. Rev. D **66**, 074507 (2002).

[34] S. Ejiri, C. R. Allton, S. J. Hands, O. Kaczmarek, F. Karsch, E. Laermann, and L. Scorzato, Nucl. Phys. B (Proc. Suppl.) **106**, 459 (2002).

[35] F. Karsch, Lect. Notes Phys. **583**, 209 (2002).

[36] F. Karsch, Nucl. Phys. B (Proc. Suppl.) **83**, 14 (2000).

[37] J. Engels, O. Kaczmarek, F. Karsch and E. Laermann, Nucl. Phys. B **558**, 307 (1999).

[38] Z. Fodor and S. D. Katz, hep-lat/0204029; Nucl. Phys. B (Proc. Suppl.) **106**, 441 (2002) [hep-lat/0110102]; Phys. Lett. B **534**, 87 (2002).

[39] Bing He, Hu Li, C. M. Shakin, and Qing Sun, Phys. Rev. D **67**, 014022 (2003).

[40] L. S. Celenza, Hu Li, C. M. Shakin, and Qing Sun, Phys. Rev. D **66**, 054010 (2002).

[41] Ph. de Forcrand, M. Garcia Pérez, T. Hashimoto, S. Hioki, H. Matsufuru, O. Miyamura, A. Nakamura, I. O. Stamatescu, T. Takaishi and T. Umeda, Phys. Rev. D **63**, 054501 (2001).

[42] J. Skullerud, D. B. Leinweber, and A. G. Williams, Phys. Rev. D **64**, 074508 (2001).

[43] C. M. Shakin and Huangsheng Wang, Phys. Rev. D **65**, 094003 (2002).

[44] C. M. Shakin and Huangsheng Wang, Phys. Rev. D **64**, 094020 (2001).

[45] L. S. Celenza, Shun-fu Gao, Bo Huang, Huangsheng Wang, and C. M. Shakin, Phys. Rev. C **61**, 035201 (2000).

[46] E. G. Drukarev and E. M. Levin, Prog. Part. Nucl. Phys. **27**, 77 (1991).

[47] B. D. Serot and J. D. Walecka, in *Advances in Nuclear Physics*, Vol. 16, edited by J. W. Negele and E. Vogt (Plenum, New York, 1986).

[48] L. S. Celenza and C. M. Shakin, *Relativistic Nuclear Physics: Theories of Structure and Scattering* (World Scientific, Singapore, 1986).

[49] J. Szweda, L. S. Celenza, C. M. Shakin and W.-D. Sun, Few-Body Systems **20**, 93 (1996).

[50] M. Lutz, S. Klimt, and W. Weise, Nucl. Phys. A **542**, 521 (1992).

[51] E. Shuryak, Prog. Part. Nucl. Phys. **53**, 273 (2004).

[52] G. E. Brown, C. H. Lee, M. Rho, and E. Shuryak, Nucl. Phys. A **740**, 171 (2004).

[53] G. E. Brown, C. H. Lee, M. Rho, and E. Shuryak, J. Phys. G **30**, S1275 (2004); G. E. Brown, C. H. Lee, and M. Rho, hep-ph/0402207.

[54] P. Petreczky, J. Phys. G **30**, S431 (2004).

[55] Bing He, Hu Li, C. M. Shakin, and Qing Sun, Phys. Rev. D **67**, 114012 (2003).

[56] A. Andronic and P. Braun-Munzinger, hep-ph/0402291.